Investigation of a Pulsed Plasma Thruster for Atmospheric Applications

Manuel Azuara Rosales

A dissertation

submitted in partial fulfillment of the

requirements for the degree of

Doctor of Philosophy

University of Washington

2020

Reading Committee:

Robert M. Winglee, Chair

Brian Nelson

Justin Little

Program Authorized to Offer Degree:

Aeronautics and Astronautics

University of Washington

Abstract

Investigation of a Pulsed Plasma Thruster for Atmospheric Applications

Manuel Azuara Rosales

Chair of the Supervisory Committee:
Professor Robert M. Winglee
Department of Earth and Space Sciences

To date, the controlled access to terrestrial atmospheric altitudes of more than 20 km is limited with current technology. This is because at such altitudes, the background gas density is too low for conventional blade-based propellers to operate, and too high for most in-space electric propulsion systems. This research aims to investigate the Pulsed Plasma Thruster technology for atmospheric applications, at a background gas pressure of less than 50 Torr, corresponding to terrestrial atmospheric altitudes of more than 20 km. Because the system operates in a highly collisional regime, three acceleration mechanisms are identified, 1) due to ion-neutral collisions, 2) due to the $\mathbf{J} \times \mathbf{B}$ force, and 3) electrostatic acceleration. A theoretical model to obtain the thrust-to-power ratio of a Pulsed Plasma Thruster for atmospheric applications is presented and validated experimentally using a pendulum-based thrust stand, a quadruple Langmuir probe, and

a B-dot probe. A proposed Air-Breathing Pulsed Plasma Thruster was investigated, and based on the experimental results, an analytical approach to determine whether the system can sustain an aircraft at the aforementioned altitudes is presented, and experimentally demonstrated through three in-field tests, consisting on launching in-house designed and built aircraft to the stratosphere using high-altitude burst balloons.

TABLE OF CONTENTS

List of Figures iii

List of Tables xi

Chapter 1. Introduction 1

- 1.1 Different Attempts to Reach High Atmospheric Altitudes 3
- 1.2 Electric Propulsion Overview 7
- 1.3 Electric Propulsion for Atmospheric Applications 11
- 1.4 The Pulsed Plasma Thruster 16

Chapter 2. Pulsed Plasma Thruster for Atmospheric Applications 22

- 2.1 Principle of Operation 22
- 2.2 Cathode Length Estimation 28

Chapter 3. Air-Breathing Pulsed Plasma Thruster (AB-PPT) 31

- 3.1 Experiment Setup 31
- 3.2 Early Designs 39
  - 3.2.1 AB-PPT with a Daisy-Shaped Cathode 39
  - 3.2.2 Addition of the Variable Spacing Cathode Mechanism 46
- 3.3 Second Iteration of the AB-PPT, with the Addition of the Variable Spacing Cathode Mechanism 53

Chapter 4. AB-PPT Plasma Characteristics 64

- 4.1 Experiment Setup 64

4.2 Langmuir Probe 66

4.3 B-Dot Probe 73

4.4 Results 78

4.5 AB-PPT versus Conventional Propellers 79

Chapter 5. Proposed Aircraft 84

5.1 Aircraft Design Considerations 84

5.2 Proof of Concept 92

5.2.1 Experimental Lift with Electric Propulsion at High Altitude Niche, Test 1 94

5.2.2 Experimental Lift with Electric Propulsion at High Altitude Niche, Test 2 97

5.2.3 Experimental Lift with Electric Propulsion at High Altitude Niche, Test 3 105

Chapter 6. Further Applications 110

6.1 Possible Applications for Mars Exploration 110

Chapter 7. Conclusions 114

Bibliography 116

Appendix A: E3 and E2 Microcontroller (PIC16F628A) ASM Code 120

Appendix B: AB-PPT as a Hybrid System 122

LIST OF FIGURES

Figure 1.1: Intended atmospheric range of operation, 20-35 km. Typical atmospheric altitude at which commercial airplanes fly at is 10 km..2

Figure 1.2: a) HELIOS drone developed by NASA in 1999 [1]. Helios reached a maximum altitude of 29 km and remained there for approximately 40 minutes, b) Zephyr drone developed by Airbus [2]. Its development started in 2003. Zephyr has the record for flight duration of an unmanned aerial vehicle (UAV) at an atmospheric altitude of 20 km, c) Aquila drone developed by Facebook in 2016 [3]. Aquila has had two successful flights, and the project is currently stopped...4

Figure 1.3: Google Loon project. 6

Figure 1.4: Ratio of propellant mass to spacecraft's initial mass as a function of exhaust velocity for different Δv. The green line represents the average maximum exhaust velocity achievable by chemical propulsion. 9

Figure 1.5: Early concepts of the Air-Breathing Pulsed Plasma Thruster developed at the Advanced Propulsion Laboratory (APL) in 2014 [12]. From left to right the diameter of the devices are 7.6, 5, 2.5-5, and 2.5 cm. All of the four concepts were 8 cm in length...16

Figure 1.6: In-space breech fed rectangular Pulsed Plasma Thruster configuration. 17

Figure 1.7: In-space, breech-fed, coaxial Pulsed Plasma Thruster configuration. 18

Figure 1.8: Equivalent inductance-capacitance-resistance (LCR) electric circuit of a rectangular pulsed plasma thruster...20

Figure 2.1: Simplified version of a coaxial air-breathing pulsed plasma thruster. The cone-shaped body guides the air to flow into the discharge section. Details such as electrical connections and the nozzle have been omitted.......................................23

Figure 2.2: Cross section of a coaxial air-breathing pulsed plasma thruster. The cone-shaped body guides the air to flow into the discharge section, i.e. at station 1. The main voltage discharge between the anode and the cathode ionizes the background gases. Station 1 represents the location where breakdown of air occurs, whereas station 2 represents the location where the plasma is fully dissipated.................................24

Figure 3.1: Bell-jar shaped vacuum chamber with a volumetric capacity of 0.14 m^3 used to test the multiple iterations of the AB-PPT at the APL. 32

Figure 3.2: Simplified circuit diagram for the AB-PPT experiment. 32

Figure 3.3: CAD model of the pendulum-based thrust stand, used to measure the specific thrust of the different iterations of the AB-PPT. 34

Figure 3.4: Side view and front view of the pendulum-based thrust stand with dimensions. ...34

Figure 3.5: Typical pendulum raw data after the main discharge of the AB-PPT occurred. The maximum (first) peak of the sinusoidal voltage signal was used as the deflected pendulum angle. 36

Figure 3.6: Sample comparison picture of the AB-PPT and pendulum; before, during and after the main discharge...36

Figure 3.7: Correlation between the maximum (first) peak of the pick-up sinusoidal voltage signal and the corresponding pendulum deflected angle. 37

Figure 3.8: Front view picture of the Air-Breathing Pulsed Plasma Thruster with a daisy-shaped cathode. First iteration is shown on the left, and second iteration is shown on the right. 40

Figure 3.9: First iteration of the AB-PPT using a daisy-shaped cathode configuration. Cathode's length of 15 mm. Specific thrust measurements of less than 100 mN/kW were obtained using the pendulum based thrust stand. (*Electric connections not shown in this figure*) 41

Figure 3.10: Second iteration of the AB-PPT using a daisy-shaped cathode configuration. Except for the length of the cathode, the dimensions of the device are similar to the previous daisy-shaped cathode PPT. Specific thrust measurements of 470 mN/kW were

obtained using the pendulum based thrust stand. (*Electric connections not shown in this figure* 44

Figure 3.11: Igniter location in both of the daisy-shaped cathode AB-PPT configurations. Details such as the nozzle and electrical connections have been omitted in this figure. 45

Figure 3.12: First iteration of the AB-PPT with the addition of the variable spacing cathode mechanism..47

Figure 3.13: First iteration of the AB-PPT with the variable spacing cathode mechanism at three different positions. From left to right, 28, 55, and 73.2 mm diameter...................48

Figure 3.14: Igniter configuration in the first iteration of the AB-PPT with the addition of the variable spacing cathode mechanism. Details such as the nozzle, variable spacing cathode mechanism, and electrical connections have been omitted in this figure..49

Figure 3.15: Cathode diameter of the first iteration of the AB-PPT with the addition of the variable spacing cathode mechanism versus the highest background air pressure at which breakdown first occurs. The experiment was performed using three different voltage sources, 1000, 1200, and 1500 Volts, at five different cathode diameters, 28, 37, 51.5, 62, and 73 mm for the 1000 and 1200 Volts, and six different cathode diameters for the 1500 Volts case. 50

Figure 3.16: Specific thrust versus background pressure of the first iteration of the AB-PPT with the addition of the variable spacing cathode mechanism. The experiment was performed using three different voltage sources, 1000, 1200, and 1500 Volts, at five different cathode diameters, 28, 37, 51.5, 62, and 73 mm. Maximum specific thrust values of 240 mN/kW were achieved, with 1200 Volts at a background pressure of 19 Torr, and with 1500 Volts at a background pressure of 28 Torr........................51

Figure 3.17: Second iteration of the AB-PPT with the addition of the variable spacing cathode mechanism..54

Figure 3.18: Cathode configurations of the first and second iteration of the AB-PPT with the addition of the variable spacing cathode mechanism..55

Figure 3.19: Top view of the second iteration of the AB-PPT with the addition of the variable spacing cathode mechanism, at three different cathode diameters, 26.8, 40.8, and 52.4 mm. The nozzle is not shown in this figure. 56

Figure 3.20: Cross section view of the second iteration of the AB-PPT with the addition of the variable spacing cathode mechanism. Details such as the channel for the main gear bearings, and the chamfer addition to the air intake are shown. Electrical connections are not shown in this diagram. 57

Figure 3.21: Igniter configuration for the second iteration of the AB-PPT with the addition of the variable spacing cathode mechanism. 58

Figure 3.22: Igniter mechanism for the second iteration of the AB-PPT with the addition of the variable spacing cathode mechanism. 59

Figure 3.23: Cathode diameter of the AB-PPT versus the highest background pressure at which breakdown of air first occurs. The experiment was performed using a voltage source of 800 Volts, and five different cathode diameters, 26.8, 34, 40.8, 45.5, and 52.4 mm. For comparison, the three non-continuous lines show the cathode diameter versus the background pressure using 1000, 1200, and 1500 Volts, of the first iteration of the AB-PPT with the addition of the variable spacing cathode mechanism....................60

Figure 3.24: Specific thrust versus background gas pressure of the second iteration of the AB-PPT with the addition of the variable spacing cathode mechanism (continuous line). The test was performed using a voltage source of 800 Volts, and five different cathode diameters, 26.8, 34, 40.8, 45.5, and 52.4 mm. A maximum specific thrust value of 395 mN/kW was achieved, and at the intended range of operation, specific thrust values of > 350 mN/kW can be sustained. For comparison, the three non-continuous lines show the specific thrust values obtained using the first iteration of the AB-PPT with the addition of the variable spacing cathode mechanism, using 1000, 1200, and 1500 Volts. 62

Figure 4.1: Typical experimental setup of the AB-PPT for the measurements of the different plasma parameters. 65

Figure 4.2: Voltage and current traces of the AB-PPT main discharge, using 800 Volts per discharge, with a capacitor bank of 40 μF. 66

Figure 4.3: Side view and front view drawings of the quadruple Langmuir probe used to measure the ion density, plasma temperature, and ion speed of the AB-PPT. 67

Figure 4.4: Setup of the quadruple Langmuir probe on the AB-PPT. In order to place the probe, the nozzle was substituted for the Langmuir probe support. 68

Figure 4.5: Quadruple Langmuir probe electric diagram. Probes 1, 2, and 3 are parallel to the plasma flow, and probe 4 perpendicular to it. Vs represents the voltage source, Vm the voltage to measure, and Rs are the shunt resistors used to measure the collected current by probes 3 and 4, i.e. $I3$ and $I4$. 69

Figure 4.6: Electron density, electron temperature, and Mach number measurements of the AB-PPT at $z = 30\ mm$ along the axis. 72

Figure 4.7: B-dot probe set up used to measure to magnetic field of the AB-PPT in the theta direction. The dimensions of the chip are $2.62 \times 2.45 \times 1.83$ mm, and it was mounted on a 3D printed support to fit around the anode 4.7 mm in diameter anode. 73

Figure 4.8: B-dot probe schematic diagram. 74

Figure 4.9: Typical raw voltage signal from the Helmholtz coil, and the B-dot probe (unfiltered and filtered). 75

Figure 4.10: Top view of the AB-PPT showing the B-dot probe array. The probe was positioned at $z = 0$, at four different angular positions, 0, 90, 180, and 270 degrees. The zero degrees position represents the point where breakdown is initiated. Details such as the nozzle, the variable spacing mechanism and servo motors have been omitted in this figure. 76

Figure 4.11: Magnetic field measurements, at $z = 0$, and different angular positions; 0, 90, 180, and 270 degrees. 77

Figure 4.12: On the left, in-house designed propeller for high-altitudes, mounted on the commercial digital scale with an accuracy of ±0.01 grams. On the right, commercial 10-cm propeller, mounted on the RC lander outer rotor motor thrust stand...........80

Figure 4.13: Specific thrust as a function of altitude of a conventional blade-based propeller. .81

Figure 4.14: Specific thrust values as a function of altitude of the conventional blade-based propeller and the AB-PPT. The dotted black like represents the maximum values of specific thrust experimentally obtained at the APL. 81

Figure 4.15: 3D printed blade-based propellers shattered while testing at a background air pressure of 35 Torr, corresponding to an atmospheric altitude of 20 km. 83

Figure 5.1: Lift-to-drag coefficient as a function of angle of attack of an airfoil E178 for different Reynolds numbers. The lower (blue) trace represents the coefficient at the lowest Reynolds number, with the maximum lift-to-drag coefficient resulting at an angle of attack of approximately 7.5 degrees. (Figure extracted from "Airfoil Tools", UIUC Airfoil Coordinates Database [32]).). 86

Figure 5.2: Power requirements as a function of total aircraft mass. Interpolation obtained using equation (5.1), based on specific thrust values of 500 mN/kW, and a lift-to-drag coefficient of 40. 87

Figure 5.3: Possible configuration for a 20-kg aircraft, based on commercially available technology, and using specific thrust values of 500 mN/kW.................................89

Figure 5.4: Lift force, drag force, and AB-PPT thrust as a function of aircraft speed. The data shown in this figure is based on the parameters shown in Figure 5.3. The maximum possible aircraft speed is determined by the drag force, emphasized with the dotted magenta line. At this point, approximately 11 m/s, the maximum lift force would be 200 N, i.e. approximately 20 kg..90

Figure 5.5: Proposed aircraft powered with the AB-PPT. The aircraft has a wingspan of 35 meters, and the AB-PPTs are placed underneath the wings..................................92

Figure 5.6: Three of the different in field launches using high altitude burst balloons. a) ELEPHANT 1, b) ELEPHANT 2A, and c) ELEPHANT 3B. 93

Figure 5.7: ELEPHANT 1 being launched using a high altitude burst balloon. 94

Figure 5.8: Power supply consisting of 400 cell-coin batteries of 3.2 Volts and 90 mA-hr each, connected in series, resulting in a total energy of 115 W-hr.................................95

Figure 5.9: Altitude versus ground speed of the ELEPHANT 1. Data obtained from the APRS system. The jet stream was located approximately in the 8-16 km range, and for station keeping, an aircraft speed of < 10 m/s would be needed. 96

Figure 5.10: ELEPHANT 2A on the ground while being prepared, before launching. 98

Figure 5.11: ELEPHANT 2A being launched using a high altitude burst balloon. 98

Figure 5.12: Electric diagram of the charge/discharge system used for the E2A and E2B, laboratory, and in field tests. The system consists of four subsystems: pressure sensor (blue box), igniter (yellow box), main discharge (red box), computer (green box). 100

Figure 5.13: Cylindrical igniter configurations used in the first iteration of the AB-PPT with the addition of the variable spacing cathode mechanism. a) Configuration used for the in-field testing of the E2A, and E2B, b) improved cylindrical igniter configuration. Details such as the nozzle, variable spacing cathode mechanism, and electrical connections have been omitted in this figure..103

Figure 5.14: ELEPHANT 2A at its maximum altitude, approximately 25 km. Picture taken from the camera mounted on the tail of the aircraft..104

Figure 5.15: High-altitude burst balloon trajectories of the ELEPHANT 2A, and ELEPHANT 2B launches. The data is based on the APRS system. Peak altitudes are estimated as 25 km for E2A, and 24.5 for E2B. 104

Figure 5.16: ELEPHANT 2B after landing. The aircraft was found on a corn field, with no major damage to the structure. 105

Figure 5.17: Electronic systems being tested prior the different in field testing. a) electronics tested for ELEPHANT 2, b) electronics tested for ELEPHANT 3......................107

Figure 5.18: High altitude burst balloon trajectories of the ELEPHANT 3A, and ELEPHANT 3B launches. The data is based on the APRS system. Peak altitudes are estimated as 29 km for E3A, and 33 for E3B. 108

Figure 5.19: Discharge percentage as a function of atmospheric altitude of ELEPHANT 3A. 108

Figure 5.20: ELEPHANT 3B launch. In order to extend the flying time, the aircraft was launched using two balloons, filled with lower amount of gas. 109

Figure 6.1: Cathode diameters of the AB-PPT versus background gas pressure at which breakdown first occurs, for both gases, air and CO_2. The experiment was performed using 800 Volts per discharge, at five different cathode diameters: 26.8, 34, 40.8, 45.5, and 52.4 mm. 111

Figure 6.2: Specific thrust versus background gas pressure of the AB-PPT, for CO_2 and air. The test was performed using a voltage source of 800 Volts, and five different cathode diameters, 26.8, 34, 40.8, 45.5, and 52.4 mm. 112

Figure 6.3: Sequence of a proposed mission to Mars to deliver an atmospheric satellite, powered with the AB-PPT. 113

LIST OF TABLES

Table 1.1: Typical operating parameters of the most common propulsion systems, chemical and electric. Data extracted from references [7] and [8]..11

Table 1.2: Common electric propulsion devices and their considerations for applications at a background gas pressure of 50-10 Torr. 14

ACKNOWLEDGEMENTS

I would like to thank Professor Robert Winglee for all his support and guidance through my studies and research at the University of Washington, Corwin Hansen, who significantly contributed to this research, the Mexican National Council for Science and Technology (CONACYT) for the financial support, and the team at the Advanced Propulsion Laboratory, in particular Paul Sturmer and Paige E. Northway. Last but not least, I want to thank the departments of Earth and Space Sciences, and Aeronautics and Astronautics for their support and resources.

DEDICATION

to my parents.

Chapter 1. INTRODUCTION

This study aims to investigate the Pulsed Plasma Thruster (PPT) technology for atmospheric applications, at a background gas pressure of 10-50 Torr, which corresponds to terrestrial atmospheric altitudes of > 20 km. Figure 1.1 shows the intended range of operation. The access to such altitudes would bring significant benefits. For instance, one of the advantages of operating in this region is that the weather variability is very low, and if an efficient propulsion system capable of functioning using in-situ propellant (the atmospheric background gas) and capable of propelling an aircraft at these altitudes is developed, then it is possible to have an "atmospheric satellite" where the aircraft can stay up indefinitely and provide continuous communications and/or remote sensing over a fixed region - the development of such an "atmospheric satellite" would bring significant cost savings and flexibility relative to low Earth orbiting spacecraft. Further applications include the utilization of the device for planetary exploration, in particular for planets whose atmosphere resembles terrestrial atmosphere at altitudes > 20 km, such as Mars, or the upper atmosphere of Venus or Titan.

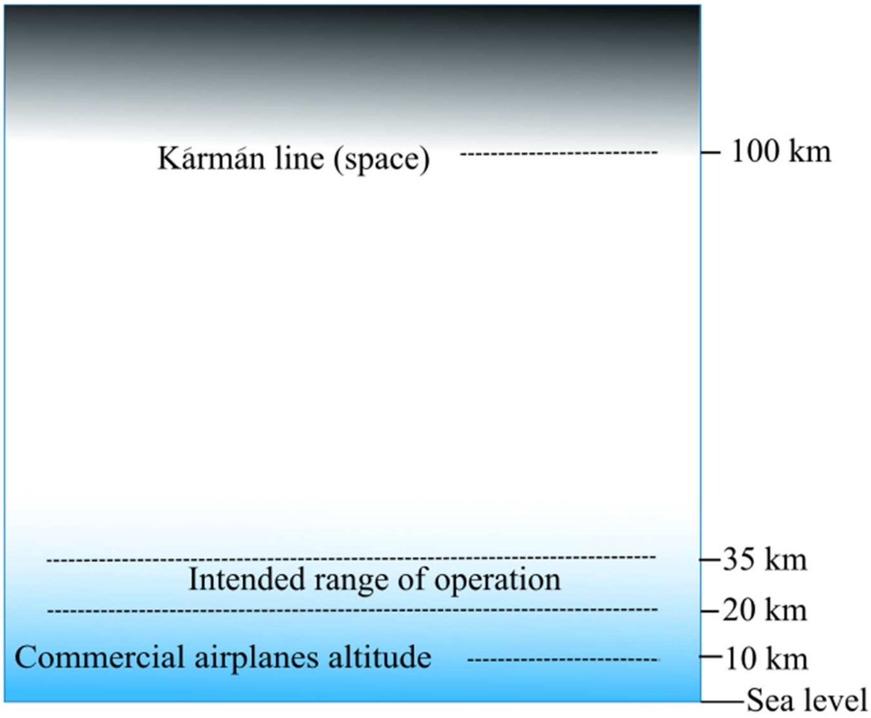

Figure 1.1: Intended atmospheric range of operation, 20-35 km. Typical atmospheric altitude at which commercial airplanes fly at is 10 km.

At such altitudes, the air density is too low for conventional propellers to operate and too high for most in-space electric propulsion systems. Additionally, the atmospheric pressure through the atmosphere varies considerably at different altitudes. This situation makes the development of a propulsion system that can efficiently operate at such altitudes more difficult. Particularly, since we intend to use the background gases of the atmosphere as fuel; and in order to reduce the complexity of the system, we intend to achieve that without the need of a compressor, or any other similar system. Therefore, in order to sustain an optimum performance through the intended range of operation, the proposed propulsion system must be able to adapt to the background gas pressure of 50-10 Torr. The development of such propulsion system, capable of efficiently operating in conditions of relative low air pressure, would enable controlled access to atmospheric altitudes that are currently limited with conventional technology, such as blade-based propellers.

This study starts with the description of some of the different efforts to reach the upper atmosphere using conventional technology, such as blade-based propellers, and non-conventional technology, such as high-altitude balloons, followed by the description of the pulsed plasma thruster technology for in-space applications, and the different implications and considerations for using the technology in thin atmosphere. A detailed description of the proposed Air-Breathing Pulsed Plasma Thruster (AB-PPT) will then be given, including a theoretical and experimental analysis of its principle of operation. Finally, a prototype of an aircraft will be proposed based on the experimental results obtained.

1.1 DIFFERENT ATTEMPTS TO REACH HIGH ATMOSPHERIC ALTITUDES

Beginning in the early 2000s, multiple efforts to operate at atmospheric altitudes of > 20 km have been performed. However, most of the concepts introduced throughout this time were designed to operate using conventional blade-based propellers. In 1999, NASA developed a propeller-driven aircraft (HELIOS, Figure 1.2a), electric-powered with solar panels, for high altitude, low atmospheric pressure operation. HELIOS reached a maximum atmospheric altitude of 29 km and remained there for approximately 40 minutes. The aircraft was destroyed due to structural failure, falling into the Pacific Ocean in 2003 [1]. A more recent attempt to reach high atmospheric altitudes using blade-based propellers is the Airbus drone “Zephyr” (Figure 1.2b), whose development started in 2003, and in summer 2018, it remained aloft for 25 days at an altitude of almost 20 km, stablishing a record for flight duration of an unmanned aerial vehicle (UAV) at such altitudes [2]. Other efforts include the Facebook drone “Aquila” (Figure 1.2c) developed in 2016 [3], and further developed in 2017 in partnership with Airbus. Aquila was designed to reach a maximum altitude of 27 km during day and dropping to 18 km at night. Since its development, the aircraft has had two successful flights, one of 96 minutes duration and the other one of one-hour and 46 minutes duration. The development status of the project is currently stopped.

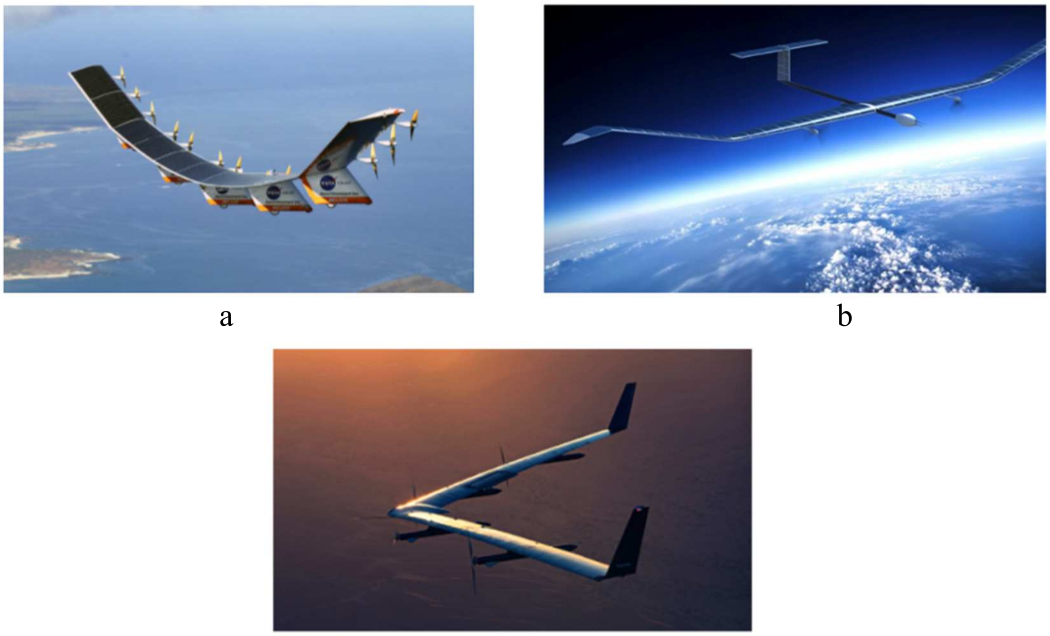

a

b

c

Figure 1.2: a) HELIOS drone developed by NASA in 1999 [1]. Helios reached a maximum altitude of 29 km and remained there for approximately 40 minutes, b) Zephyr drone developed by Airbus [2]. Its development started in 2003. Zephyr has the record for flight duration of an unmanned aerial vehicle (UAV) at an atmospheric altitude of 20 km, c) Aquila drone developed by Facebook in 2016 [3]. Aquila has had two successful flights, and the project is currently stopped.

The conventional blade-based propellers are typically used by aircraft travelling at subsonic speeds, typically below 770 km/h. The technology is more than 100 years old - it is efficient and reliable. However, propeller systems are strongly limited by the lack of air at atmospheric altitudes

> 20 km. From Bernoulli’s principle, the basic form to obtain the force of a blade-based propeller as a function of air density is expressed as,

$$F_d = \frac{1}{2}\rho A(v_e^2 - v_0^2) \tag{1.1}$$

where ρ is the density of air, A the area of the propeller, v_e the exhaust speed, and v_0 the incoming air speed. As the aircraft increases its altitude, the air density decreases and the propeller’s net force is reduced, limiting the maximum altitude that the aircraft can reach. Increasing the area of the propeller helps minimize this effect, however increasing the area represents potential structural damage to the blades, in addition to increasing the total weight of the aircraft. Another possible solution to eliminating the reduction of force by the blade-based propellers at such altitudes, is increasing the revolutions per minute (rpm), increasing the power and cooling requirements. However, the speed of the propellers cannot be increased indefinetely. The lack of air density represents a major challenge for the airfoil design of a propeller system, since the behavior of the boundary layer and the effects of laminar separation and reattachment of an airfoil at low Reynolds number, and high air speed, needs to be carefully taken into consideration in order to avoid stalling and/or structural damage to the blades. Craig L. Nickol et al. [4], provides a detailed study for design considerations of blade-based propellers for high altitude applications. Further complications result if the propellers are operated at high speeds, as at such altitudes the motors don’t have enough surrounding air to cool down during operation.

Non-conventional methods have also been explored. Such is the case of the Loon project, Figure 1.3, introduced by Google with the goal of providing Internet to unconnected areas [5].

Figure 1.3: Google Loon project.

This project is based on very large balloons filled with lighter than air gas, which can go up to 20 km of altitude. In order to move to different locations, the balloons sail the winds by moving up or down into different wind currents traveling in different directions. Other companies such as JP Aerospace have also explored this method [6]. To date, no balloon system has successfully managed to stay in a prescribed area.

Limitations of conventional and non-conventional methods encouraged the Advanced Propulsion Laboratory (APL) at the University of Washington, to search for alternative methods to efficiently operate at high altitudes in thin atmosphere. Electric propulsion (EP) is an attractive option, with features that could potentially allow us to reach controlled access to atmospheric altitudes, that to date, are difficult to achieve with the current technology. Electric propulsion is a well-known technology, that has been historically used for in-space applications, thus research in this area have been primarily focused on developing more efficient systems for applications such as station keeping, orbiting, drag compensation, deep space missions, etc. As described in this study, an electric propulsion system operating at the upper atmosphere, offers efficiencies not possible for in-space systems nor for blade-based propellers. Furthermore, the ability of the system to use the atmosphere as propellant offers the potential for indefinite flight, making the possibility of an “atmospheric satellite” a near-term reality.

1.2 ELECTRIC PROPULSION OVERVIEW

The concept of electric propulsion dates back to 1911 with the contributions of Konstantin Eduardovitch Tsiolkovsky, who is considered one of the founding fathers of rocketry and astronautics. Among his important contributions, Tsiolkovsky derived the expression that relates the change of velocity of the rocket, to the exhaust velocity and the initial and final mass of the rocket. Such expression was initially called, the formula of aviation, and today is known as the Tsiolkovsky rocket equation, or simply the rocket equation,

$$\Delta v = v_e In\left(\frac{m_0}{m_f}\right) \tag{1.2}$$

where Δv is the change of velocity of the spacecraft, m_0 and m_f are the initial, and final mass respectively, and v_e is the exhaust velocity, which can also be expressed as,

$$v_e = gI_{sp} \tag{1.3}$$

where g is the acceleration of gravity, and I_{sp} the specific impulse – a parameter that is commonly used to describe the performance of a propulsion system.

Different propulsion methods exist and can be classified based on their means by which the fuel is accelerated to create thrust. Currently, two types of propulsion methods that obey the rocket equation exist.

- Chemical propulsion, where the thrust is produced by the product of a chemical reaction. Due to the large amount of thrust, and the high fuel mass consumption, this type of propulsion method is typically used for high thrust and short time missions, such as escaping Earth.
- Electric propulsion (EP), which uses electrical energy to heat the propellant and expel it at high speeds to generate thrust. Unlike chemical propulsion, EP operates in a low thrust regime but with higher specific impulse and exhaust velocities, and hence lower mass fuel consumption. As a result, this technology is more suited for long time, and/or small thrust requirement applications, such as in-space missions.

The choice of propulsion system is based on mission requirements, such as deliverable exhaust velocity, mass consumption, and Δv. For instance, escaping Earth requires a $\Delta v = 11.2$ km/s, whereas a typical Δv for station keeping in GEO is approximately 50 m/s. Stéphane Mazouffre [7], provides a summary of different Δv requirements depending on mission types. Based on equation (1.2), in order to achieve a large Δv, two option are possible: either to use a large amount of propellant – typical regime for chemical propulsion, or having a high exhaust velocity – typical regime for electric propulsion. Figure 1.4 shows the ratio of propellant mass to the spacecraft's initial mass versus exhaust velocity for three different Δv: 1, 5, and 8 km/s.

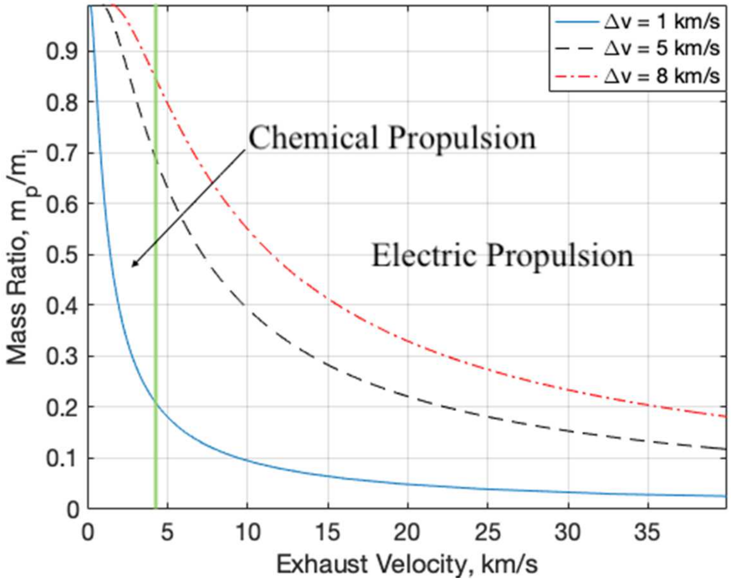

Figure 1.4: Ratio of propellant mass to spacecraft's initial mass as a function of exhaust velocity for different Δv. The green line represents the average maximum exhaust velocity achievable by chemical propulsion.

The green line represents the average maximum exhaust velocity, achievable by chemical propulsion; approximately 4.5 km/s. Because of this, the propellant mass requirements are much higher for a given Δv, when compared to EP. As a result, the applications of chemical propulsion are typically limited to short, high-thrust missions. On the other hand, EP delivers much higher values of exhaust velocity with less propellant mass, enabling its usage for in-space applications. Such high values of exhaust velocity are achieved by increasing the kinetic energy of the propellant. This is achieved by ionizing the gaseous propellant using electrical energy, before ejecting it out of the spacecraft. Thus, the thrust produced by EP devices consists of two essential steps; 1) the propellant is first ionized using electrical energy, and 2) the ionized propellant is accelerated out of the spacecraft to generate thrust. Different methods to accelerate the ionized gas exist, and typically, EP is classified by the acceleration mechanism. Currently, three categories exist,

- *Electrostatic thrusters*. In this type of thrusters, the acceleration mechanism is produced mainly by the application of a static electric field in the direction of the acceleration. The most common device in this category is the ion thruster.
- *Electromagnetic thrusters*. This type of thrusters uses the $\bar{J} \times \bar{B}$ force as the main acceleration mechanism. The most common devices are the Hall thruster and the pulsed plasma thruster (PPT). PPTs also have an electrothermal acceleration contribution; however they are usually placed in the electromagnetic thruster category.
- *Electrothermal thrusters*. In this type of thrusters, electromagnetic fields are used to increase the temperature of the bulk propellant. The thermal energy imparted to the propellant gas is then converted into kinetic energy by a nozzle. Arcjets and resistojets are the most common devices in this category.

A brief summary of the characteristic parameters of the most common propulsion systems is provided in table 1.1.

Table 1.1: Typical operating parameters of the most common propulsion systems, chemical and electric. Data extracted from references [7] and [8]

Thruster	Specific Impulse [s]	Input Power [kW]	Efficiency [%]	Propellant (typical)
Cold gas	50-75	0.05	-	Ammonia, N_2
Chemical (Liquid)	150-450	10^2 - 10^7	-	Hydrazine, LO_2+LH_2, kerosene
Chemical (Solid)	250-300	10^8	-	HTPB, NH_4CLO_4
Resistojet	300	0.5-1	65-90	N_2H_4 monoprop
Arcjet	500-600	0.9-2.2	25-45	N_2H_4 monoprop
Ion thruster	2500-3600	0.4-4.3	40-80	Xenon
Hall thruster	1500-2000	1.5-4.5	35-60	Xenon
PPTs	850-1200	< 0.2	7-13	Teflon

1.3 ELECTRIC PROPULSION FOR ATMOSPHERIC APPLICATIONS

In 1961 it was recognized that the gases of the upper atmosphere could be used as the fuel source for EP systems to propel satellite vehicles [9], but it wasn't until the early 2000's when different EP concepts for atmospheric applications were proposed and developed. Such is the case of the Air-Breathing Ion Engine (ABIE) proposed in 2003 [10], and the Air-Breathing Electrically Powered Hall Effect Thruster, first proposed by the U.S. company BUSEK in 2004 [11]. Both of these devices were designed to operate, and to power a satellite at atmospheric altitudes > 150 km. However, the net thrust produced was not enough to overcome the drag force to sustain an aircraft at such altitudes. Maximum specific thrust values of 10 mN/kW, and 30 mN/kW respectively were reported.

Due to complications of operating an EP system at atmospheric altitudes of > 150 km, and the underperformance of previous concepts at the advanced propulsion laboratory (APL) at the University of Washington, we decided to investigate EP for operation at much lower atmospheric altitudes ≥ 25 km. When compared to operating at atmospheric altitudes > 150 km, operating at much lower altitudes (≥ 25 km) has the following advantages:

1. Higher values of thrust-to-power ratio (specific thrust) are achievable [12].
2. Due to the high Knudsen number $\left(\frac{\lambda}{L}\right)$, where λ is the mean free path and L the length scale of the device, at atmospheric altitudes of 150 km, air collectors designed to compress the background air prior to entering the ignition section (section where the breakdown of gas occurs) are required [13]. At 25 km, this requirement is eliminated due to the higher background air pressure.
3. Testing the device at an atmospheric altitude of 25 km is relatively easy using conventional, and inexpensive methods, such as high-altitude burst balloons.

Excluding the conventional blade-based propeller systems, the present study is the first to consider a propulsion system that can efficiently operate in a controlled manner at atmospheric altitudes > 20 km. Thus, the question as to what EP system is best suited for the intended range of operation still remains. In order to study the appropriate EP technology for applications at such altitudes, two key conditions need to be taken into consideration.

1. At the intended range of operation, the background air density is relatively high, so the plasma is in a collisional regime, as opposed to in-space applications, where the plasma is assumed to be in a collisionless regime. As a result, the exhaust velocity is much lower than in-space analogue systems, but the specific thrust is much higher.
2. Due to the high exhaust velocities of EP devices (typically in the 5-30 km/s range), and because the system uses the background gases of the atmosphere as propellant, steady-flow devices such as ion thrusters and Hall thrusters would require the addition of an acceleration system for the incoming air. However, accelerating the air using conventional methods represents a major challenge. As will be discussed later in this section, an unsteady-flow device such as the pulsed plasma thruster, allows the breakdown of the high density of neutrals encountered at high atmospheric altitudes, and the pulse rate of the system allows for natural filling of the ionization chamber, without the need for a compressor.

Table 1.2 shows a summary of the most common EP devices, and their main considerations for their possible usage at a background gas pressure of 50-10 Torr.

Table 1.2: Common electric propulsion devices and their considerations for applications at a background gas pressure of 50-10 Torr.

Thruster	Condition for atmospheric applications
Ion Thruster	Requires collisionless plasma, and continuous flow operation.
Hall Thruster	
Resistojet and Arcjet	Can operate in a pulsed regime, but the pulse duration is long when compared to Pulsed Plasma Thrusters, thus and incoming air accelerator is needed.
Pulsed Plasma Thruster	No gas compression, and no continuous flow operation required.

Because the ion thruster and Hall thruster require collisionless plasma, and more importantly, because both of these devices operate in a steady-flow regime, the ion thruster and Hall thruster were discarded in our study. The electrothermal devices, the resistojet and arcjet, can operate in a pulse regime, however the pulse duration is long when compared to Pulsed Plasma Thrusters, thus and incoming air accelerator is needed. Additionally, these devices do not take advantage of the high collisionality caused by the high background gas pressure, and relies on accelerating the plasma and hot gases through a converging-diverging nozzle. As it will be discussed in detail in section 2.1, due to the high neutral density at the intended range of operation, the specific thrust of the proposed system does not rely on the exhaust velocity, but on collisions between charged particles and neutrals, such that the exhaust velocity is reduced, but the amount of material ejected is increased. In fact, the addition of a converging-diverging nozzle reduces the number of collisions between charged particles and neutrals, and instead, the collisions occur with the chamber and nozzle walls, such that a large amount of thrust is lost. This situation was observed when adding and testing several converging-diverging nozzle configurations to the proposed system, resulting in a reduction of the specific thrust. Finally, frozen flow losses can be an issue when accelerating the hot gases, however for collisionality, this is not a major concern.

Compared to other electric propulsion systems, such as Ion and Hall thrusters, the pulsed plasma thruster is an attractive EP device due to its low mass, low cost, simplicity, robustness, and short development time. Furthermore, as its name indicates, the PPT creates its thrust through a constant series of pulses at a selected frequency, a condition that makes the PPT a more throttle-suitable device (when compared to other EP systems), because not only can the energy per discharge be regulated, but also the pulse frequency. Additionally, thanks to the high electric field that pulsed devices use, the breakdown of air in thin atmosphere is relatively easy, without the requirement of air compression before ignition.

In 2014 at the APL, at the University of Washington, the first Air-Breathing Pulsed Plasma Thrusters were studied [12]. The different prototypes are shown in Figure 1.5; they were all designed to be 8 cm in length and with diameters ranging between 2.5 and 7.6 cm. Maximum specific thrust values of 150 mN/kW were obtained.

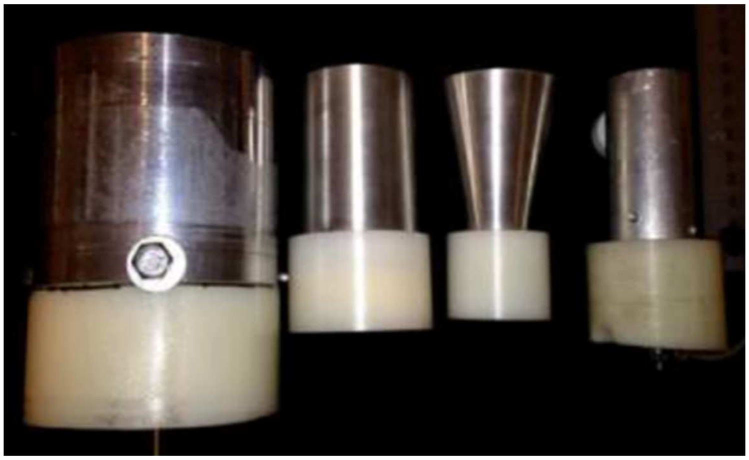

Figure 1.5: Early concepts of the Air-Breathing Pulsed Plasma Thruster developed at the Advanced Propulsion Laboratory (APL) in 2014 [12]. From left to right the diameter of the devices are 7.6, 5, 2.5-5, and 2.5 cm. All of the four concepts were 8 cm in length.

1.4 THE PULSED PLASMA THRUSTER

The conventional in-space Pulsed Plasma Thruster (PPT), is a device in which thrust is produced electrothermally (ET) and electromagnetically (EM), through a train of electrical pulses at a selected frequency, which are created by discharging a large amount of voltage across two electrodes (an anode and a cathode), using a capacitor bank. The contributions of the two acceleration mechanisms vary considerably and depends on the configuration and characteristics of the system. The PPT technology is more than 50 years old and has been an area of active research to date [15]. PPTs exist in different configurations and can be classified mainly by their geometry and fuel feeding mechanism. One of the most common geometrical configurations is the rail-electrode (rectangular) PPT, shown in Figure 1.6.

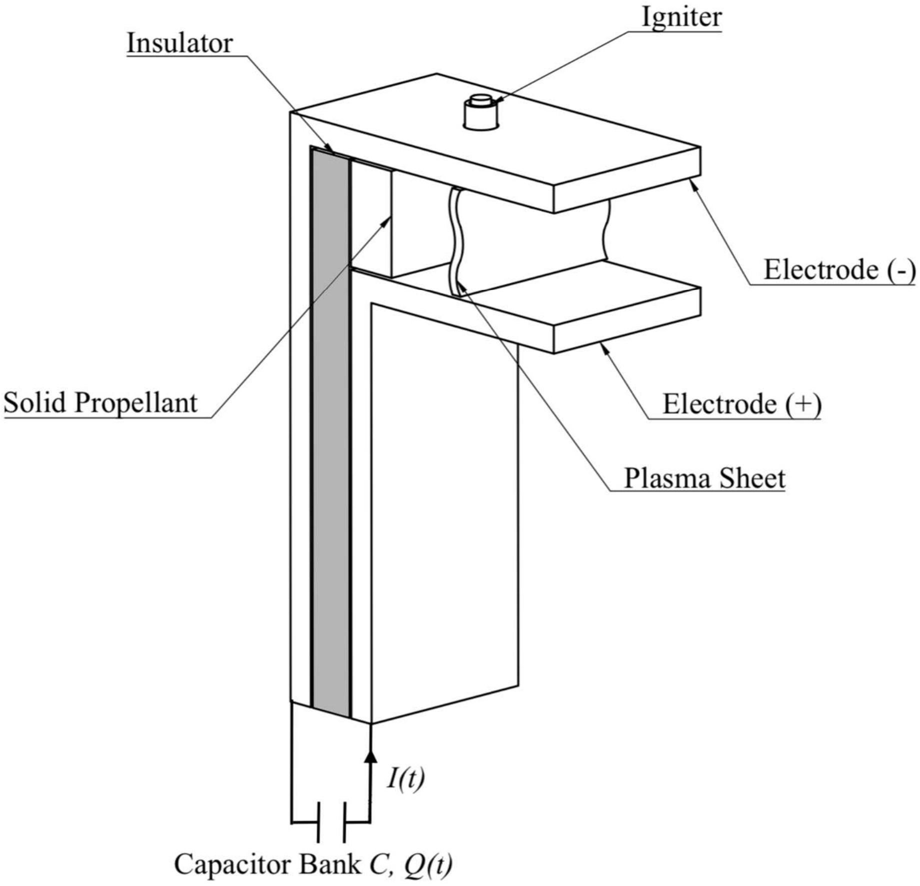

Figure 1.6: In-space breech fed rectangular Pulsed Plasma Thruster configuration.

In this configuration, the current and self-induced magnetic field are primarily transverse to the plasma flow. Variations of this geometry include tongue-shaped electrodes, positioned at different angles (parallel or flared) [16]. The rectangular PPT configuration represents the simplest geometry of PPT configurations.

Figure 1.7 shows another of the most common PPT configurations, the coaxial PPT. This device has a relatively simple design, that consists of a central, cylindrical electrode (anode), and a circular, tubular outer electrode (cathode). Because the ionization of the propellant results from the electrons primarily emitted from the electrodes, and secondary electron emission, in a coaxial

PPT configuration it is customary to have the negative polarity of the capacitor bank connected to the cathode. Unlike rectangular PPTs, the current density and magnetic field profiles in the coaxial PPT configuration, have azimuthal symmetry.

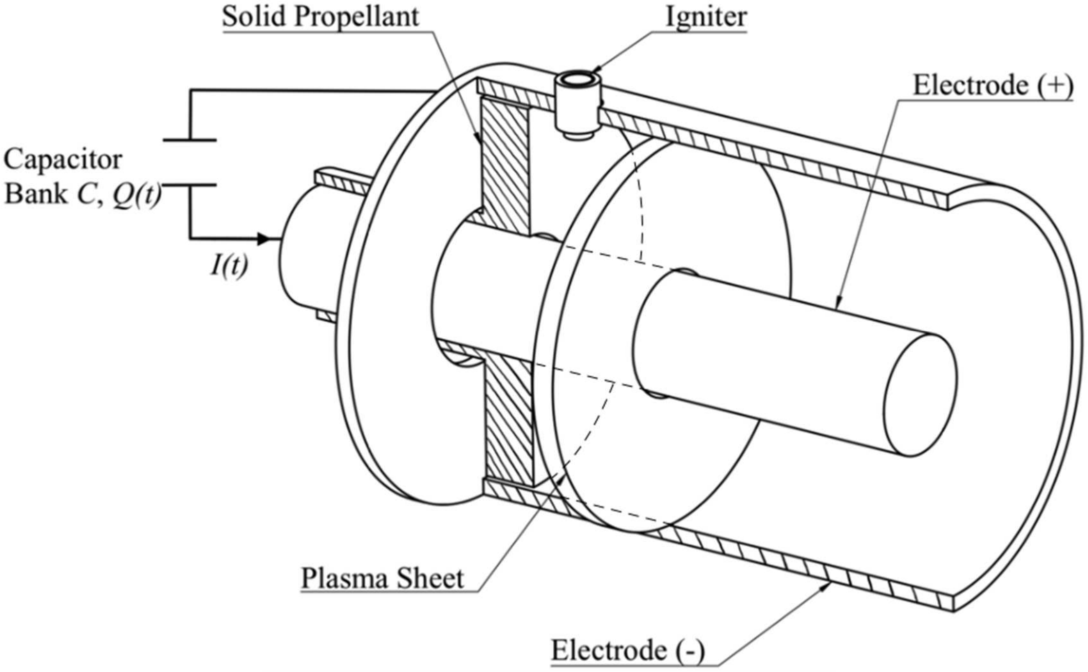

Figure 1.7: In-space, breech-fed, coaxial Pulsed Plasma Thruster configuration.

The second most important characteristic through which PPTs are classified, is the way the fuel is fed into the systems. Two main fuel feeding configurations are: the breech-fed, where the propellant is fed to the chamber from the rear end (opposite to the exhaust nozzle), and side-fed, where the propellant is fed from the sides (at right angles to the electrodes). Other characteristics can also determine their classification, including the propellant type (solid, gas, liquid), short pulse versus quasi-steady, ablation area, igniter plug and nozzle type. Each of these characteristics play an important role in determining the performance of the system, however, discussing these characteristics in detail is outside of the scope of this study.

Independent of the configuration, the principle of operation of pulsed plasma thrusters is generally very similar. An igniter plug provides an initial spark, followed by the main voltage discharge across the electrodes, originating at the capacitor bank. The potential difference ionizes the propellant, creating a current density between the electrodes, which in turn generates a magnetic field. The two resulting acceleration mechanisms of in-space PPTs are: the $\bar{J} \times \bar{B}$ force, and electrothermal, created by Ohmic heating of the ablated mass. The total impulse bit of a pulsed plasma thruster can thus be expressed as,

$$I_{bit} = I_{EM} + I_{ET} \tag{1.4}$$

where I_{EM} and I_{ET} are the impulse created electromagnetically and electrothermally respectively. Typically, the total impulse bit is highly dominated by the electromagnetic term.

Robert G. Jahn [17], describes the efficiency of a rectangular pulsed plasma thruster based on inductance changes during acceleration, i.e. the amount of energy delivered to moving the plasma sheet. Such efficiency is obtained by analyzing the system as a simple inductance-capacitance-resistance (LCR) electric circuit, as shown in Figure 1.8.

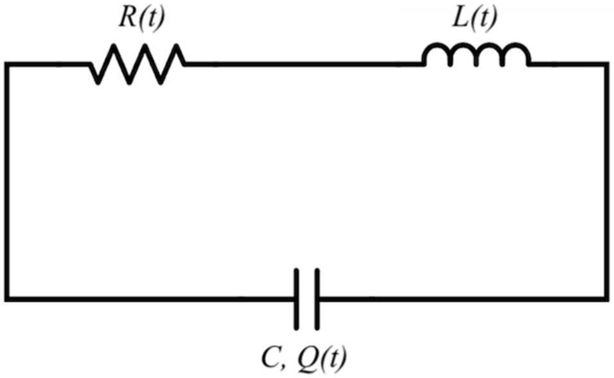

Figure 1.8: Equivalent inductance-capacitance-resistance (LCR) electric circuit of a rectangular pulsed plasma thruster.

where *R(t)* and *L(t)* represent the resistance and the inductance of the moving plasma sheet across the electrodes. The electric circuit is described by equation (1.5).

$$V = IR + \dot{\emptyset} \tag{1.5}$$

where $\dot{\emptyset}$ denotes the change in magnetic flux and is directly related to the inductance. If the total power delivered by the capacitor to the circuit is expressed as $P = IV$, equation (1.5) can be expressed as,

$$P = I^2R + \frac{d}{dt}\left(\frac{1}{2}LI^2\right) + \frac{1}{2}I^2\dot{L} \tag{1.6}$$

The first term represents the rate of resistive heat generation, the second term the rate of change of energy stored in magnetic field, and the last term the rate of work done on moving the plasma sheet. Using the definition of the energy stored in a capacitor, equation (1.6) can be expressed as,

$$E_0 = \frac{1}{2} C V_0^2 = \int_0^\tau P\,dt = \int_0^\tau I^2 R + \frac{d}{dt}\left(\frac{1}{2} L I^2\right) + \frac{1}{2} I^2 \dot{L}\,dt \tag{1.7}$$

Where E_0 and V_0 are the initial energy and voltage per discharge respectively, delivered by the capacitor bank, and τ represents the pulse length. Because the current is zero at $t = 0$ and $t = \tau$, the rate of change of energy stored in the magnetic field (i.e. the term in the middle), disappears from the integration. For in-space PPTs, the resistive heat generation represents a loss in the system. In other words, it is desirable to have most of the energy delivered by the capacitor bank deposited in moving the plasma sheet. Therefore, for in-space PPTs, the efficiency, η, is expressed as,

$$\eta = \frac{1/2 \int_0^\tau I^2 \dot{L}\,dt}{E_0} \tag{1.8}$$

For an air-breathing PPT, the efficiency of the device is also highly dependent on the capacitor energy per discharge, however an air-breathing PPT operates in a highly collisional regime, thus the resistive heat generation in the plasma, i.e. the first term of equation (1.6) doesn’t necessarily represent losses to the thrust efficiency. In fact, as will be seen in the following section, this term has a major contribution to the net thrust. As a result, the efficiency of an air-breathing PPT is typically higher than the efficiency of conventional in-space PPTs.

Chapter 2. PULSED PLASMA THRUSTER FOR ATMOSPHERIC APPLICATIONS

In this section the pulsed plasma thruster for lower atmospheric applications will be described. Because the device was originally intended for propelling an aircraft that could potentially act as an atmospheric satellite in thin atmospheres, the specific thrust (thrust-to-power ratio) is essential and decisive in the study and development of the device. Thus, we will begin by describing the principle of operation, including an analytical derivation for the specific thrust. Additionally, it is expected that the net thrust of the AB-PPT is maximized by having a large background gas pressure, such that during and after the main discharge, the thermal expansion caused by the plasma results in many collisions with the gas neutrals, aiding in the overall thrust of the system. However, in order for these collisions to have the desired effect, the cathode needs to be designed such that the plasma is not diffused in the radial direction. Therefore, based on the probability of ion-neutral collisions, the conditions for the appropriate discharge section dimensions will be determined.

2.1 PRINCIPLE OF OPERATION

Multiple concepts and iterations of the AB-PPT (Air-Breathing Pulsed Plasma Thruster) were investigated at the advanced propulsion laboratory. Each of them is discussed in detail in Chapter 3. Regardless of the variations and complexity of the system, the underlying components and principle of operation of an air-breathing PPT remain similar. Therefore, in order to facilitate the description of the principle of operation, we will employ a diagram of a simplified version of the device. Figure 2.1 shows a coaxial air-breathing PPT, and Figure 2.2 shows a cross section of the system.

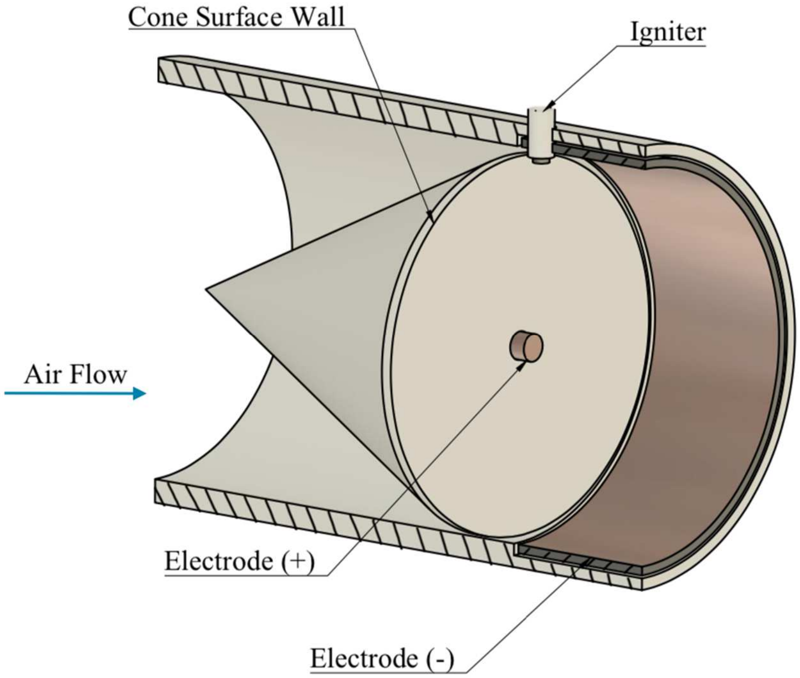

Figure 2.1: Simplified version of a coaxial air-breathing pulsed plasma thruster. The cone-shaped body guides the air to flow into the discharge section. Details such as electrical connections and the nozzle have been omitted.

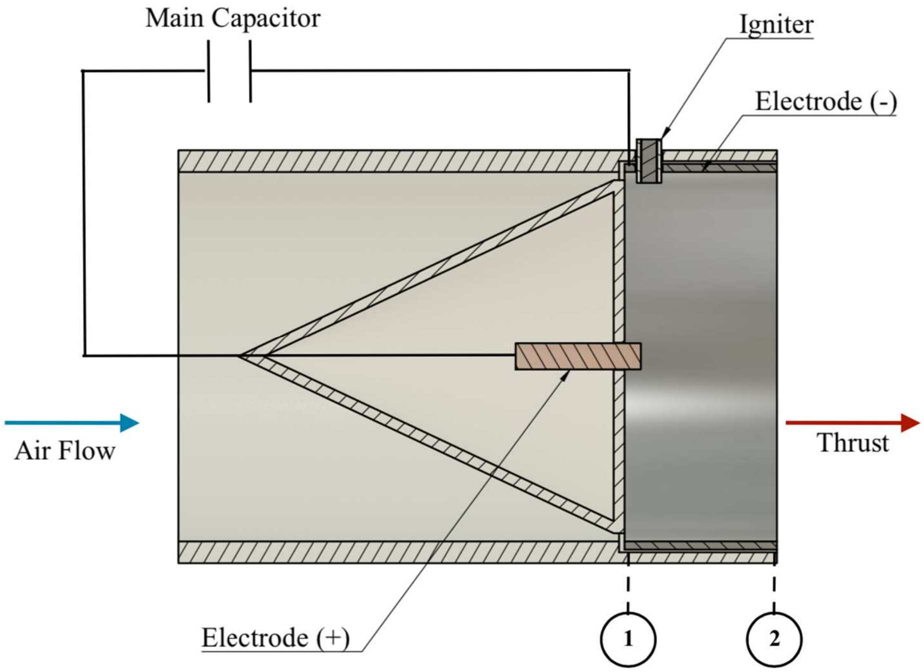

Figure 2.2: Cross section of a coaxial air-breathing pulsed plasma thruster. The cone-shaped body guides the air to flow into the discharge section, i.e. at station 1. The main voltage discharge between the anode and the cathode ionizes the background gases. Station 1 represents the location where breakdown of air occurs, whereas station 2 represents the location where the plasma is fully dissipated.

The components and principle of operation of an air-breathing pulsed plasma thruster are similar to in-space PPTs. A spark plug provides an initial spark, followed by a large voltage discharge between the two electrodes (anode and cathode). An optimal configuration requires the negative polarity of the main capacitor bank to be connected to the cathode, such that a larger flow of electrons is generated, facilitating the ionization of the background air. The main difference between in-space and air-breathing PPTs lies in the following,

1) For an air-breathing PPT no on-board propellant is needed, instead; the background gases of the atmosphere are used. The cone-shaped body allows a smooth flow of air into the discharge section, while preventing the hot gases from escaping through the back of the device after the breakdown of air. In other words, after the breakdown of air occurs, the plasma heats up the surrounding gases, and the hot gases expand in all directions. However, because of the cone-shaped air intake, the gases that expand backwards hit the surface wall, creating thrust in the desired direction.
2) Due to the highly collisional regime in which an air-breathing PPT operates, the generated plasma has multiple collisions with the background neutrals, such that the overall exit velocity is reduced, but the amount of material ejected is greatly increased. As a result, these collisions reduce the overall I_{sp} of the device but increase the specific thrust.

Based on these two premises, an expression for the specific thrust of an air-breathing PPT can be derived starting with the momentum equations for the neutrals, ions, and electrons,

$$m_n n_n \frac{d\mathbf{u}_n}{dt} = -\nabla P_n + \mathbf{R}_{in} + \mathbf{R}_{en} \tag{2.1}$$

$$m_i n_i \frac{d\mathbf{u}_i}{dt} = n_i e(\mathbf{E} + \mathbf{u}_i \times \mathbf{B}) - \nabla P_i - \mathbf{R}_{ie} - \mathbf{R}_{in} \tag{2.2}$$

$$m_e n_e \frac{d\mathbf{u}_e}{dt} = -n_e e(\mathbf{E} + \mathbf{u}_e \times \mathbf{B}) - \nabla P_e - \mathbf{R}_{ei} - \mathbf{R}_{en} \tag{2.3}$$

where $\mathbf{R}_{in}$ and $\mathbf{R}_{en}$ represent the momentum gained by the neutrals due to ion-neutral and electron-neutral collisions respectively. Therefore, these quantities are of particular interest for our analysis.

Combining this set of equations, assuming quasi-neutrality, using the definition of the current density $\mathbf{J} = en_i\mathbf{u}_i - en_e\mathbf{u}_e$, and neglecting the momentum of the electrons, the following expression is be obtained.

$$m_i n_i \frac{d\mathbf{u}_i}{dt} + m_n n_n \frac{d\mathbf{u}_n}{dt} = \mathbf{J} \times \mathbf{B} - \nabla P - \nabla P_n \tag{2.4}$$

Where P and P_n represent the plasma pressure and the neutrals pressure respectively, and the subscripts i and n represent ion, and neutral quantities, respectively. Because we wish to derive an expression to obtain the axial force of the device, equation (2.4) can be solved in cylindrical coordinates,

$$m_n n_n u_n \frac{du_n}{dz} = -\frac{1}{2\mu_0}\frac{dB_\theta^2}{dz} - \frac{d(P + P_n)}{dz} - m_i n_i u_i \frac{du_i}{dz} \tag{2.5}$$

Where the current density is assumed to be purely in the radial direction, and the magnetic field in the theta direction. Integrating over the volume, equation (2.5) can be written as,

$$\int_V m_n n_n u_n \frac{du_n}{dz} dV = -\int_S \left[\frac{1}{2\mu_0} dB_\theta^2 + d(P + P_n) + m_i n_i u_i du_i\right] d\mathbf{S} \tag{2.6}$$

Using the mass conservation for the neutrals, from the point of the entry of air (station 1 of Figure 2.2), to the thruster's exit point (station 2), $\frac{d(n_n u_n)}{dz} = 0$, and if it is assumed that at station 1 is where the plasma initiates, and station 2 is where the plasma is fully dissipated, the following assumptions can be used: $B_{\theta 1}^2 \gg B_{\theta 2}^2$, $u_{i1} \gg u_{i2}$, $P_1 \gg P_2$, and since $u_{n2} \gg u_{n1}$, $P_{n2} \approx 0$. Thus, to obtain the force in the axial direction, equation (2.6) can be reduced to the following form,

$$F_z = \frac{A}{2}\left[\frac{B_{\theta 1}^2}{\mu_0} + m_i n_{i1} u_{i1}^2 + 2(P_1 + P_{n1})\right] \tag{2.7}$$

where A is the exhaust area of the air-breathing PPT, $A = \pi(r_2^2 - r_1^2)$; r_2 and r_1 being the radius of the cathode and radius of the anode respectively. In order to obtain the specific thrust, equation (2.7) is integrated over the pulse length and divided by the energy per discharge, $E_c = \frac{1}{2}CV^2$.

$$T_{sp} = \frac{\pi(r_2^2 - r_1^2)}{2E_c}\int\left[\frac{B_{\theta 1}^2}{\mu_0} + m_i n_{i1} u_{i1}^2 + 2(P_1 + P_{n1})\right]dt \tag{2.8}$$

Equation (2.8) represents the specific thrust of an air-breathing PPT as a function of the measurable plasma parameters, ion density (n_i), ion speed (u_i), magnetic field (B), and plasma pressure (P). The contribution to the specific thrust can be divided into three different mechanisms, 1) electromagnetic, corresponding to the first term inside the brackets, 2) electrostatic, corresponding to the second term inside the brackets, driven by the electric field across the length of the cathode during the main discharge, and 3) ion-neutral collisions, corresponding to the last term on the right side inside the brackets, driven by electrothermal expansion (P_1) and the ambient pressure (P_{n1}). In other words, the higher the plasma temperature and background pressure of the atmosphere, the more collisions will occur. The specific thrust heavily relies on the diameter of the device through the first term in equation (2.8), i.e., a larger diameter would result in greater values of specific thrust. However, a larger diameter will also require a larger amount of voltage per discharge, reducing the values of specific thrust. This condition is described by the Paschen's law, which indicates the required voltage to ionize a specific gas, for a given distance between the electrodes and the background gas pressure. This condition will be discussed in more detail in section 3.2.2. Additionally, increasing too much the cathode's diameter would increase the size of the system, and thus its overall weight. The ion-neutral collisions are determined by the background gas pressure. The greater the background gas pressure, the greater the specific thrust. However, a higher background gas pressure will also require a larger voltage per discharge. The characteristic plasma parameters to obtain the electromagnetic and electrostatic contributions are determined by E_c. Although the specific thrust is inversely proportional to the energy per discharge, a minimum voltage per discharge is needed in order to ionize the air and generate the different acceleration mechanisms. Additionally, a lower voltage source could potentially lead to a reduction in the values of the plasma parameters and pulse length. Experimentally validating equation (2.8) is therefore essential in the investigation of an air-breathing PPT.

2.2 CATHODE LENGTH ESTIMATION

In this section, the condition to determine the optimal geometrical configuration of the cathode of an air-breathing PPT is determined. Equation (2.8) shows the importance of having a large cathode diameter. However, its length and its impact on the thrust of the device have not yet been discussed. Because the thrust is presumably produced mainly through ion-neutral collisions, the condition $\mathrm{P_r} < \mathrm{P_z}$, where $\mathrm{P_r}$ and $\mathrm{P_z}$ are the probability of collisions in the cathode's wall plane and the exit plane respectively, needs to be satisfied. If such condition is violated, the plasma will diffuse mainly in the radial direction, rather than in the desired axial direction, reducing the net thrust obtained from the device.

The total number of neutrals in the discharge section of the air-breathing PPT is given by $N_n = n_n V = n_n A_1 dz$, where n_n is the number of neutrals per unit volume, V is the volume of the discharge section of the device, and A_1 is the cross sectional area of the discharge section. The probability of collisions in the exit plane and the cathode's wall plane can be written as,

$$\mathrm{P_z} = \frac{N_n \sigma}{A_1} = \frac{n_n A_1 dz\sigma}{A_1} = n_n dz\sigma \tag{2.9}$$

$$\mathrm{P_r} = \frac{N_n \sigma}{A_2} = \frac{n_n A_1 dz\sigma}{A_2} = \frac{n_n dr\sigma}{2} \tag{2.10}$$

where σ represents the cross-sectional area of the neutrals, and A_2 the area of the cathode's wall, $A_2 = 2\pi r dz$. The condition $\mathrm{P_r} < \mathrm{P_z}$ can then be expressed in terms of the radius (r) and the length (z) of the air-breathing PPT as,

$$2z > r \tag{2.11}$$

In order to maximize the thrust of an air-breathing PPT, expression (2.11) needs to be satisfied. As will be seen in the next section, violating such a condition will result in a significant reduction of the net thrust produced by the device. Because the momentum is transferred to the neutrals when the plasma is dissipated, the maximum length of the cathode is determined by the full dissipation of the plasma. Increasing the length of the cathode indefinetely, could potentially result in a larger fraction of the neutrals colliding with the wall of the device, in addition to adding extra weight to the system. Therefore, for an optimal size of the discharge section, condition (2.11) can be expressed as $2z \cong r$. At this point the neutrals carry the momentum, ideally in the axial direction. However, some of these neutrals are directed in the radial direction. Thus, in order to redirect their momentum in the axial direction, the addition of a nozzle to the system is considered.

Chapter 3. AIR-BREATHING PULSED PLASMA THRUSTER (AB-PPT)

In this section, the multiple iterations of the Air-Breathing Pulsed Plasma Thruster studied at the APL will be discussed. From this point, we will refer to the Air-Breathing Pulsed Plasma Thruster as AB-PPT. Considering that the device was originally intended for propelling an aircraft that could potentially act as an atmospheric satellite in thin atmosphere, the specific thrust, i.e. the net force obtained per input energy, is an essential and decisive parameter in the study and for the development of an atmospheric satellite. Therefore, in this section we will start by introducing the experimental setup, including the pulsed power electronics, and pendulum-based thrust stand that was used for measuring the specific thrust of the different prototypes studied at the APL. We will then describe the different AB-PPTs developed through this time, starting with the daisy-shaped cathode AB-PPT, the first iteration with the variable spacing electrode mechanism, and the final AB-PPT design, with which the desired specific thrust values of 450 mN/kW were achieved, making an atmospheric satellite a near-term reality.

3.1 EXPERIMENT SETUP

The multiple iterations of the AB-PPT presented in this chapter, were studied in our bell-jar shaped vacuum chamber (Figure 3.1), with a volumetric capacity of 0.14 m^3. Because the device is originally intended for operations at terrestrial atmospheric altitudes between 20 and 30 km, the experiment was performed using background air pressures corresponding to these altitudes, i.e. 50-10 Torr.

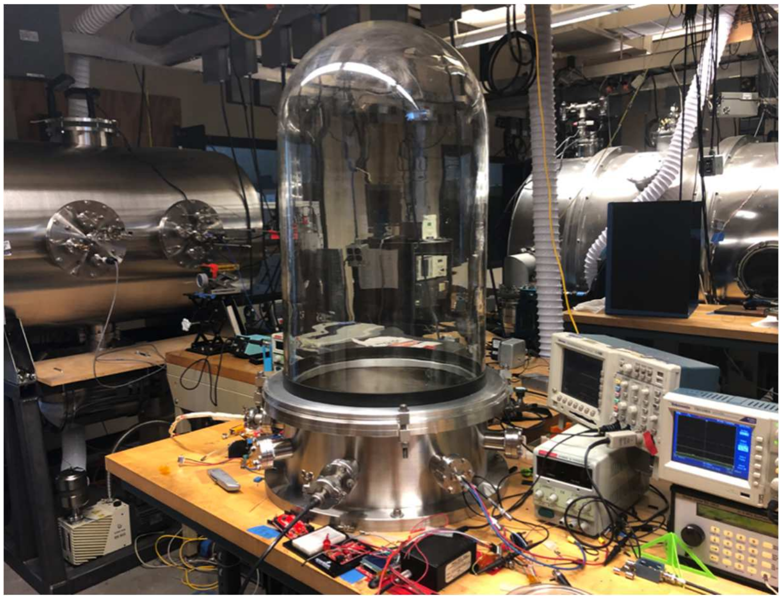

Figure 3.1: Bell-jar shaped vacuum chamber with a volumetric capacity of 0.14 m^3 used to test the multiple iterations of the AB-PPT at the APL.

In order to generate the main voltage discharge to ionize the background air, a power supply was constructed in-house, which was capable of delivering up to 1.5 kV per discharge. Figure 3.2 shows a simplified version of the circuit diagram used for the experiment.

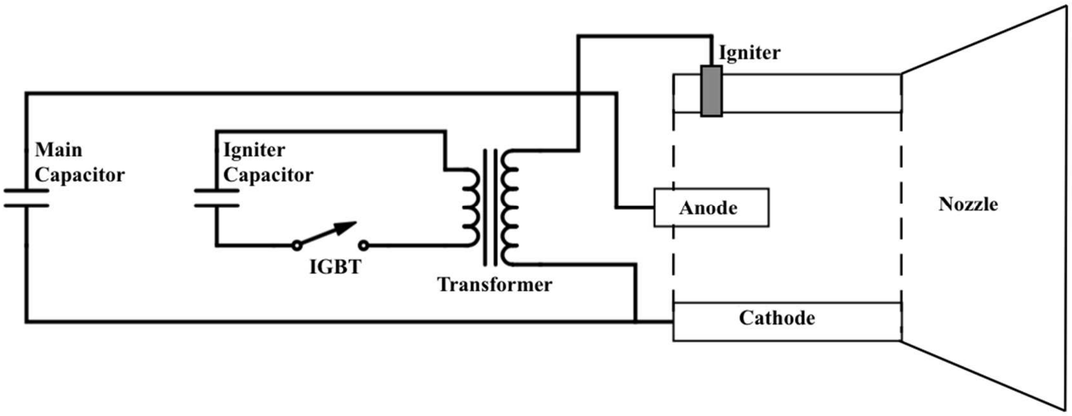

Figure 3.2: Simplified circuit diagram for the AB-PPT experiment.

The main discharge capacitor bank is comprised of eight 5 μF polypropylene capacitors, rated at 1.5 kV, connected in parallel for a total capacitance of 40 μF. In order to obtain the largest possible flow of electrons in the system to facilitate the ionization of air, the negative polarity was connected to the outer electrode (cathode), and the positive polarity was connected to the centered electrode (anode). Additionally, in order to reduce stray inductance, the length of the wires connecting the capacitor bank and the electrodes was kept as short as possible – approximately 5 cm. Although no thorough analysis was performed as to how the performance of the device varies with length of the connections, and whether the wires are twisted or not, it is well-known that stray inductance can have a negative effect on the performance of the thruster. This effect was noticed in the experiment performed by Paige et al. [18], which made use of similar high-power electronics used for this experiment. The igniter circuit consists of a secondary capacitor charged at 300 Volts, a 1:100 step-up toroidal transformer and an Insulated Gate Bipolar Transistor (IGBT) switch. The two ends of the transformer were connected, one to the igniter and the other to the cathode.

In order to measure the specific thrust of the AB-PPTs, and in-house designed and constructed aluminum pendulum-based thrust stand was used. Figure 3.3 and Figure 3.4 shows the CAD model and isometric views of the thrust stand respectively.

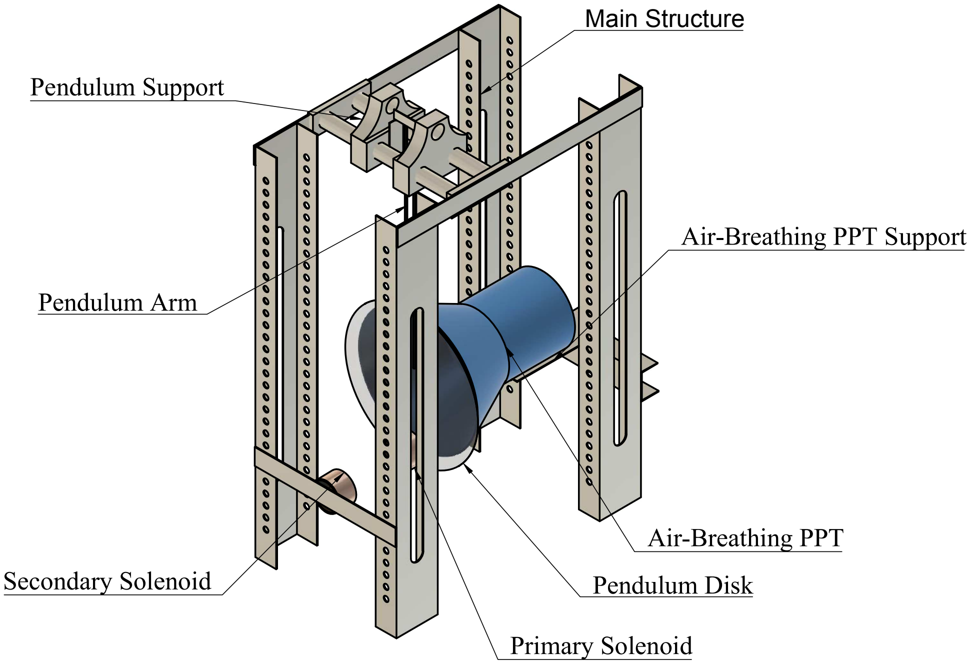

Figure 3.3: CAD model of the pendulum-based thrust stand, used to measure the specific thrust of the different iterations of the AB-PPT.

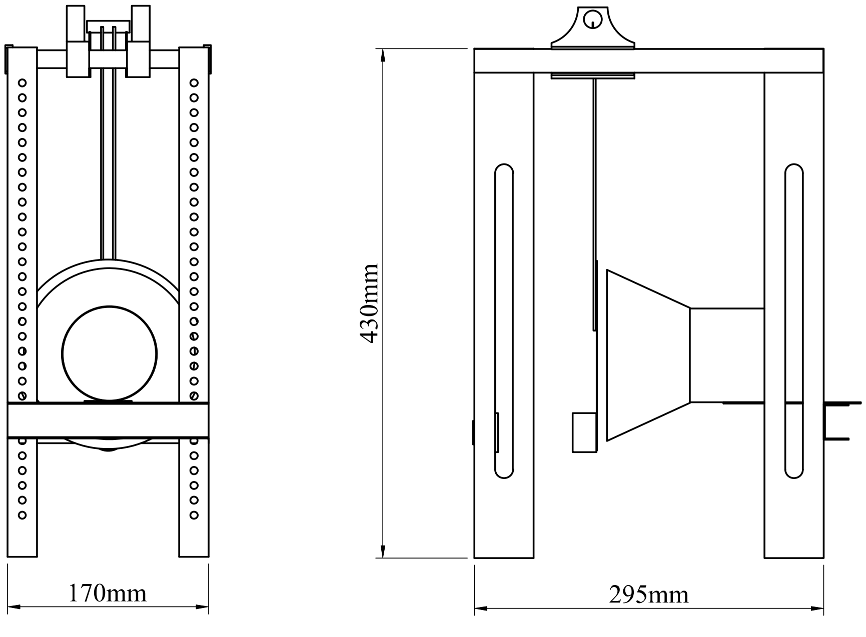

Figure 3.4: Side view and front view of the pendulum-based thrust stand with dimensions.

The thrust stand consists of an aluminum structure, with a support to place the AB-PPT, and a 100 grams pendulum suspended from the two upper beams. The pendulum disk was made of acrylic, and in order to minimize the friction between the pendulum and the main structure, a razor blade was used as the pivot point. In order to obtain the pendulum's deflected angle, two solenoids were placed, one on the pendulum (connected to an oscilloscope), and the other one to the thrust stand (connected to a function generator). After the main voltage discharge of the AB-PPT, the pendulum swings back and forth, triggering the voltage signal from the solenoid connected to the oscilloscope. This voltage signal was compared and interpolated with the angle measured with a video camera. Figure 3.5 shows a typical raw data obtained from the solenoid connected to the pendulum, and Figure 3.6 shows a picture with the AB-PPT and pendulum before, during, and after the main discharge.

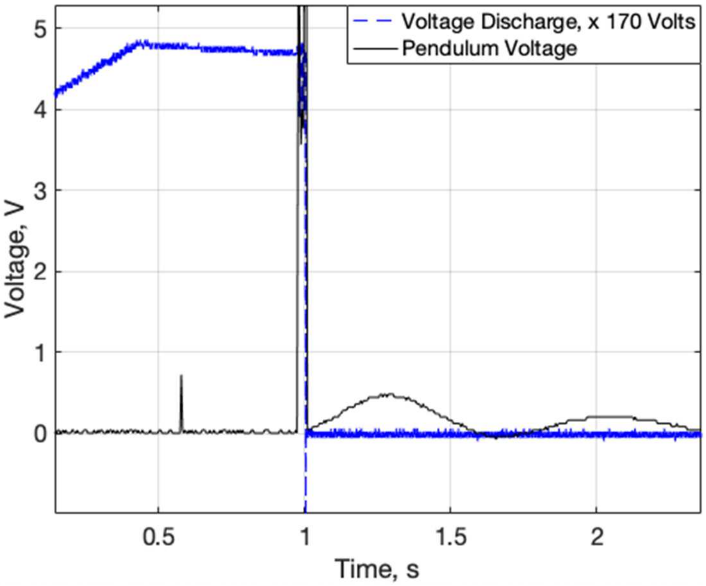

Figure 3.5: Typical pendulum raw data after the main discharge of the AB-PPT occurred. The maximum (first) peak of the sinusoidal voltage signal was used as the deflected pendulum angle.

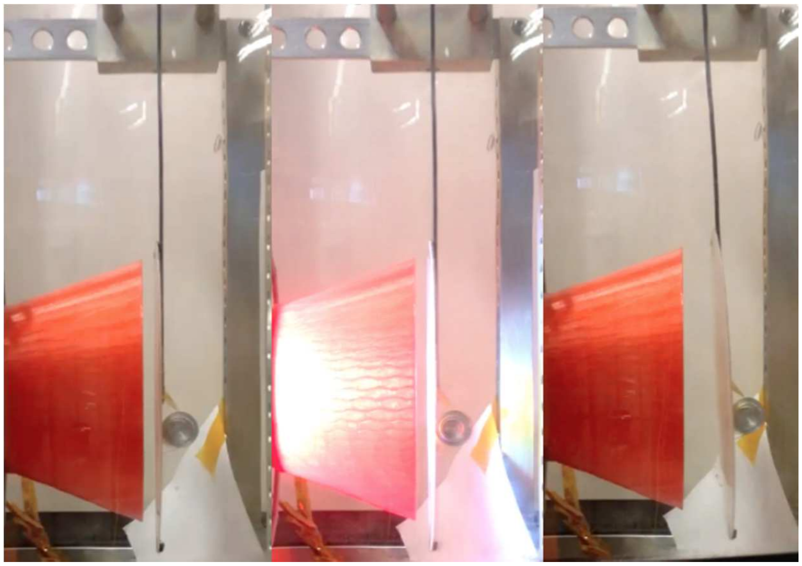

Figure 3.6: Sample comparison picture of the AB-PPT and pendulum; before, during and after the main discharge.

The first peak of the sinusoidal signal represents the point of maximum deflection of the pendulum; therefore, this point was compared to the angle obtained from the video-camera. Figure 3.7 shows the correlation between the pick-up voltage and the corresponding pendulum deflected angle.

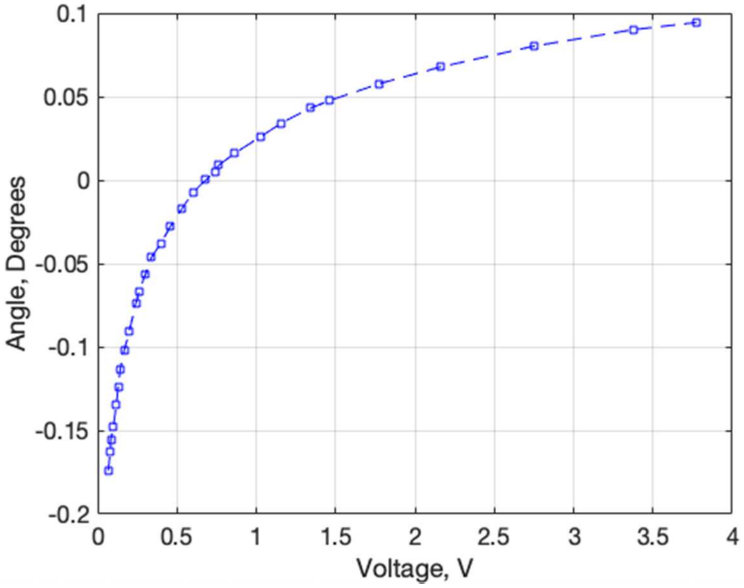

Figure 3.7: Correlation between the maximum (first) peak of the pick-up sinusoidal voltage signal and the corresponding pendulum deflected angle.

After the pendulum reaches its maximum angular position, it swings back, causing a negative deflected angle. Thus, in order to obtain an accurate correlation between the pick voltage and the pendulum deflected angle, the zero-degree position of the pendulum was set at an output solenoid voltage of 0.7 V. The impulse bit of the pendulum can be obtained using the deflected angle and energy conservation, i.e. $E_P = E_K$, where E_P is the potential energy, and E_k is the kinetic energy. Using a small angle approximation, the potential energy (E_P) can be expressed as,

$$E_P = m_p g d_p (1 - \cos\theta) \tag{3.1}$$

Where m_p represents the mass of the pendulum, d_p the distance from the center of mass to pivot, and θ the deflected angle. For the pendulum used in the experiment, $m_p = 100$ grams, and $d_p = 24.5$ cm. Because we are interested in the impulse bit of the pendulum, the kinetic energy (E_K) can be written in terms of the angular momentum ($L = I_p\omega$) as,

$$E_K = \frac{1}{2} I_p \omega^2 = \frac{1}{2}\frac{L^2}{I_p} \tag{3.2}$$

Where ω represents the angular velocity, and I_p the pendulum moment of inertia. An expression to calculate the impulse bit of the pendulum can be obtained combining equations (3.1) and (3.2). Additionally, we can relate the angular momentum (L) to the linear momentum (P) through the distance from impact to pendulum pivot ($L = Pr_p$) – for the experiment, $r_p = 26$ cm. The expression to determine the impulse bit for a given deflected angle per discharge is then given as,

$$I_{bit} = \frac{\sqrt{2gm_p d_p I_p (1 - \cos\theta)}}{r_p} \tag{3.3}$$

The specific thrust values are calculated dividing the specific impulse by the total capacitor bank energy per discharge, $E_c = \frac{1}{2}CV^2$.

$$T_{sp} = \frac{I_{bit}}{E_c} = \frac{2\sqrt{2gm_p d_p I_p (1 - \cos\theta)}}{r_p C V^2} \tag{3.4}$$

Where E_c, V, and C are the energy per discharge delivered by the main capacitor bank, the voltage per discharge, and capacitance respectively. Finally, a calibration was performed by impacting the pendulum with an object with known mass and momentum. This calibration process placed an uncertainty of ±10% to the specific thrust measurements.

3.2 EARLY DESIGNS

The system presented in section 3.3, with which specific thrust values of more than 400 mN/kW were achieved, resulted after studying different concepts and iterations of the AB-PPT. In Chapter 2, the principle of operation of the device, and the basic geometrical design considerations were discussed. However, there are key elements that were addressed experimentally through the development of the system. Such elements include the air intake, the electrodes (cathode and anode) configuration, and the igniter configuration. The different prototypes of the AB-PPT studied through this time, can be summarized as follows:

1) AB-PPT with a daisy-shaped cathode.
2) First iteration of the AB-PPT with the addition of a variable spacing electrode mechanism.
3) Final iteration of the AB-PPT with the addition of the variable spacing electrode mechanism.

3.2.1 *AB-PPT with a Daisy-Shaped Cathode*

Two different configurations of the AB-PPT using a daisy-shaped cathode were studied. Figure 3.8 shows a front view picture of both configurations of the AB-PPT with a daisy-shaped cathode. First iteration is shown on the left, and the second iteration is shown on the right.

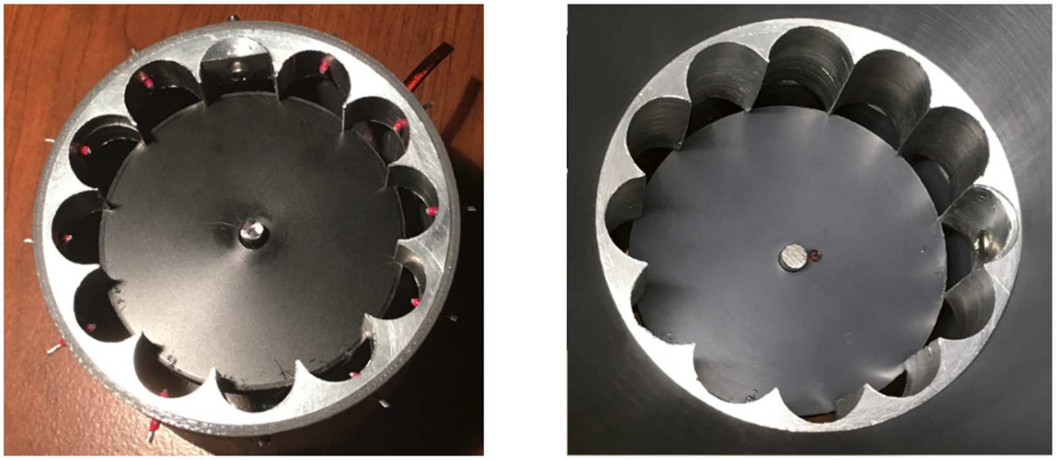

Figure 3.8: Front view picture of the Air-Breathing Pulsed Plasma Thruster with a daisy-shaped cathode. First iteration is shown on the left, and second iteration is shown on the right.

This configuration is similar to the one used for the CubeSat propulsion system, studied at the Advanced Propulsion Laboratory at the University of Washington [18]. The addition of the daisy-shaped cathode to the AB-PPT results in overall improvements in terms of the specific thrust and has two main advantages.

1) It allows air into the discharge section from the back of the system (rear end), while preventing the hot gases from escaping through the back of the device after the breakdown of air. In other words, after the breakdown of air occurs, the plasma heats up the surrounding gases, and the hot gases expand in all directions. Because of the daisy-shaped cathode, the gases that expand backwards hit the surface wall, creating thrust in the desired direction. Although there are hot gases escaping from the rear end through the incoming air gaps, most of the gases escape in the opposite direction through the nozzle. This was confirmed during experimentation, when adding different elements to the back of the thruster such as fans, and no movement in such elements was observed after the discharges.

2) When compared to the traditional cylindrical configuration, the daisy-shaped configuration enables enhancement of the electric field, which also aids in the overall thruster efficiency. Paige E. Northway et al. [18], provides an analysis and comparison of the electric field between a cylindrical cathode and the daisy-shaped cathode for an in-space PPT.

Figure 3.9 shows the first iteration of the AB-PPT using a daisy-shaped cathode configuration.

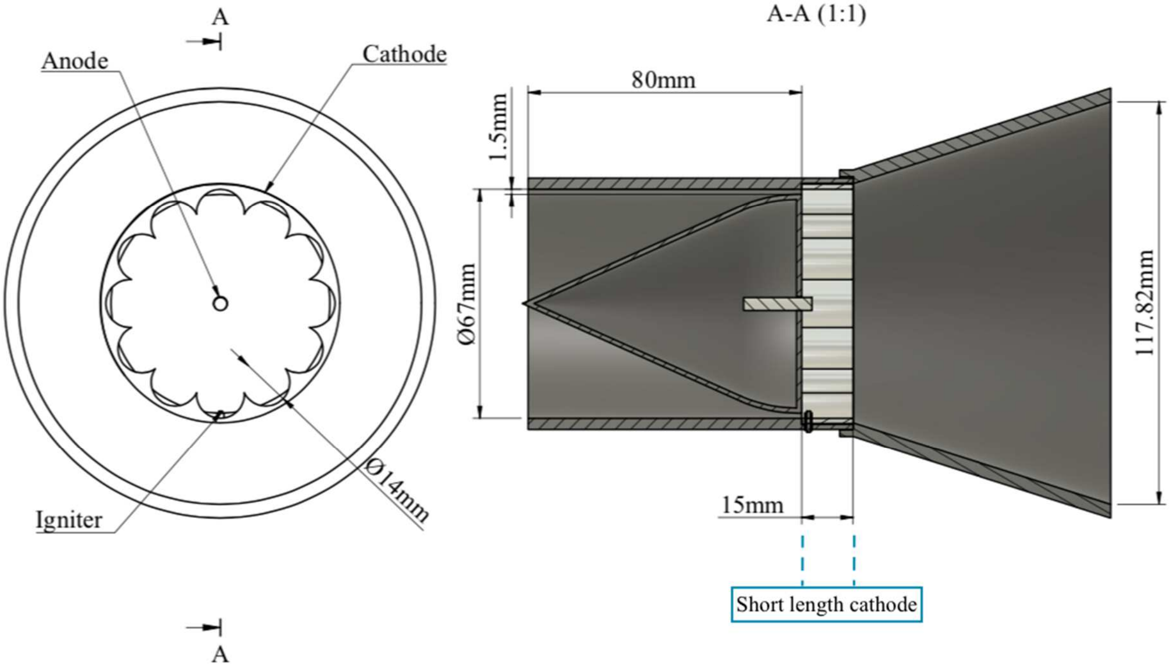

Figure 3.9: First iteration of the AB-PPT using a daisy-shaped cathode configuration. Cathode's length of 15 mm. Specific thrust measurements of less than 100 mN/kW were obtained using the pendulum based thrust stand. (*Electric connections not shown in this figure*)

For this configuration, the daisy-shaped cathode consisted of 12 “peaks”, 67 mm in diameter, and 15 mm in length. Additionally, the part was made of aluminum. The air intake system consisted of a simple cone-shaped design, with a 1.5 mm gap between the cone and the wall of the device, to allow the incoming air into the discharge section. Because the speed of the aircraft, powered with the AB-PPT, is relatively small when compared to the exhaust velocity, the addition to the device of a system to accelerate the incoming air seems necessary, however, the pulsed nature of the device enables the discharge section of the system to refill between pulses through normal airflow. In order to calculate the time that it takes to refill the system with air, the following expression can be used.

$$t = \frac{V\rho}{\dot{m}} = \frac{V}{v_a A} \tag{3.5}$$

where V is the volume of the device to be filled up with gas, v_a the aircraft velocity relative to the wind speed, and A the air inlet area. For an aircraft speed of 7 m/s, the time it would take to fill up the AB-PPT shown in Figure 3.9 with air, would be approximately 25 milliseconds. A typical discharge frequency of the device is 10 Hz, thus air flow does not represent a problem for the system. From conservation of mass flow and Bernoulli’s equation for flows at low Mach number, the pressure at the breakdown point can be expressed as

$$\frac{\rho v_a^2}{2}\left(1 - \left(\frac{A_1}{A_2}\right)^2\right) + P_i = P_o \tag{3.6}$$

where A_1 is the area at the point of the entry of air, and A_2 the area at the breakdown point respectively, and P_i and P_o are the incoming air pressure, and the pressure at breakdown point respectively. The air density (ρ) in the 20-30 km range is approximately 0.09-0.02 kg/m^3, and considering that the area of the incoming air and the area at the point of breakdown are approximately the same, equation (3.6) can be reduced to $P_i \cong P_o$. Since the acceleration mechanism of the AB-PPT is presumably mainly through ion-neutral collisions, the proposed air-intake design, in combination with the daisy-shaped cathode, also helps in preventing net thrust in the opposite direction of the exit nozzle. Finally, unlike propulsion systems that use converging-diverging nozzles to accelerate the hot gases to create thrust, such as chemical and electrothermal thrusters, the addition of a nozzle to the AB-PPT helps directing the momentum of the heavy particles during the collisions process in the axial direction of the thrust. In other words, after the plasma is fully dissipated (point 2 of Figure 2.2), some of the particles are directed in the radial direction, thus the nozzle helps directing the momentum by bouncing these particles in the axial direction. The nozzle was 75 mm in length, with an area ratio of 1:1.75, with an aperture angle of 23 degrees. Specific thrust measurements with and without the nozzle, indicate an increase of approximately an average of 200% with the addition of the nozzle.

The first iteration of the AB-PPT using a daisy-shaped cathode configuration was tested using the thrust stand shown in Figure 3.3. Maximum specific thrust values of less than 100 mN/kW were obtained. Such values are relatively small when compared to the specific thrust values obtained with the concepts studied in 2014 [12]. These results support and suggest that the condition (2.11) must be satisfied to maximize the net thrust. For this iteration of the AB-PPT using the daisy-shaped cathode configuration, the length of the cathode is too short, resulting in the violation of condition (2.11). Figure 3.10 shows the second iteration of the AB-PPT using a daisy-shaped cathode configuration.

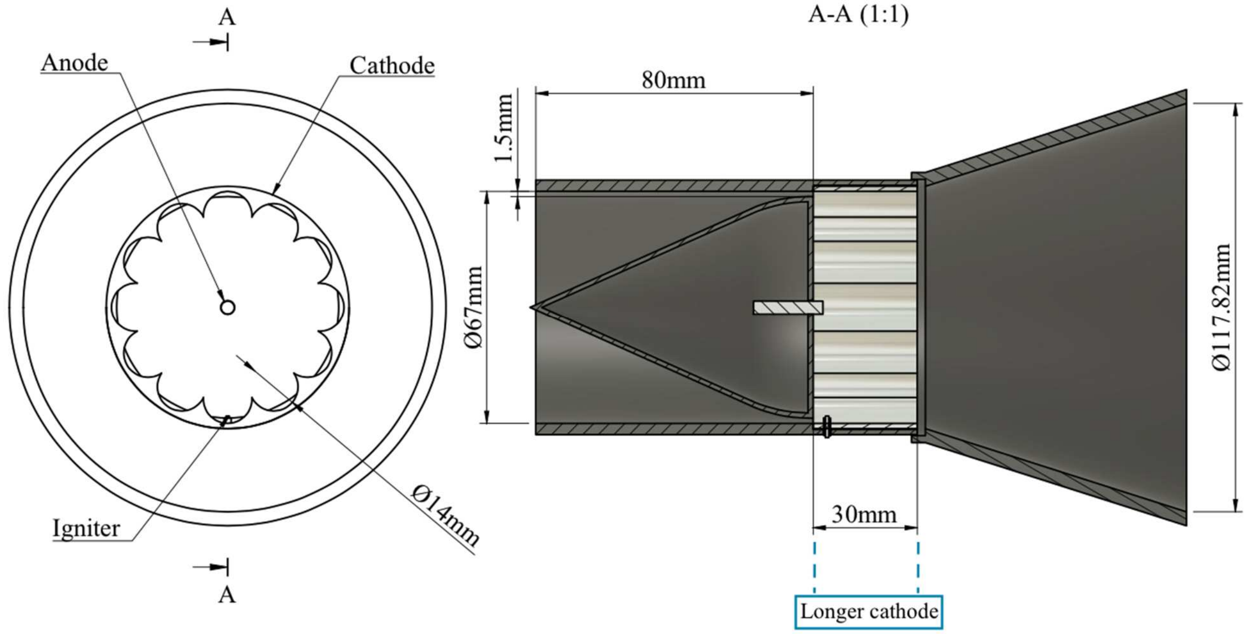

Figure 3.10: Second iteration of the AB-PPT using a daisy-shaped cathode configuration. Except for the length of the cathode, the dimensions of the device are similar to the previous daisy-shaped cathode PPT. Specific thrust measurements of 470 mN/kW were obtained using the pendulum based thrust stand. (*Electric connections not shown in this figure*

Similar to the first iteration, the daisy-shaped cathode consisted of 12 “peaks”, 6.7 cm in diameter, but 30 mm in length, i.e. twice the length of the first iteration, such that the condition $2z > r$ is satisfied. The rest of the components, including the air intake system, and nozzle were kept the same. The second iteration of the AB-PTT with the daisy-shaped cathode configuration was also tested in the pendulum-based thrust stand. Maximum specific thrust values of 470 mN/kW were achieved, at a background gas pressure of 22 Torr. For both of the AB-PPT configurations with the daisy-shaped cathode, the igniter was placed near the cathode, as shown in Figure 3.11.

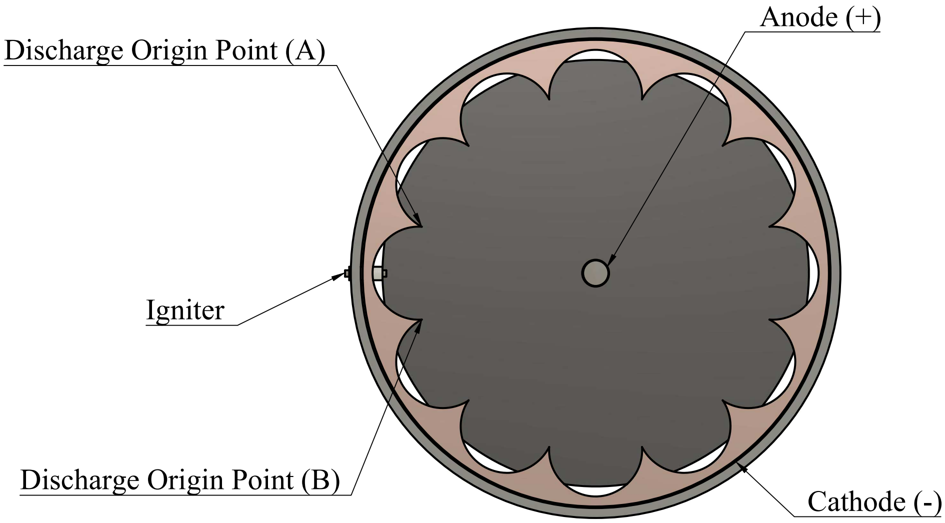

Figure 3.11: Igniter location in both of the daisy-shaped cathode AB-PPT configurations. Details such as the nozzle and electrical connections have been omitted in this figure.

This igniter location is typically used for cylindrical-cathode PPT configurations. However, in the daisy-shaped cathode configuration, the main discharge is initiated at one of the points near the igniter, i.e. either point A or point B of Figure 3.11. This causes such located cathode peaks to wear off faster than the rest of the peaks, reducing the lifetime of the system. Different igniter configurations have been studied and incorporated to the improved iterations of the AB-PPT. These igniter configurations, in addition to the improved iterations of the AB-PPT will be discussed in the following sections.

3.2.2 *Addition of the Variable Spacing Cathode Mechanism*

The addition of the daisy-shaped cathode to the early cylindrical designs, resulted in a considerable improvement in terms of the amount of the specific thrust obtained. However, a fixed cathode diameter is only ideal for a given background gas pressure, and a voltage per discharge. This condition is described by the Paschen's law,

$$V_b > \frac{BPd}{\mathrm{In}(Pd) + C} \tag{3.7}$$

which relates the three key variables for the breakdown of a certain gas in a parallel plate electrode configuration; background gas pressure (P), minimum voltage per discharge needed to ionize the background gases (V_b), and distance between the electrodes (d). Multiple experimental studies have been performed for different types of gas; such is the case of the study carried out by E. Husain et al. [19], which includes the breakdown of air in the analysis.

Additionally, and most importantly, experimental measurements of the air-breathing PPTs performed in 2014, indicate that the specific thrust is maximized by keeping the energy per discharge at minimum, i.e. just enough to ionize the background air [12]. Considering that the device is intended to operate in a wide range through the atmosphere, a mechanism to adjust the electrode separation based on the background gas pressure was added to the system. With this addition, the product (Pd), and the voltage per discharge (V_b) remain constant, maximizing the amount of specific thrust of the device, over a wider pressure range. The first iteration of the AB-PPT with the addition of the variable spacing cathode mechanism is shown in Figure 3.12.

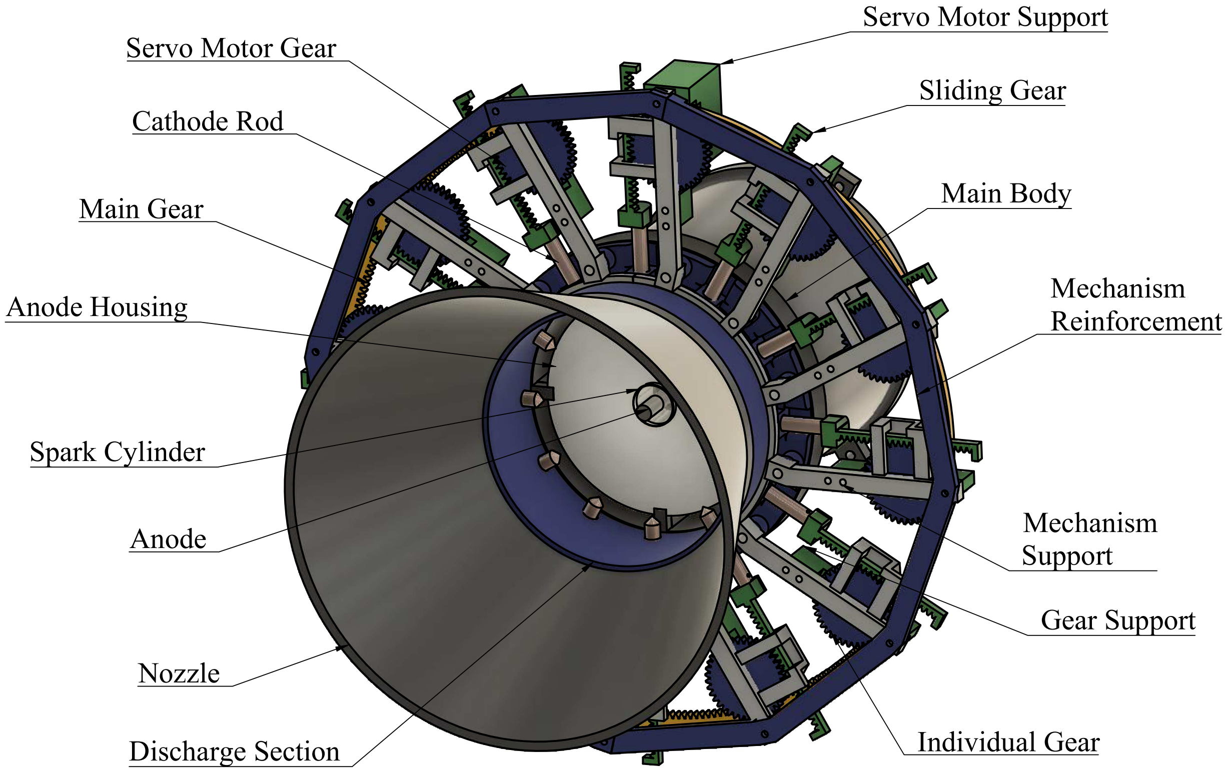

Figure 3.12: First iteration of the AB-PPT with the addition of the variable spacing cathode mechanism.

The first iteration of the AB-PPT with the addition of the variable spacing cathode mechanism was published in 2017 at the 53rd AIAA/SAE/ASEE Joint Propulsion Conference [20]. It has a total length of 250 mm and has several innovations including the variable electrodes to allow optimal operation at different altitudes, and a cylindrical igniter configuration.

Because the daisy-shaped cathode is a rigid body, in order to enable movement of the electrodes; the cathode used for the first iteration of the AB-PPT with the addition of the variable spacing cathode mechanism was replaced by 12 copper rods, as shown in Figure 3.12 and Figure 3.14. The rods were 33 mm in length, and each of them had sharp points to facilitate the arc discharge between the electrodes.

The variable spacing cathode mechanism consists of 12 individual gears, with one of them attached to a servomotor, which is connected to a pressure sensor. When the background air pressure is in the range corresponding to a > 20 km of altitude, the servomotor starts operating. Each of the individual gears actuates a gear bar. The 12 gear bars are then attached to the 12 copper rods that form the cathode in a circular pattern. The individual gears are synchronized with a 200 mm diameter inner gear. When the gear connected to the servo operates, it moves the 200 mm diameter inner gear, which in turn moves the other 11 gears. The 12 gears then move the gear bars, which cause the copper rods to slide in and out in a 28-73.2 mm diameter range. Figure 3.13 shows the first iteration of the AB-PPT with the addition of the variable spacing cathode mechanism, at three different positions: 28, 55 and 73.2 mm diameter.

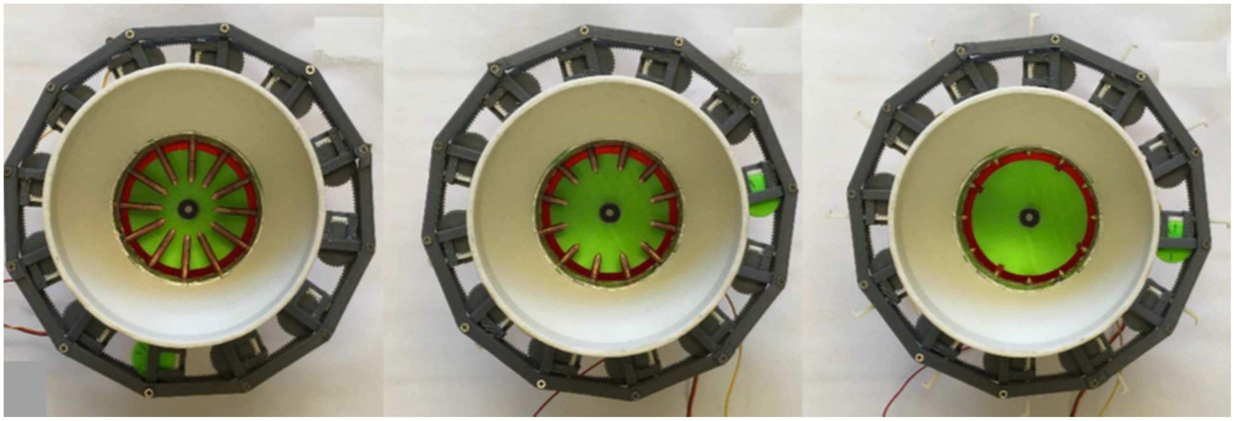

Figure 3.13: First iteration of the AB-PPT with the variable spacing cathode mechanism at three different positions. From left to right, 28, 55, and 73.2 mm diameter.

The main discharge section is 35 mm in length, with 12, 5 mm diameter holes, evenly distributed around the discharge section for the cathode rods access. Additionally, the cathode rods were connected to each other in series with copper wire.

Similar to the daisy-shaped cathode configurations, the main discharge initially occurs where the igniter is located. This situation represents a major concern regarding the lifetime of the device, as the cathode rod/peak where the breakdown of air occurs would wear off faster than the rest of the rods/peaks. To solve this, a cylinder-shaped igniter surrounding the anode was chosen, as shown in Figure 3.14.

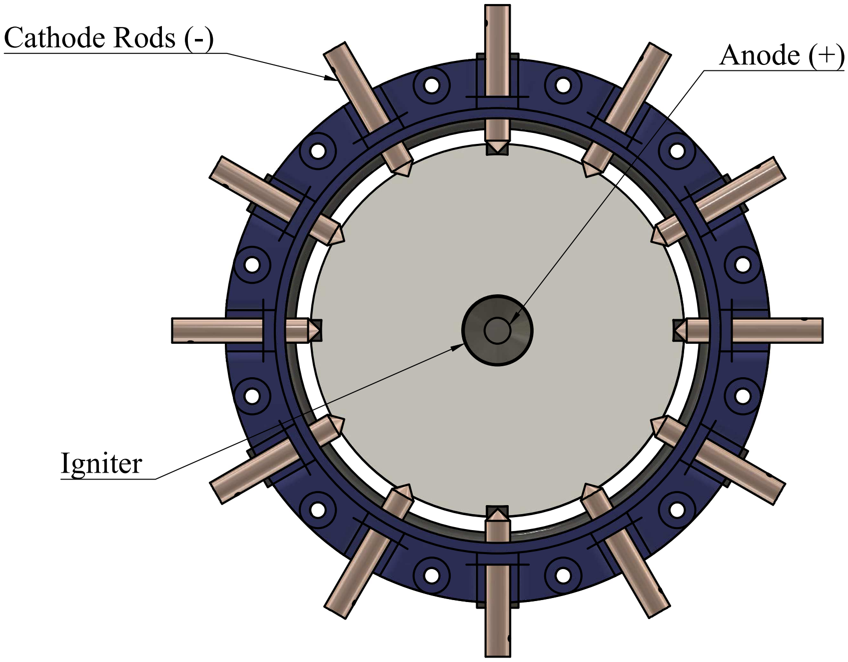

Figure 3.14: Igniter configuration in the first iteration of the AB-PPT with the addition of the variable spacing cathode mechanism. Details such as the nozzle, variable spacing cathode mechanism, and electrical connections have been omitted in this figure.

The anode and igniter are separated with a 2 mm thick insulator. The cylindrical igniter has the advantage of creating a more uniformly distributed spark around the cathode region, when compared to the conventional wire. As a result, the breakdown of air is also more uniform.

The AB-PPT with the addition of the variable spacing cathode mechanism was tested using the pendulum-based thrust stand. Figure 3.15 shows the relation between the cathode diameter, and the background air pressure at which breakdown of air first occurs, and Figure 3.16 shows the specific thrust measurements versus the background air pressure. The experiment was performed using three different voltage sources, 1000, 1200, and 1500 Volts, at five different cathode diameters, 28, 37, 51.5, 62, and 73 mm.

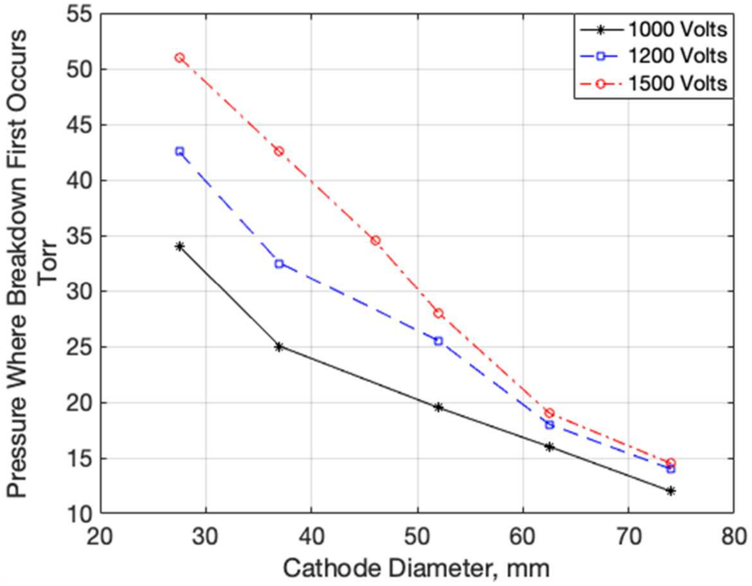

Figure 3.15: Cathode diameter of the first iteration of the AB-PPT with the addition of the variable spacing cathode mechanism versus the highest background air pressure at which breakdown first occurs. The experiment was performed using three different voltage sources, 1000, 1200, and 1500 Volts, at five different cathode diameters, 28, 37, 51.5, 62, and 73 mm for the 1000 and 1200 Volts, and six different cathode diameters for the 1500 Volts case.

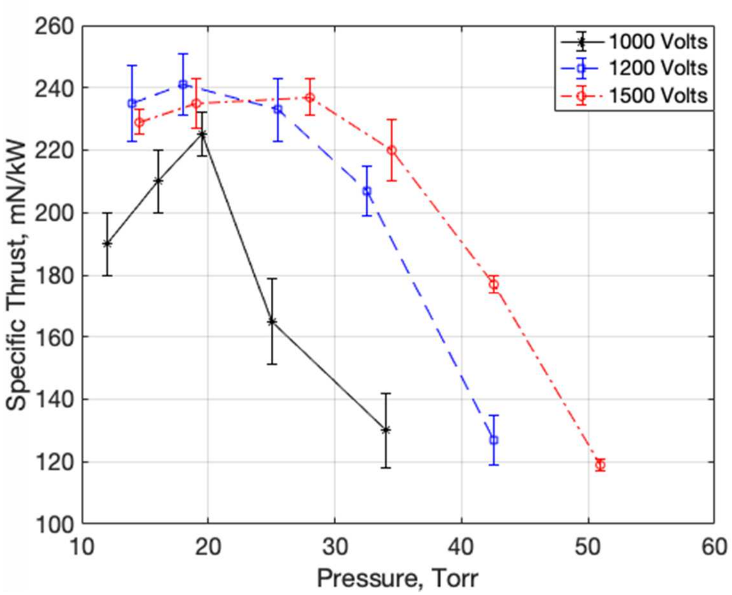

Figure 3.16: Specific thrust versus background pressure of the first iteration of the AB-PPT with the addition of the variable spacing cathode mechanism. The experiment was performed using three different voltage sources, 1000, 1200, and 1500 Volts, at five different cathode diameters, 28, 37, 51.5, 62, and 73 mm. Maximum specific thrust values of 240 mN/kW were achieved, with 1200 Volts at a background pressure of 19 Torr, and with 1500 Volts at a background pressure of 28 Torr.

According to different studies of the Paschen curve, such as the one described by E. Husain et al. [19], the relation between the breakdown voltage and the background gas pressure is not linear, in particular at low pressures. In other words, according to the Paschen curve, when approaching low background gas pressures, the required breakdown voltage remains relatively constant for a given pressure range. This situation is in accordance with the results obtained from the AB-PPT, as shown in Figure 3.15, where at background air pressures lower than 20 Torr, the required breakdown voltage does not vary significantly for a given cathode diameter.

Maximum specific thrust values of 235-240 mN/kW, for the 1.5 and 1.2 kV cases were obtained. Also, it is noticed that the peak values of both traces do not vary significantly. However, at higher voltage sources the peak values of specific thrust shift towards regions of higher pressure. The 1.2 kV trace shows an optimal performance in the 15-25 Torr range, whereas the 1.5 kV trace an optimal performance in the 20-30 Torr range. Finally, the maximum specific thrust value obtained when using a voltage source of 1 kV, is 225 mN/kW. This maximum value occurred at a background air pressure of 20 Torr. The range of operation in this case was also more limited when compared to the 1.2 and 1.5 kV cases.

The AB-PPT with the innovation of the variable spacing cathode mechanism was a significant improvement from the early designs. It allowed us to have more control and a more consistent thrust performance over a wider pressure range. However, this modification also resulted in maximum specific thrust values of 240 mN/kW – approximately half of the amount of specific thrust obtained with the daisy-shaped cathode AB-PPT. This reduction in specific thrust can be attributed to three conditions,

1) The change in the configuration of the cathode, from daisy-shaped to the sliding horizontal rods. This change resulted in a reduction in the main discharge surface area, i.e. with the daisy-shaped cathode the discharge would occur across the full length of the cathode, whereas for the horizontal rods, the discharge occurs in one single point, leading to less ionization of the background air.
2) Because no wall was added between the cathode rods; as the rods slide in, such that the diameter of the cathode decreases, some of the plasma diffuses in the radial direction through the gaps between the rods. This situation causes an increase in the ion-neutral

collisions in the radial direction, and a reduction of such collisions in the axial direction, leading to a reduction in the net thrust.

3) The location of the igniter, which was placed near the anode, as opposed to placing it near the cathode. While this configuration helped in creating a more uniform spark, as it will be shown and described in the following section, having the igniter near the anode is not as efficient, in terms of helping and reducing the breakdown voltage requirements. As a result, a lower background gas pressure is needed for a given cathode diameter, and thus reducing the amount of specific thrust.

3.3 SECOND ITERATION OF THE AB-PPT, WITH THE ADDITION OF THE VARIABLE SPACING CATHODE MECHANISM

Figure 3.17 shows the second and final iteration of the AB-PPT with the addition of the variable spacing cathode mechanism. This concept was published in 2019 at the AIAA Joint Propulsion Conference [21], and has a provisional patent – 16/506804. It has a total length of 250 mm, with a body diameter of 80 mm. The system is similar to the first iteration of the AB-PPT with the addition of the variable spacing cathode mechanism. However, this iteration has different improvements in four key elements:

1. Electrodes configuration.
2. The variable spacing cathode mechanism.
3. Air intake system.
4. Ignition system.

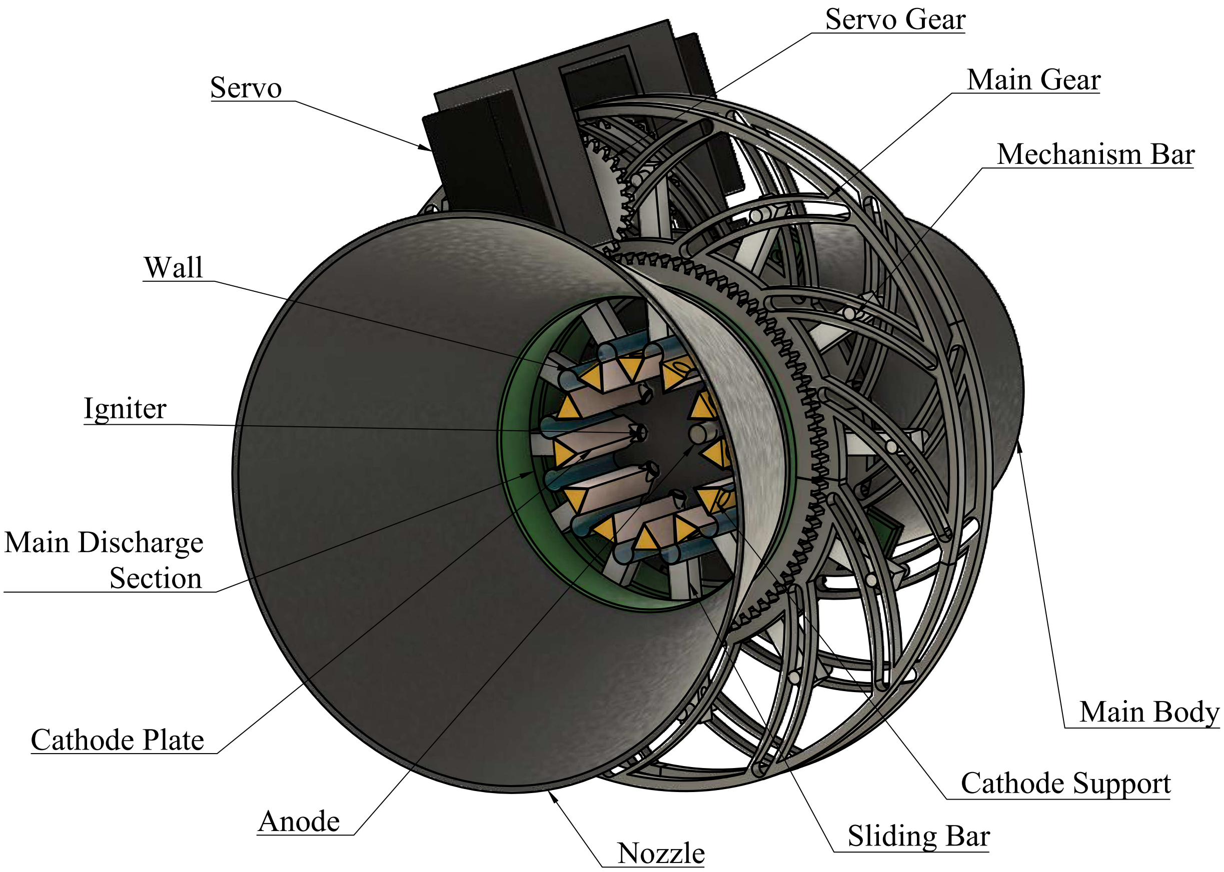

Figure 3.17: Second iteration of the AB-PPT with the addition of the variable spacing cathode mechanism.

Similar to the first iteration, the cathode consists of 12 bars evenly distributed around the circumference of the discharge section. However, with the intention of increasing the main discharge surface area of the cathode, the bars were designed with the same length as the discharge section, and parallel to the anode. In order to maintain the advantage that sharp electrodes possess in the enhancement of the electric field, the 12 bars were designed in a triangular shape. Additionally, in order to reduce the diffusion of the plasma and hot gases in the radial direction after the main discharge occurs, a flexible wall between the cathode bars was placed. A comparison of the two cathode configurations is shown in Figure 3.18.

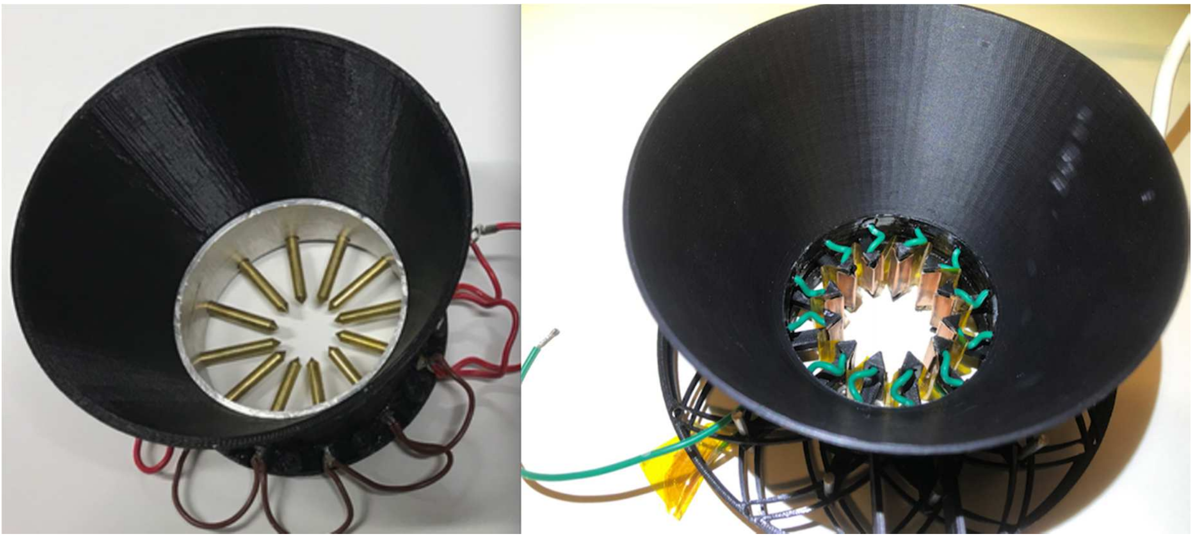

Figure 3.18: Cathode configurations of the first and second iteration of the AB-PPT with the addition of the variable spacing cathode mechanism.

The variable spacing cathode mechanism consists of 12 bars connected to the triangular-shaped cathode bars. Similar to the first iteration, the bars slide in and out in a circular pattern (typically in a 28-73.2 mm diameter range), and the diameter chosen is based on the background atmospheric pressure. Figure 3.19 shows a top view of the second iteration of the AB-PPT with the addition of the variable spacing cathode mechanism, at three different cathode diameters, 26.8, 40.8, and 52.4 mm. In order to move the bars, two large concentric gears surrounding the AB-PPT are used. The gears move, one of them clockwise and the other one anticlockwise, using two servo motors, which are connected to a pressure sensor. When the background gas pressure is in the desired range the servos start operating. In order to obtain a smooth, and almost frictionless movement of the large gears, metal bearings are used between the discharge section and the two concentric gears, as shown in Figure 3.20. The main discharge section is 35 mm in length, with 12 squared holes, evenly distributed around the discharge section for the cathode bars access. Additionally, the cathode bars were connected to each other in series with copper wire.

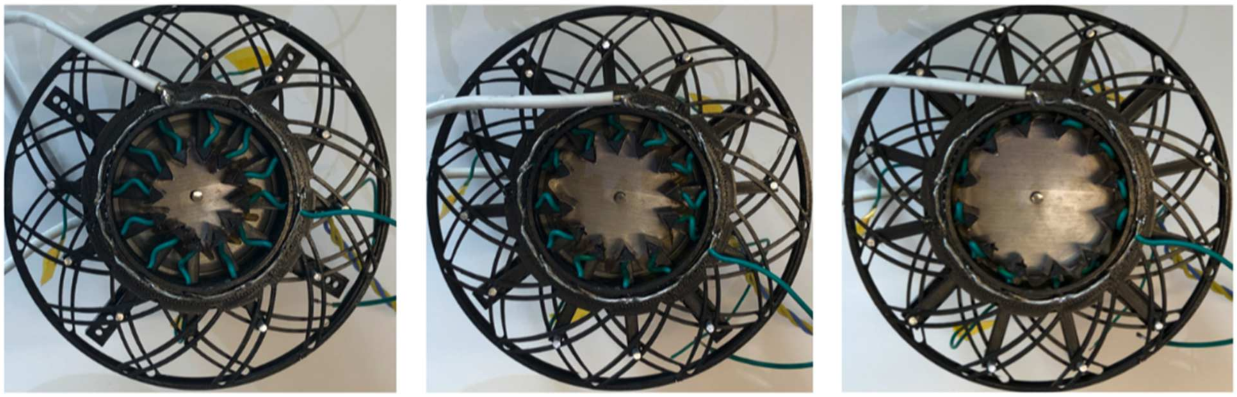

Figure 3.19: Top view of the second iteration of the AB-PPT with the addition of the variable spacing cathode mechanism, at three different cathode diameters, 26.8, 40.8, and 52.4 mm. The nozzle is not shown in this figure.

The air-intake system is similar to the system used in previous configurations. However, in order to direct the airflow into the discharge section more efficiently, while the device is in motion, a chamfer was added to the system, Figure 3.20.

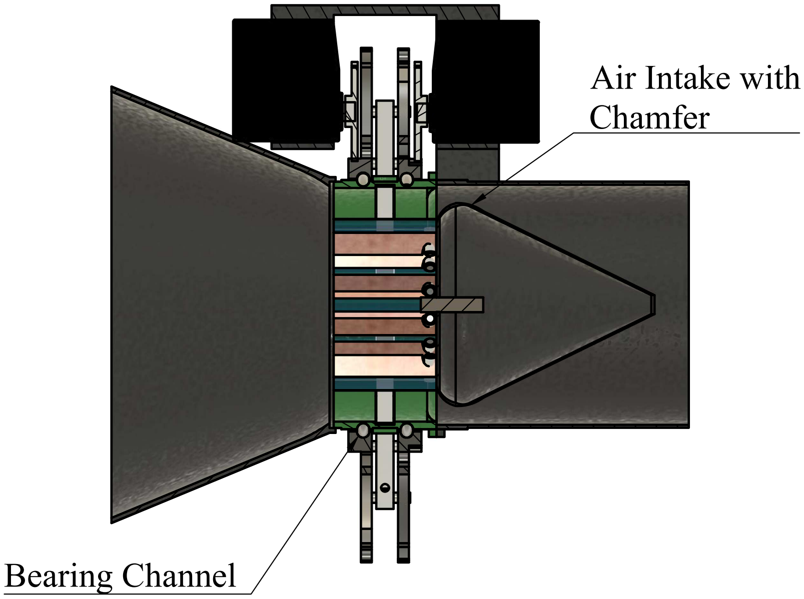

Figure 3.20: Cross section view of the second iteration of the AB-PPT with the addition of the variable spacing cathode mechanism. Details such as the channel for the main gear bearings, and the chamfer addition to the air intake are shown. Electrical connections are not shown in this diagram.

The main breakdown of air is initiated between the anode and one of the twelve cathode plates, and eventually the plasma fills up the whole discharge section of the AB-PPT. If the breakdown of air occurs in one of the plates at all time during operation, that particular plate will wear off relatively fast, limiting the lifetime of the AB-PPT. However, since the main breakdown of air occurs where the igniter is located, the origin of the breakdown can be controlled. This situation was solved in the first iteration by placing the igniter spark around the anode. However, because the cathode is where the electrons originate, it is more advantageous to place the igniter near the cathode, which would help in the breakdown of air at a higher background gas pressure. Therefore, for this iteration, 12 igniters were used - each of them was placed near one of the cathode bars, as shown in Figure 3.21.

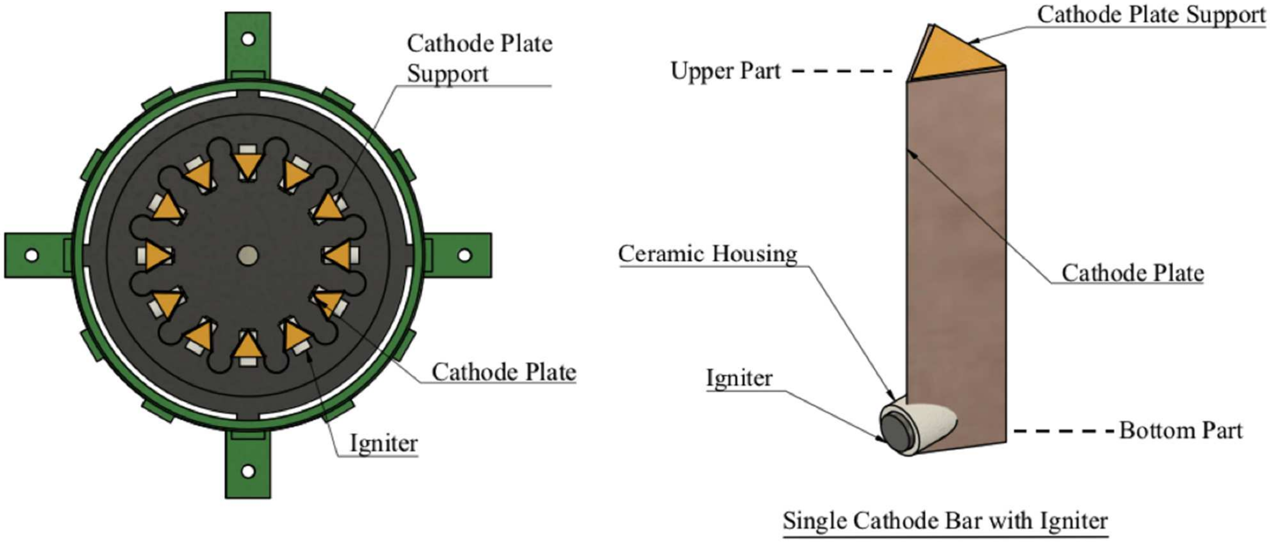

Single Cathode Bar with Igniter

Figure 3.21: Igniter configuration for the second iteration of the AB-PPT with the addition of the variable spacing cathode mechanism.

Additionally, a specifically designed igniter selector was used, Figure 3.22. It consists of a wheel (multiple spark selector) with 12 copper plates separated by 1.5 mm, and each of the plates is connected to one of the igniters. The wheel is attached to a servomotor, which is controlled using a microcontroller, and synchronized with the main discharge switching. In order to create a good electrical connection, the copper rod, which is connected to the output of the step-up toroidal transformer, is pushed at all times towards the multiple spark selector using a spring.

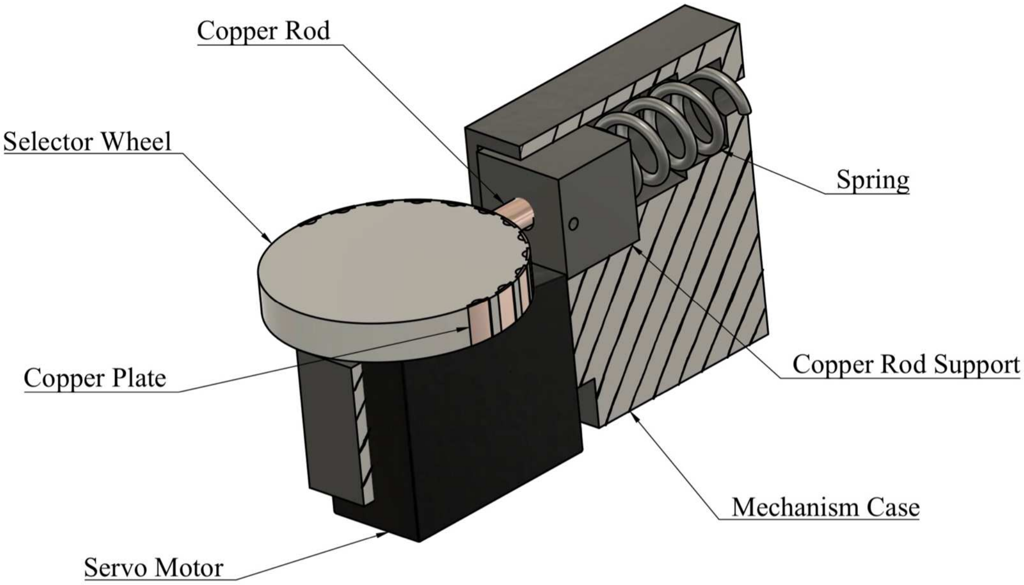

Figure 3.22: Igniter mechanism for the second iteration of the AB-PPT with the addition of the variable spacing cathode mechanism.

The second iteration of the AB-PPT with the addition of the variable spacing cathode mechanism was tested using the pendulum-based thrust stand. Figure 3.23 shows the relation between the cathode diameter, and the highest background air pressure at which breakdown of air first occurs (for both of the AB-PPT configurations: second iteration, using the multiple igniter configuration, and the first iteration, using the cylindrical igniter configuration), and Figure 3.24 shows the specific thrust measurements versus the background air pressure. The experiment was performed using 800 Volts per discharge, at five different cathode diameters, 26.8, 34, 40.8, 45.5, and 52.4 mm.

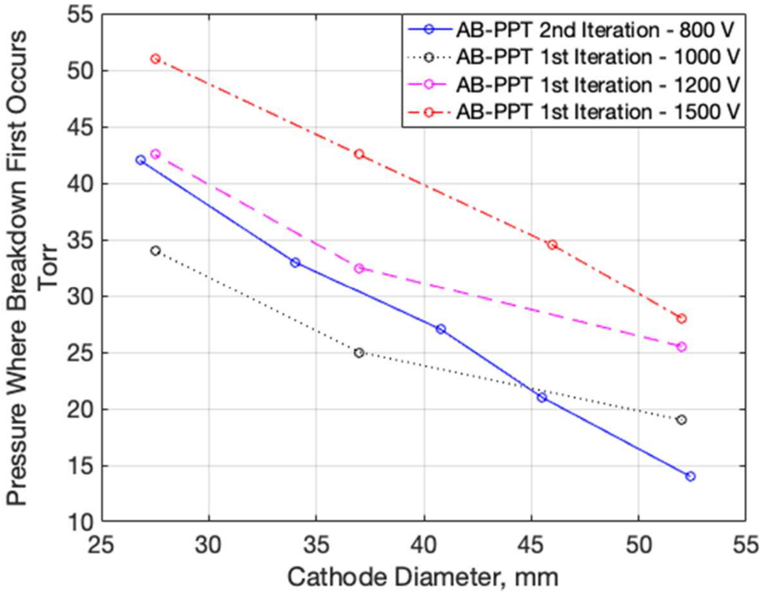

Figure 3.23: Cathode diameter of the AB-PPT versus the highest background pressure at which breakdown of air first occurs. The experiment was performed using a voltage source of 800 Volts, and five different cathode diameters, 26.8, 34, 40.8, 45.5, and 52.4 mm. For comparison, the three non-continuous lines show the cathode diameter versus the background pressure using 1000, 1200, and 1500 Volts, of the first iteration of the AB-PPT with the addition of the variable spacing cathode mechanism.

When compared to the configuration of the igniter near the anode, placing the igniter near the cathode helps in reducing the required amount of voltage per discharge. For a given cathode diameter and background gas pressure, the required voltage per discharge for the first iteration of the AB-PPT is approximately 50% more than the voltage needed for the second iteration. In addition to the non-linear behavior of the breakdown voltage and background gas pressure relation, described in section 3.2.2, it is believed that at low background gas pressures, the required breakdown voltage becomes more sensitive to the configuration and the geometry of the system.

In other words, it is believed that because a different configuration was used for the second iteration of the AB-PPT, a slightly different pattern at lower background gas pressures was derived.

Figure 3.24 shows the specific thrust values versus the background gas pressure, measured with the pendulum-base thrust stand. The blue continuous line represents the values obtained with the second (latest) iteration of the AB-PPT with the addition of the variable spacing cathode mechanism, whereas the three non-continuous lines represent the specific thrust values obtained with the first iteration of the AB-PPT with the addition of the variable spacing cathode mechanism.

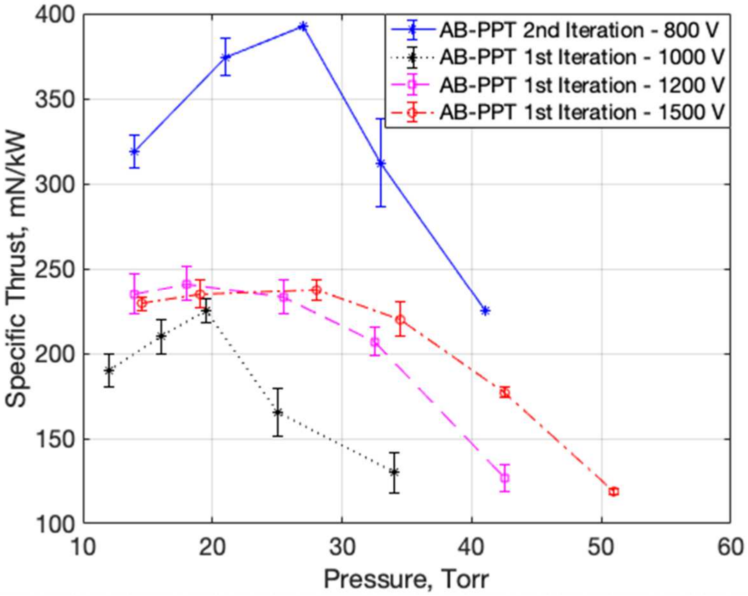

Figure 3.24: Specific thrust versus background gas pressure of the second iteration of the AB-PPT with the addition of the variable spacing cathode mechanism (continuous line). The test was performed using a voltage source of 800 Volts, and five different cathode diameters, 26.8, 34, 40.8, 45.5, and 52.4 mm. A maximum specific thrust value of 395 mN/kW was achieved, and at the intended range of operation, specific thrust values of > 350 mN/kW can be sustained. For comparison, the three non-continuous lines show the specific thrust values obtained using the first iteration of the AB-PPT with the addition of the variable spacing cathode mechanism, using 1000, 1200, and 1500 Volts.

Maximum specific thrust values of 395 mN/kW were obtained at a background gas pressure of 27 Torr, and specific thrust values of > 350 mN/kW can be sustained in the 17-30 Torr range, corresponding to a terrestrial atmospheric altitude of 20-30 km approximately. When compared to the thrust values obtained with the first iteration, an increase of approximately 60% was achieved. In order to have an optimal performance in a different pressure range, different voltage levels can be used, however in this study, further experimental testing was carried out using 800 Volts per discharge.

In order to reduce the manufacturability challenges in the construction and development of the different prototypes of the AB-PPT tested in this section, most of the components were made of 3-D printed ABS and PLA, whereas the cathode and the anode were made of copper and tungsten respectively, and the igniters were made of tungsten. A flight version would have to replace these 3-D printed components with more robust materials, but for short-term usage the 3-D printed components were more than sufficient for proof-of-concept and further experimentation.

Chapter 4. AB-PPT PLASMA CHARACTERISTICS

To this point, the different iterations of the AB-PPT have been studied based on the specific thrust measurements using the pendulum-based thrust stand, Figure 3.1. However, in order to have a better understanding of the acceleration mechanism of the device, further experimental testing was performed to quantify the characteristics of the generated plasma. Equation (2.8) indicates that the specific thrust can be divided into three different acceleration mechanisms; electromagnetic, electrostatic, and due to ion-neutral collisions. Such mechanisms are dependent on the measurable plasma parameters, ion density (n_i), ion speed (u_i), magnetic field (B), and plasma pressure (P). Therefore, in order to measure such parameters, two diagnostic techniques were used:

1. A quadruple Langmuir probe to measure the ion density, ion speed, and plasma temperature.
2. B-dot probe to measure the magnetic field.

In this section, we will start by describing the experimental setup, including the power supply, followed by a detailed description of each of the different plasma diagnostic techniques and the results.

4.1 EXPERIMENT SETUP

The measurements were performed using the bell-jar shaped vacuum chamber, and the AB-PPT was mounted on the pendulum-based thrust stand. However, because in this section no measurements of the specific thrust are presented, the pendulum was not included. A typical experimental setup is shown in Figure 4.1.

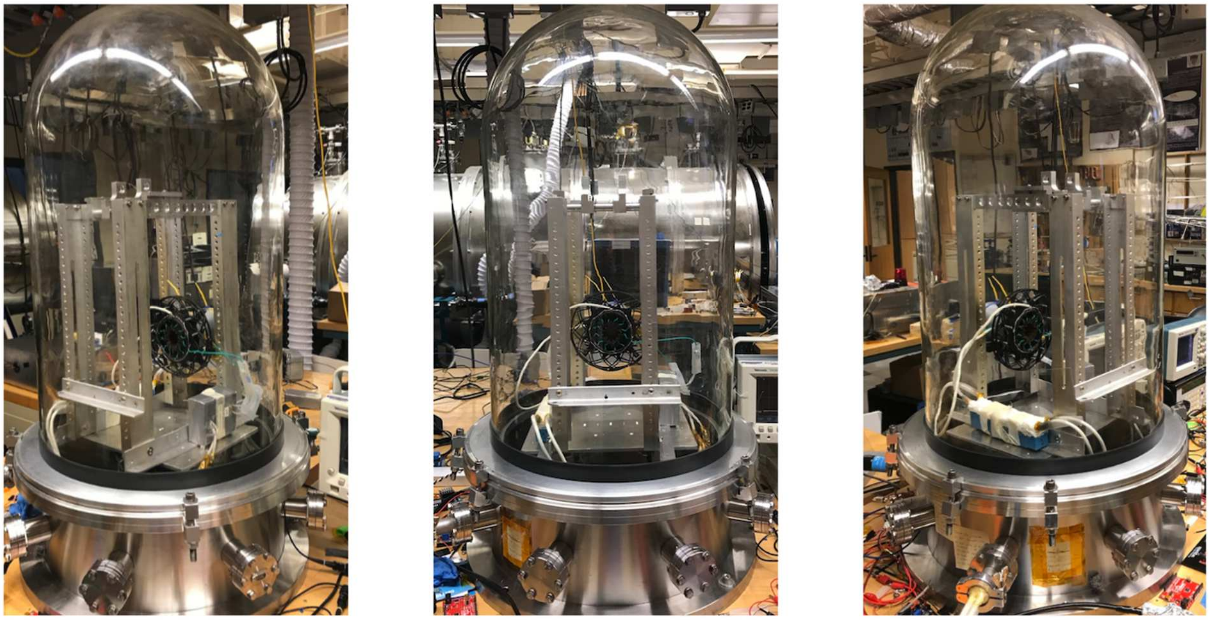

Figure 4.1: Typical experimental setup of the AB-PPT for the measurements of the different plasma parameters.

For the measurements of the plasma parameters presented in this section, the configuration that resulted in the maximum values of specific thrust was used. One of those configurations is the second iteration of the AB-PPT with the addition of the variable spacing cathode mechanism. Such configuration yielded a maximum specific thrust of 395 mN/kW, obtained at a background air pressure of 27 Torr, and a cathode diameter of 40.8 mm. Thus, the experiment and measurements in this section were performed using this configuration, with these parameters.

Additionally, the power supply was similar to the one used for the specific thrust measurements. The voltage source per discharge was 800 Volts, using a capacitor bank of 40 μF, resulting in a total energy per discharge of 12.8 Joules. Figure 4.2 shows a typical voltage and current trace of the AB-PPT main discharge. The traces are damped sinusoidal waves, with a pulse length extending to approximately 80 μs, whereas a maximum current of 4.6 kA was achieved.

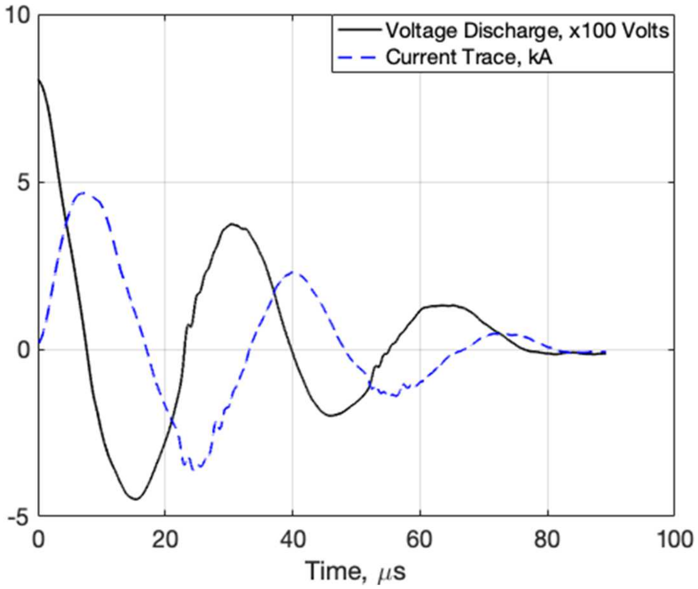

Figure 4.2: Voltage and current traces of the AB-PPT main discharge, using 800 Volts per discharge, with a capacitor bank of 40 μF.

4.2 LANGMUIR PROBE

In order to measure the ion density, ion speed, and plasma temperature, a quadruple Langmuir probe was used. The technique was developed by Burton, et al. in 1993 [22], and has been used for multiple in-space PPT experiments. The probe, shown in Figure 4.3, consists of four-2.3 mm in length, and 0.3 mm diameter tungsten bars. Probes 1, 2 and 3 were parallel to the plasma flow, and probe 4 perpendicular to it. Misalignments between probe 4 and the plasma flow were neglected, and the separation d, between the probes was 2 mm, such that the condition $d/\lambda_D \gg 1$, where λ_D is the Debye length, is satisfied. Additionally, the mean free path $\left(\lambda_{\text{mfp}}\right)$ was estimated to be 66 times the Debye length.

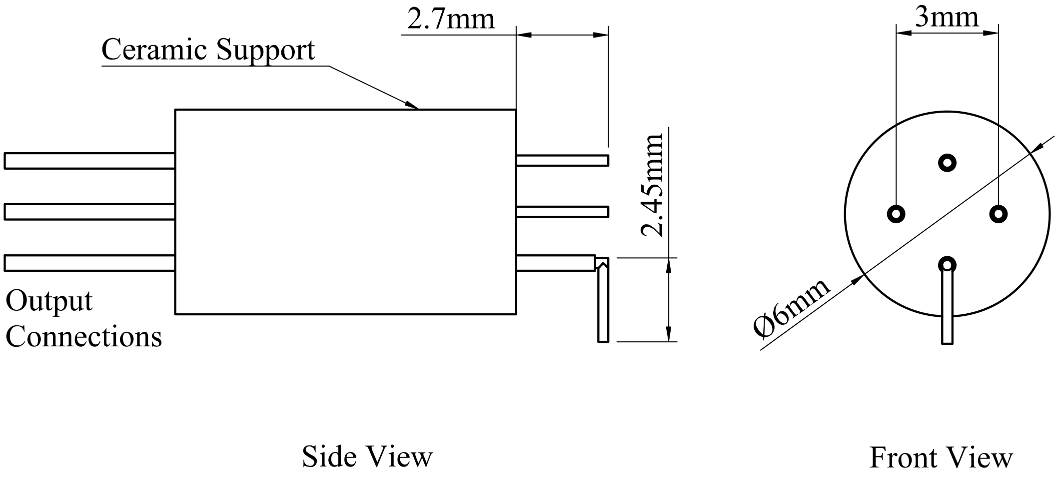

Figure 4.3: Side view and front view drawings of the quadruple Langmuir probe used to measure the ion density, plasma temperature, and ion speed of the AB-PPT.

Equation (2.8) requires measurements of the different plasma parameters at the point where the main discharge occurs, i.e. at point 1 of Figure 2.2. However, placing the probe near the plane where the main discharge between the anode and the cathode of the AB-PPT occurs, would result in undesirable arcs between one of the AB-PPT electrodes and the probe. Thus, the probe was mounted on a 3D printed support, which was then placed on the AB-PPT at $z = 30$ mm; $z = 0$ being the plane where the main discharge occurs. A 3D model of the AB-PPT with the Langmuir probe and support is shown in Figure 4.4.

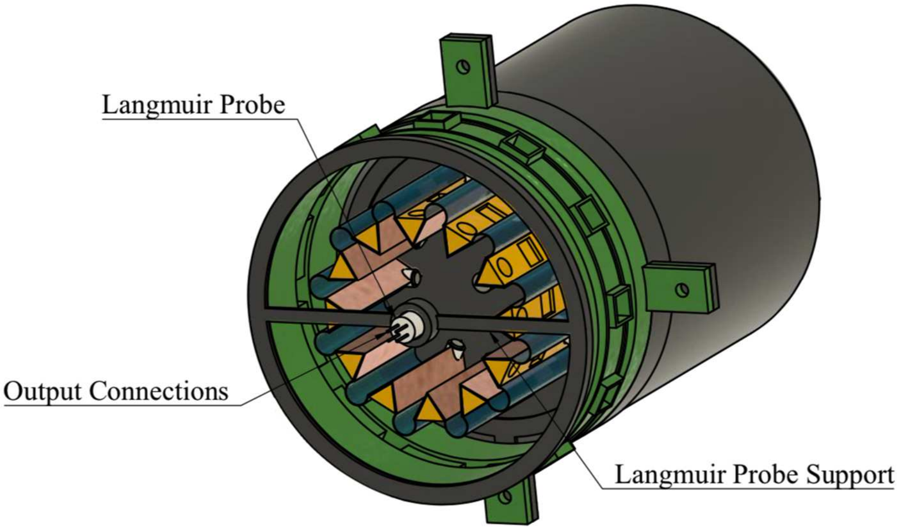

Figure 4.4: Setup of the quadruple Langmuir probe on the AB-PPT. In order to place the probe, the nozzle was substituted for the Langmuir probe support.

Figure 4.5 shows the electric diagram of the Langmuir probe. Probes P3 and P4 were negatively biased at 36 Volts negative with respect to P2 for ion current collection, and P1 was floating. The biased voltage is represented by V_s, whereas the measured voltage is represented by V_m. Currents I_3 and I_4 were measured using shunt resistors, R_s.

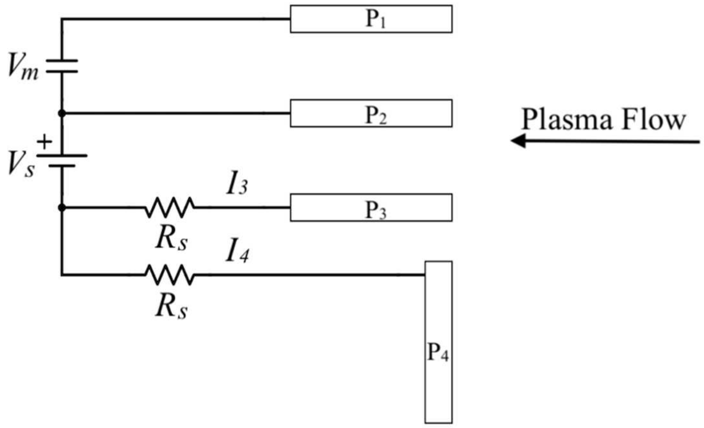

Figure 4.5: Quadruple Langmuir probe electric diagram. Probes 1, 2, and 3 are parallel to the plasma flow, and probe 4 perpendicular to it. V_s represents the voltage source, V_m the voltage to measure, and R_s are the shunt resistors used to measure the collected current by probes 3 and 4, i.e. I_3 and I_4.

The expressions to obtain the different plasma parameters can be derived by applying Kirchhoff's law to the electric diagram of the Langmuir probe, i.e.

$$I_2 = I_3 + I_4 \tag{4.1}$$

$$I_1 = 0 \tag{4.2}$$

$$V_{12} = V_1 - V_2 \tag{4.3}$$

$$V_{23} = V_{24} = V_3 - V_2 = V_4 - V_2 \tag{4.4}$$

using the definition of the current collected by an electrically charged probe,

$$I = -en_0 A \sqrt{\frac{kT_e}{2\pi m_e}} e^{-\frac{e|\emptyset(x)|}{kT_e}} + n_0 u_i e A \tag{4.5}$$

and assuming that the current collection area of probes P1, P2 and P3 are the same, i.e.

$$A_1 = A_2 = A_3 \tag{4.6}$$

The theory behind the quadruple Langmuir probe has been previously developed by different authors, and it is well documented [22]-[24]. Thus, it will not be discussed in detail. Combining equations (4.1)-(4.6), the equation to obtain the electron temperature can be derived, Equation (4.7).

$$\frac{\exp\left(\frac{e(V_s)}{kT_e}\right) + 1 - 2\exp\left(\frac{e(V_s - V_m)}{kT_e}\right)}{\left(\exp\left(\frac{e(V_s - V_m)}{kT_e}\right) - 1\right)\left(\frac{I_4}{I_3}\right)_{measured}} = 1 \tag{4.7}$$

This expression is a function of the measurable and known quantities, I_3, I_4, V_m and V_s, and the electron temperature is obtained through interpolation. Because 78% of Earth's atmosphere is comprised of nitrogen, it is assumed that the plasma is comprised mainly by ionized nitrogen. Thus, for a single ion species plasma, rearranging Equation (4.7) and using the Bohm sheath criterion, as described by Sekiguchi et al. [25], which relates the ion saturation current to the electron temperature, electron density and the ion mass, an expression for the electron density can be obtained.

$$n_e = \frac{\left(\frac{I_3}{A_3}\right)\left(1+\frac{I_4}{I_3}\right)\exp\left(\frac{1}{2}\right)}{\left(\exp\left(\frac{eV_m}{kT_e}\right)-1\right)e\left(\frac{kT_e}{m_i}\right)^{\frac{1}{2}}} \tag{4.8}$$

In order to determine the ion speed, the ratio of the current collected by the probe perpendicular to the flow to the probe parallel to the plasma probe must be taken, i.e. I_4/I_3. The current collected by a probe perpendicular to the plasma flow, and the cross electrostatic probes technique to measure the ion speed has been presented and studied elsewhere [26]. For a single species plasma this ratio is expressed as,

$$\frac{I_4}{I_3} = \frac{2}{\sqrt{\pi}}\frac{A_4}{A_3}k\exp\left[-\left(\frac{u_i}{c_m}\right)^2\right]\sum_{n=0}^{\infty}\left[\frac{\left(\frac{u_i}{c_m}\right)^n}{n!}\right]^2\Gamma\left(n+\frac{3}{2}\right) \tag{4.9}$$

where k represents the fraction of probe P4 that collects current, i.e. since the plasma flow induces a wake region through the probe perpendicular to the plasma flow, only a fraction of the area of the probe will collect current. It has been experimentally shown, that such value is approximately 1/2 for plasmas with $u_i/c_m \sim 1$ [27]. For the AB-PPT the ion speed is expected to be approximately similar to the most probable thermal speed, defined as $c_m = \sqrt{2kT/m_i}$, thus for this experiment, $k = 1/2$. Figure 4.6 shows the electron density, electron temperature, and speed ratio measurements as a function of time.

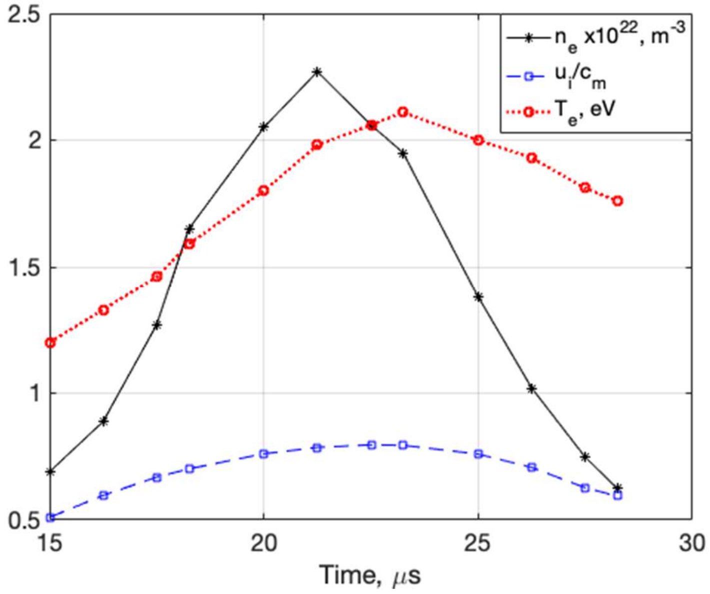

Figure 4.6: Electron density, electron temperature, and Mach number measurements of the AB-PPT at $z = 30\ mm$ along the axis.

Because the location of the probe was 30 mm away from the main discharge, the output signal was obtained 15 μs after the discharge, suggesting an exhaust velocity of approximately 2 km/s. The measurements were obtained over a time interval of 14 μs. Average values of $n_e = 1.38 \times 10^{22}\ \mathrm{m}^{-3}$, $T_e = 1.75\ e\mathrm{v}$, and $u_i/c_m = 0.7$ were obtained, with peak values at approximately 22-23 μs after the discharge. Recalling the definition of the most probable thermal speed, and using the average electron temperature, the resulting average ion speed is $u_i = 2266\ \mathrm{m/s}$, which is in close agreement with the velocity previously estimated. When compared to in-space PPTs, the AB-PPT's ion speed is much lower [15], suggesting that the thrust of the device is produced through a different mechanism, presumably through collisions between the charged particles and neutrals. This situation is in particular true when looking at the plasma density. Typical plasma density for an in-space PPT is on the order of ~ $10^{19}\mathrm{m}^{-3}$, whereas for the AB-PPT, assuming quasineutrality, $n_i = n_e = 1.38 \times 10^{22}\ \mathrm{m}^{-3}$. Finally, assuming thermal equilibrium, $T_i \cong T_e = 1.75\ e\mathrm{v}$. For in-space PPTs, the typical plasma temperature is on the order of 2 ~ 4 eV.

4.3 B-DOT PROBE

A single B-dot probe was used to measure the magnetic field in the theta direction. The probe consisted of a commercial inductor chip (LQW2UAS4R7J00L), placed on a 3D printed support designed to fit around the AB-PPTs anode, Figure 4.7.

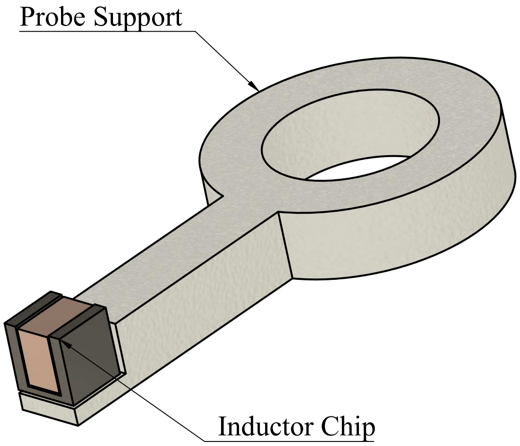

Figure 4.7: B-dot probe set up used to measure to magnetic field of the AB-PPT in the theta direction. The dimensions of the chip are $2.62 \times 2.45 \times 1.83$ mm, and it was mounted on a 3D printed support to fit around the anode 4.7 mm in diameter anode.

The dimensions of the chip are $2.62 \times 2.45 \times 1.83$ mm, with an inductance of 4700 nH. In order to reduce inductance coupling, the pair of wires connected to the chip were twisted, and in order to avoid capacitive coupling, the twisted wire was shielded and grounded, the output was then connected to an oscilloscope. Finally, the inductor chip was covered with epoxy to avoid undesirable arcs during breakdown. Figure 4.8 shows a simplified schematic diagram of the probe.

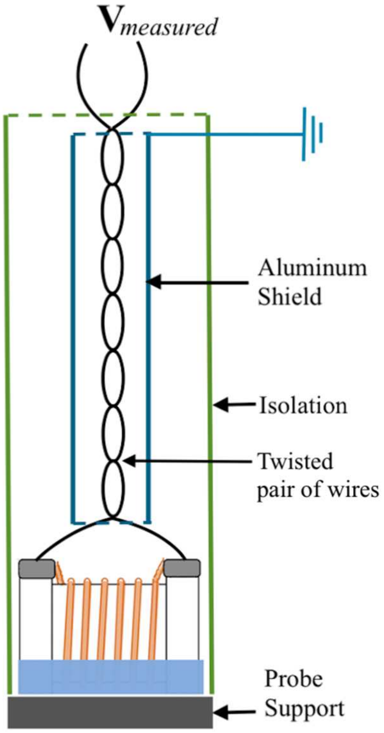

Figure 4.8: B-dot probe schematic diagram.

The magnetic field is measured through Faraday's law, $\Phi = \frac{\partial B}{\partial t} \cdot NA$, where NA represents the numbers of turns and the area of the inductor chip respectively. Thus, because the output signal is in the form of voltage, integration over the pulse length was performed in order to obtain the magnetic field. The B-dot probe was calibrated to obtain the effective NA using a custom designed Helmholtz coil. Because the magnetic field measurements in the AB-PPT were performed only in the theta direction, the calibration was only implemented in one direction, simplifying the process significantly. Additionally, because we are merely interested in the magnitude of the magnetic field, a calibration to determine the direction was not performed. A typical raw voltage signal from the Helmholtz coil and the B-dot probe is shown in Figure 4.9.

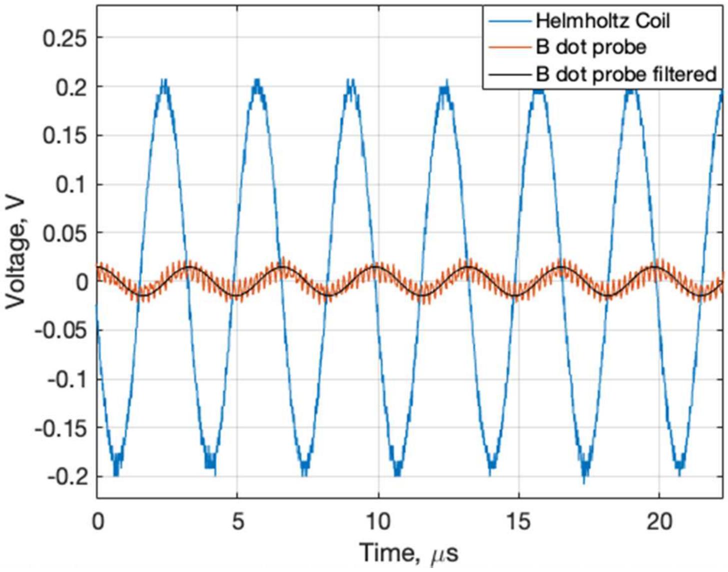

Figure 4.9: Typical raw voltage signal from the Helmholtz coil, and the B-dot probe (unfiltered and filtered).

The effective NA was then calculated by letting the magnetic field detected by the inductor chip equal to the Helmholtz coil magnetic field, i.e. $B = B_{HC}$. This equality can also be written as,

$$-\frac{1}{NA}\int \varepsilon_{coil}\, dt = \left(\frac{4}{5}\right)^{\frac{3}{2}} \frac{\mu_0 n I_{Hc}}{R} \tag{4.10}$$

where the left-hand side represents the magnetic field detected by the inductor chip, and the right-hand side the Helmholtz coil magnetic field - a well-known expression that can be found in different literature [28]. The current through the Helmholtz coil is represented by I_{Hc}, whereas n and R represent the number of turns and the radius respectively. The calibration process led to an effective NA value of 115 mm^2. Because equation (2.8) needs the magnetic field where the plasma discharge occurs, the probe was placed at an axial distance equivalent to the plane $z = 0$, between the anode and the cathode. Additionally, because the main discharge initiates at one of the cathode plates, measurements were performed at four different angles along the $z = 0$ plane: 0, 90, 180, and 270 degrees, as shown in Figure 4.10.

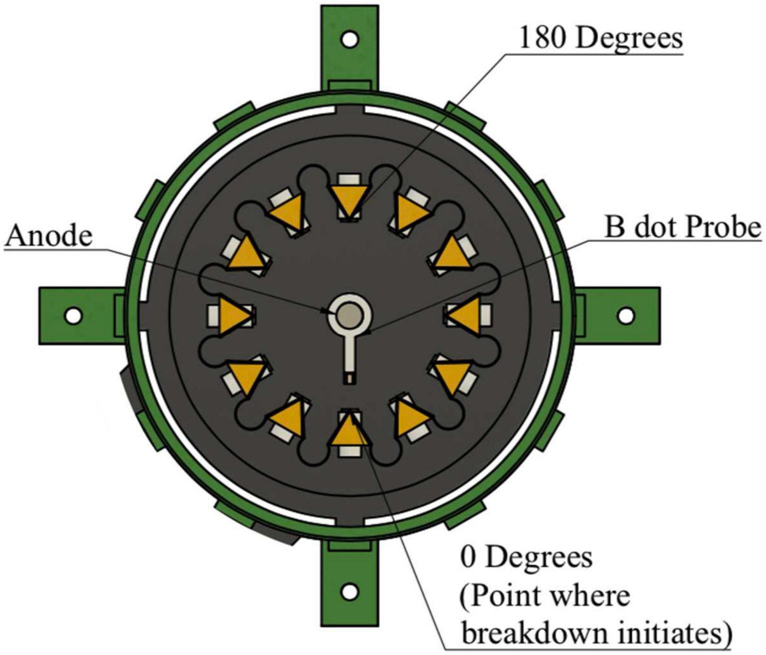

Figure 4.10: Top view of the AB-PPT showing the B-dot probe array. The probe was positioned at $z = 0$, at four different angular positions, 0, 90, 180, and 270 degrees. The zero degrees position represents the point where breakdown is initiated. Details such as the nozzle, the variable spacing mechanism and servo motors have been omitted in this figure.

Because the igniter spark selector (Figure 3.22) was used for the experiment, we were able to control the location of the main discharge. Therefore, the point where the breakdown occurs corresponds to 0 degrees, whereas the farthest point corresponds to 180 degrees. Five measurements per angular position were performed. Figure 4.11 shows an average of the magnetic field measurements per angular location.

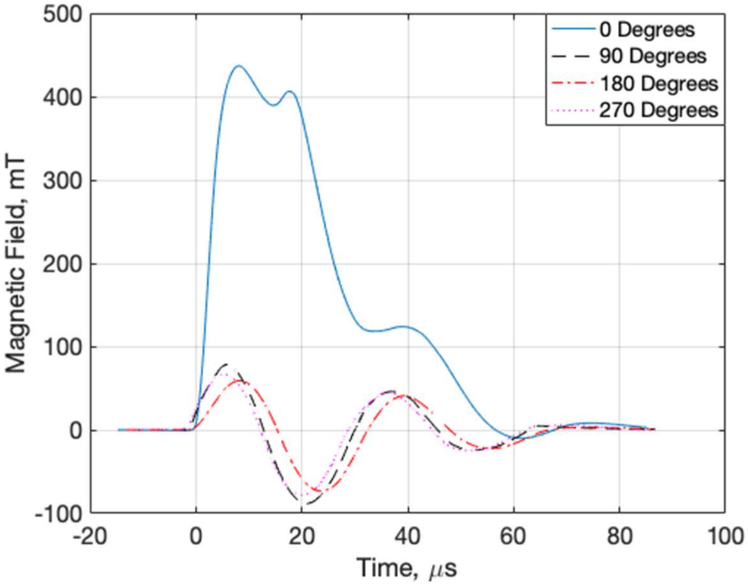

Figure 4.11: Magnetic field measurements, at $z = 0$, and different angular positions; 0, 90, 180, and 270 degrees.

Because the main discharge is initiated at the cathode bar where the igniter is located, an asymmetry in the discharge at the $z = 0$ plane is noticed. At the 0 degrees position, the magnetic field is the strongest, reaching more than 400 mT, for a time length of approximately 20 microseconds. The other three angular positions show a weaker magnetic field, with no more than 100 mT. No considerable differences between the 90, 180, and 270 degrees is noticed. This situation suggests that at the zero degrees angular position, a larger flow of electrons between the anode and the cathode occur, causing a higher percentage of ionization of the background air, and as the plasma expands across the entire AB-PPT discharge section, the ionization percentage is reduced. Therefore, due to asymmetries in the magnetic field measurements, in order to validate equation (2.8), an average of the magnetic field in the four different angular positions was used, as described in the following section.

4.4 RESULTS

In order to validate equation (2.8), averaged quantities of the different plasma parameters, measured over a pulsed length of 80 microseconds were used. I.e. $n_i = 1.38 \times 10^{22}$ m^{-3}, $u_i = 2266$ m/s, and $B = 100$ mT. In order to obtain the plasma pressure, the expression $P = (T_i + T_e)n$ was used, where $n = n_i = n_e$ and $T_e = T_i = T$, leading to a plasma pressure (P), of 7.12 kPa. In order to determine the pressure of the neutrals, we need to consider the degree of ionization, and how much of the plasma temperature has been transferred to the neutrals at the moment of ionization. Because the latter is almost impractical to determine, and because the degree of ionization $(\alpha = n_i/(n_i + n_n))$ is relatively small, P_n is assumed to be the background gas pressure, i.e. 27 Torr. However, this value could be approximately 5% lower. The energy per discharge was 12.8 J, and the radius of the cathode was the average between the peak of the cathode bar and the flexible wall, i.e. $r_2 = 30$ mm. Equation (2.8) leads to specific thrust values of 352 mN/kW, which shows good agreement with the 395 mN/kW of specific thrust, obtained using the pendulum-based thrust stand under the same experiment configuration. The discrepancies between the two methods can be attributed to uncertainties of the different measuring techniques, and asymmetries in the plasma discharge, which could have led to variations in the different measurements. This is in particular true for the Langmuir probe measurements. According to Bushman et al. [29], and similar experiments using the quadruple Langmuir probe technique [30], based on the combination of theoretical assumptions, and experimental uncertainties, a total uncertainty of 50, 14, and 15% for n_e, T_e and u_i/c_m respectively is estimated. Experimental uncertainties are in particular relevant for plasmas with a high ion speed, which causes the probe to be sensitive to small angle misalignments, placing additional uncertainties of 11% to the density measurements [31]. However, because the ion speeds obtained from the AB-PPT are relatively small, the uncertainties placed on n_e due to the misalignments of the probe are expected to be lower. Also, according to Sekiguchi et al. [25], the percentage error of n_e is lower than 15% for plasmas with $T_e < 6eV$. Thus, an uncertainty of approximately 20% for the electron density measurements is estimated. Finally, discrepancies can also be attributed to the pendulum-based thrust stand, where the calibration process placed an uncertainty of $\pm 10\%$. Based on the Langmuir probe and B-dot probe measurements, we are able to determine that the main acceleration mechanism is derived from the ion-neutrals collisions, with a contribution of 57% ± 7%, followed by the electromagnetic acceleration, contributing with 33% ± 5%, and the electrostatic acceleration, with 10% ± 4%.

4.5 AB-PPT VERSUS CONVENTIONAL PROPELLERS

One of the potential applications of the AB-PPT is to power an aircraft that could potentially act as an atmospheric satellite in the stratosphere, thus finding the atmospheric altitude at which the proposed device delivers greater specific thrust values than conventional blade-based propellers is necessary. The specific thrust as a function of the background air pressure of different blade-based propellers, including an in-house designed propeller for high-altitudes, was measured. The experiment was carried out in the bell-jar shaped vacuum chamber, using a commercial brushless motor – GoolRC A2212/5T, and a power source of 14-17 Watts. In order to measure the thrust, two scales were used: a commercial digital scale with an accuracy of ±0.01 grams, and an RC lander outer rotor motor thrust stand. Figure 4.12 shows the two thrust stands used for the experiment.

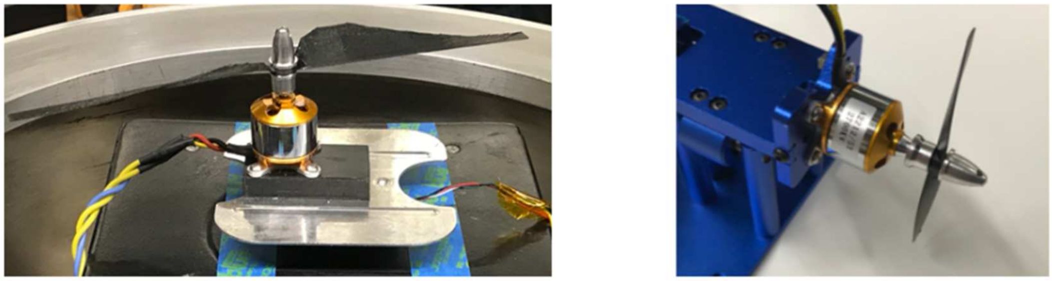

Figure 4.12: On the left, in-house designed propeller for high-altitudes, mounted on the commercial digital scale with an accuracy of ±0.01 grams. On the right, commercial 10-cm propeller, mounted on the RC lander outer rotor motor thrust stand.

Figure 4.13 shows typical specific thrust values as a function of altitude, obtained from one of the blade-based propellers with better performance at high atmospheric altitudes. These values show good agreement with other propellers of this type, such as the ones used in Zephyr from Airbus [2]. Because the AB-PPT can be configurable to deliver maximum specific thrust values at any given background pressure, the optimal point of operation would be determined by the point at which the blade-based propeller delivers lower values of specific thrust than the AB-PPT, in this case 500 mN/kW. Therefore, Figure 4.14 shows the specific thrust values of the blade-based propeller, and a vertical dotted line representing the maximum values of specific thrust experimentally obtained from the AB-PPT.

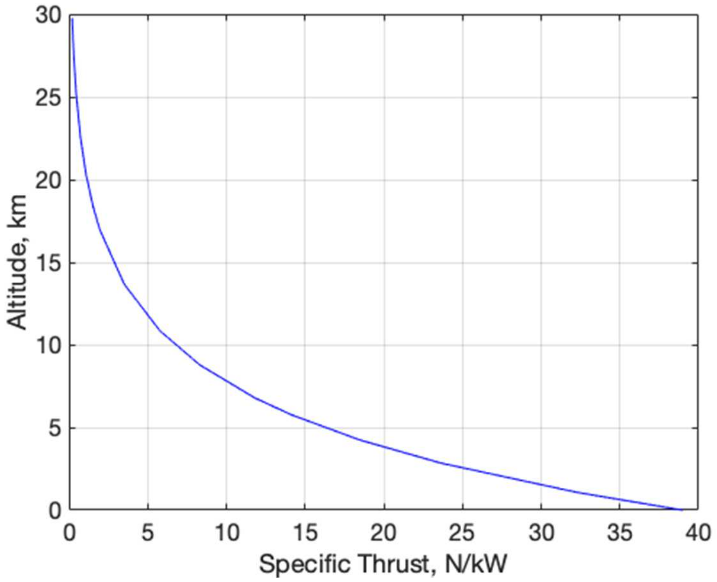

Figure 4.13: Specific thrust as a function of altitude of a conventional blade-based propeller.

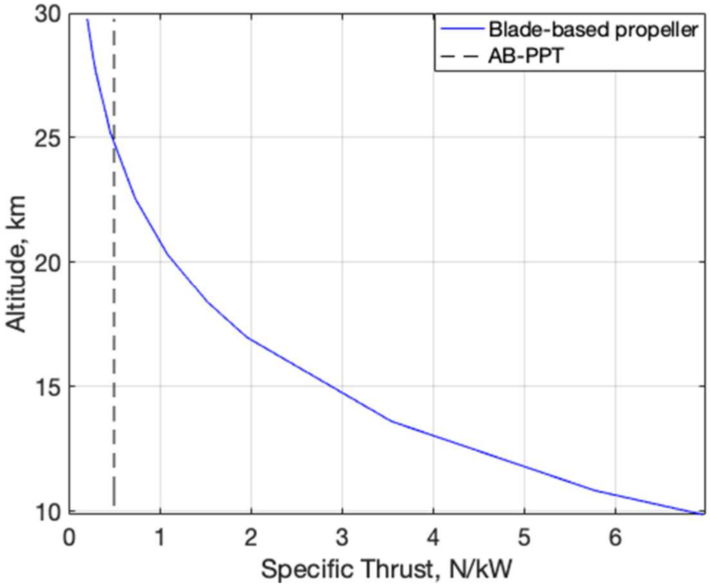

Figure 4.14: Specific thrust values as a function of altitude of the conventional blade-based propeller and the AB-PPT. The dotted black like represents the maximum values of specific thrust experimentally obtained at the APL.

At an atmospheric altitude of approximately 25 km, the AB-PPT outperforms the conventional blade-based propellers. Therefore, based on these results the ideal range of operation for the intended atmospheric satellite powered with the AB-PPT, would be above this region. Although blade-based propellers perform well at an atmospheric altitude of up to 25 km, as it will be discussed in section 5.1, in order to avoid the need of batteries for operation of the propulsion systems at night, and thus be able to reduce the total weight of the system, the sink rate of the aircraft can be used. However, to compensate using solely solar panels during daytime for the loss of altitude during night, operating at higher altitudes is required.

Because the net force of the blade-based propellers is proportional to the air density and exhaust speed, as shown in equation (1.1), in order to maintain the force and compensate for the lack of air at high altitudes, the exhaust speed must increase, increasing the RPMs of the propeller and imposing a potential risk of structural damage to the blades. This situation was observed when one of the propellers tested in the vacuum chamber shattered at a background air pressure of 35 Torr, corresponding to an atmospheric altitude of 20 km, as shown in Figure 4.15. Because the thrust measurements were performed relatively fast, no heating issues in the motor were observed. However, according to Craig L. Nickol et al. [4], over heating of the motor and other components can be an issue due to the low air density at high atmospheric altitudes, limiting the altitude at which blade-based propellers can operate.

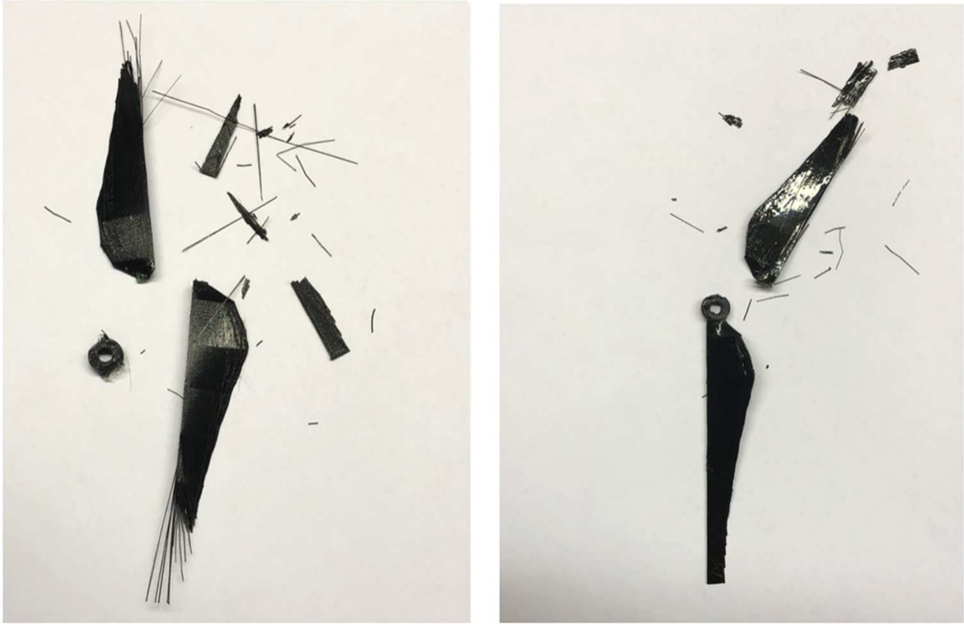

Figure 4.15: 3D printed blade-based propellers shattered while testing at a background air pressure of 35 Torr, corresponding to an atmospheric altitude of 20 km.

Chapter 5. PROPOSED AIRCRAFT

In this section, we will study the potential practical applications of the AB-PPT. Because the device was originally intended for powering an aircraft that could potentially act as an atmospheric satellite in thin atmosphere, this chapter will be mainly focused on the different design considerations for developing such an aircraft. Additionally, there are always differences and inherent unforeseen issues as a laboratory system is converted to a flight system. To account for such issues, three in-field tests were performed, where an in-house designed and constructed aircraft was launched into the stratosphere using high-altitude burst balloons to test the system. In this section, the different launches will be also discussed in detail.

5.1 AIRCRAFT DESIGN CONSIDERATIONS

Using specific thrust values of 500 mN/kW (maximum values of specific thrust experimentally obtained at the APL using the AB-PPT with the daisy-shaped cathode configuration), it is possible to propel an aircraft using the AB-PPT at terrestrial atmospheric altitudes > 20 km, and/or in an atmosphere of a different planet/moon, such as Mars and Titan. The analysis presented in this section is focused on terrestrial atmospheric applications. An initial analysis for an aircraft design can be derived from the following simplified expression,

$$F_{lift} = C_{LD} F_{thrust} \tag{5.1}$$

where F_{lift} represents the lift force created by the aircraft, C_{LD} the lift-to-drag coefficient of the wings, and F_{thrust} the net thrust produced by the propulsion system. For the AB-PPT, the net thrust can also be expressed as,

$$F_{thrust} = T_{sp} f E_c \alpha \tag{5.2}$$

where f and E_c are the frequency and energy per discharge respectively, and α the total number of AB-PPTs. A typical experimental energy and frequency per discharge of the system are 13 Joules and 20 Hz respectively. Therefore, for a specific thrust of 500 mN/kW, a net thrust of 0.13 N would be delivered. The actual performance will depend on the electronics, and power supply of the system.

In addition to equation (5.1), for sustained flight, the condition $mg < F_{lift}$, where m is the total mass of the aircraft and g the acceleration of gravity, must be satisfied. Therefore, equation (5.1) can be expressed as,

$$mg \leq C_{LD} T_{sp} f E_c \alpha \tag{5.3}$$

The lift-to-drag coefficient (C_{LD}) depends on the airfoil, angle of attack, and Reynolds number $R = \frac{vc}{u}$, where c is the chord length of the wings, u the kinematic viscosity, and v the flight speed. For an intended atmospheric satellite of this type, and for station keeping, the flight speed is on the order of 7-15 m/s. A typical lift-to-drag coefficient of an airfoil for a high-altitude aircraft, such as the E178, can vary between 40 to 120 at an angle of attack of 7 degrees, depending on the Reynolds number. Different tools and experimental data of the key parameters of different airfoils are readily available. Figure 5.1 shows the lift-to-drag coefficient as a function of the angle of attack of an airfoil E178, at different Reynolds numbers (figure obtained from "Airfoil Tools", UIUC Airfoil Coordinates Database [32]).

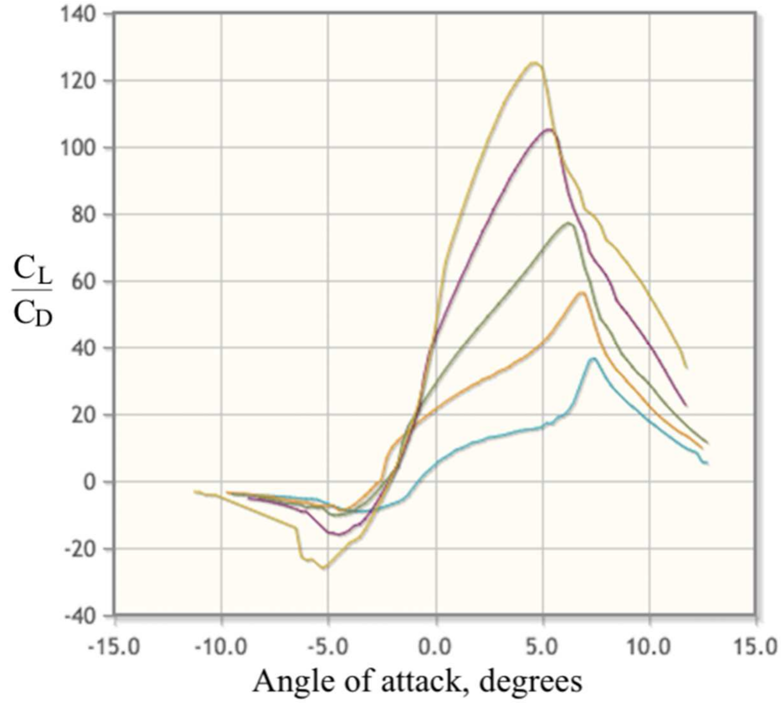

Figure 5.1: Lift-to-drag coefficient as a function of angle of attack of an airfoil E178 for different Reynolds numbers. The lower (blue) trace represents the coefficient at the lowest Reynolds number, with the maximum lift-to-drag coefficient resulting at an angle of attack of approximately 7.5 degrees. (Figure extracted from "Airfoil Tools", UIUC Airfoil Coordinates Database [32]).).

In order to minimize weight and complexity of the system, the aircraft would be launched to the stratosphere using high-altitude burst balloons, and in order for the system to stay in the prescribed area, the aircraft would fly during day using solar panels, at an atmospheric altitude of ~ 30 km, and during night it would glide down to an altitude of 20 km. The typical sink rate for an aircraft of this type is 0.4 m/s [33], thus in 10 hours the proposed system would sink less than 14 km overnight, and because the performance of the AB-PPT is relatively uniform over this range through the atmosphere, it allows the system to climb back at maximum altitude during day.

Because of this, although battery storage is desirable, no batteries to store the energy for operating the AB-PPTs at night are needed, reducing considerably the total weight of the system. Using specific thrust values of 500 mN/kW, a lift-to-drag coefficient of 40, and based on equation (5.1), a relation between the power requirements and the total mas of the aircraft can be interpolated, as shown in Figure 5.2.

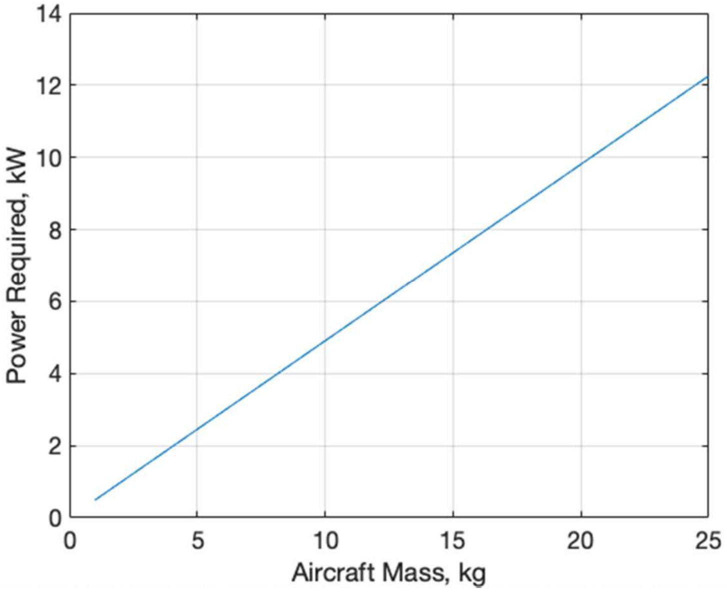

Figure 5.2: Power requirements as a function of total aircraft mass. Interpolation obtained using equation (5.1), based on specific thrust values of 500 mN/kW, and a lift-to-drag coefficient of 40.

Solar panels capable of delivering up to 2 kW/kg are commercially available (through companies such as Flisom). Thus, if specific thrust values of 500 mN/kW are used, the thrust-to-weight ratio would be 1 N/kg. However, this ratio does not include the weight of the AB-PPT, and the electronics to convert the energy collected by the solar panels into usable energy to ionize the background gases of the atmosphere.

Because the AB-PPT developed at the APL is a prototype mainly made of 3D printed materials, the exact weight of a final flight version is still unknown. However, opposite to conventional in-space EP devices, that need to have a lifetime of 5+ years, operating under harsh space conditions, the AB-PPT is designed to operate at a more accessible operation range, allowing to perform maintenance and/or repairs to the system as needed, thus the AB-PPT can be manufactured with very light materials. The heavy components being the electrodes, ceramic components, and electrical connections. The estimated weight of the commercial version of the AB-PPT is < 200 grams. Finally, if an electric system capable of delivering 4 kW/kg is used, the thrust-to-weight ratio of the AB-PPT plus the electronic system would be also 1 N/kg. An electric system capable of delivering such ratio can be achieved through various configurations, depending on the energy and frequency per discharge, as expressed in equation (5.2). A high-power electronic configuration is shown and discussed in more detail in Figure 5.3. With these parameters, the combination of the solar panels, AB-PPT, and electronic system would result in a thrust-to-weight ratio of 0.5 N/kg. If a lift-to-drag coefficient of 40 is used, half the weight of the aircraft would be allocated to the combination of the solar panels, AB-PPTs and electronics, whereas the other half would be allocated to the structure of the aircraft, and the mission's payload.

Depending on the mission requirements, there are multiple possible configurations for having a fully functional aircraft powered with the AB-PPT. The design of such an aircraft can be divided into four different subsystems:

1. Wings.
2. AB-PPT.
3. High-power electronics.
4. Solar panels.

Based on commercially available technology and using specific thrust values of 500 mN/kW, a possible configuration for a 20-kg aircraft is shown in the following diagram.

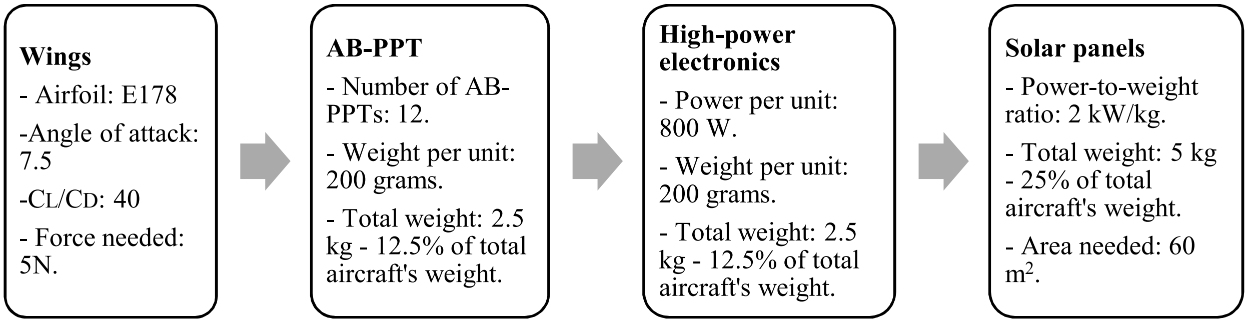

Figure 5.3: Possible configuration for a 20-kg aircraft, based on commercially available technology, and using specific thrust values of 500 mN/kW.

The lift-to-drag coefficient will dictate the required force to sustain an aircraft. Therefore, based on equation (5.1), if such coefficient is 40, for a 20-kg aircraft the required force would be 5 N. Currently, companies such as Flisom offer solar panels capable of delivering 2 kW/kg, thus for a specific thrust of 500 mN/kW, 5 kg of solar panels are needed. Finally, based on equation (5.2), 5 N of force can be achieved using 12 AB-PPTs, operated at 20 Hz, and 40 Joules per discharge, which can be obtained from an 80 μF capacitor bank, operated at 1000 Volts per discharge.

In order to estimate the maximum attenable aircraft speed, equation (5.1) can be written in terms of the lift and drag force,

$$F_{lift} = \frac{1}{2} C_L \rho v^2 A \tag{5.4}$$

$$F_{drag} = \frac{1}{2} C_D \rho v^2 A \tag{5.5}$$

where ρ, v, and A are the background air density, aircraft speed, and wings area respectively, and the lift and drag coefficients are given by C_L, and C_D respectively. Using the parameters from Figure 5.3, equations (5.2), (5.4), and (5.5) are plotted in Figure 5.4.

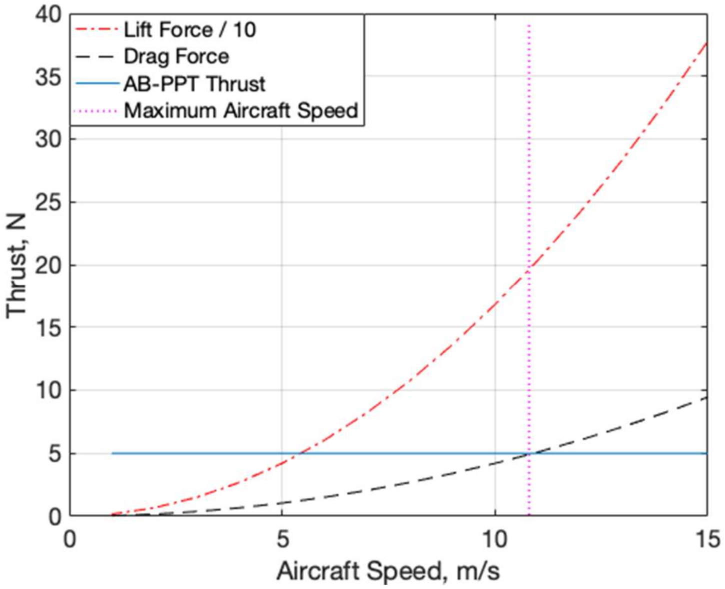

Figure 5.4: Lift force, drag force, and AB-PPT thrust as a function of aircraft speed. The data shown in this figure is based on the parameters shown in Figure 5.3. The maximum possible aircraft speed is determined by the drag force, emphasized with the dotted magenta line. At this point, approximately 11 m/s, the maximum lift force would be 200 N, i.e. approximately 20 kg.

The continuous blue trace represents the net thrust delivered by the AB-PPT, whereas the dotted black line represents the drag force. These two traces will determine the maximum speed that the aircraft can attain. In this scenario such speed will be approximately 11 m/s, as shown by the dotted magenta line. As discussed in more detail in section 5.2.1, the wind speed at an atmospheric altitude > 20 km is less than 5 m/s, meaning that for station keeping 11 m/s is more than enough. At this speed the corresponding lift force would be 200 N, i.e. a 20 kg aircraft could be sustained at an atmospheric altitude of approximately 30 km. With these parameters, a speed higher than 11 m/s is not possible, since the drag force becomes greater than the net force delivered by the AB-PPT. Figure 5.5 shows the proposed aircraft, with a 35 meter wingspan.

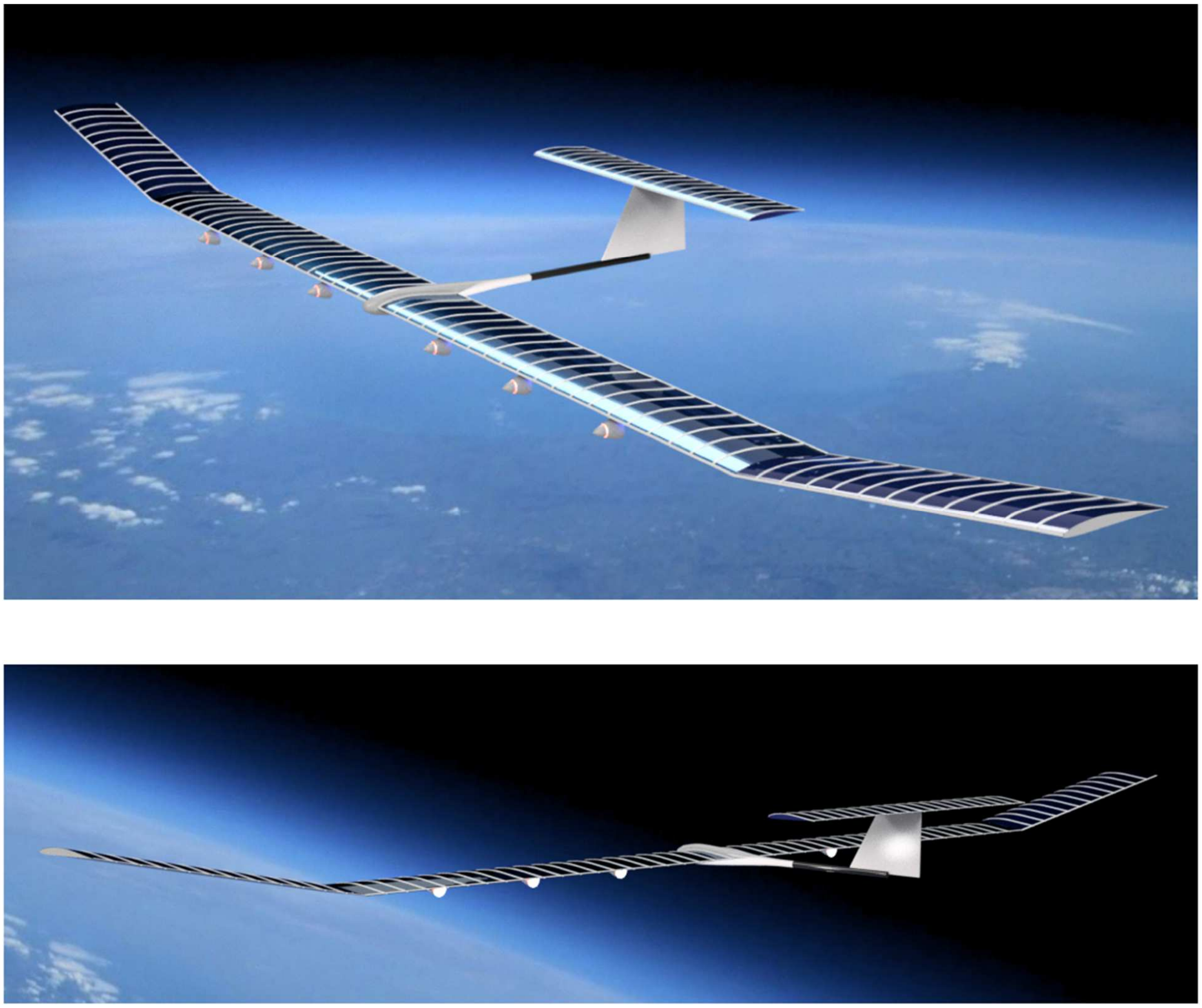

Figure 5.5: Proposed aircraft powered with the AB-PPT. The aircraft has a wingspan of 35 meters, and the AB-PPTs are placed underneath the wings.

5.2 PROOF OF CONCEPT

In order to test the system's ability to deliver the required thrust to sustain an aircraft at atmospheric altitudes > 20 km, five specifically designed aircrafts, ELEPHANT 1, 2A, 2B, 3A, and, 3B (Experimental Lift with Electric Propulsion at High Altitude Niche, Test 1, 2A, 2B, 3A, and 3B), were launched into the stratosphere using high-altitude burst balloons. Due to the FAA (Federal

Aviation Administration) regulations on flight of untethered balloons, the weight of the multiple aircraft was kept at < 5 kg. Figure 5.6 shows three of the different launches, ELEPHANT 1, 2A, and 2B.

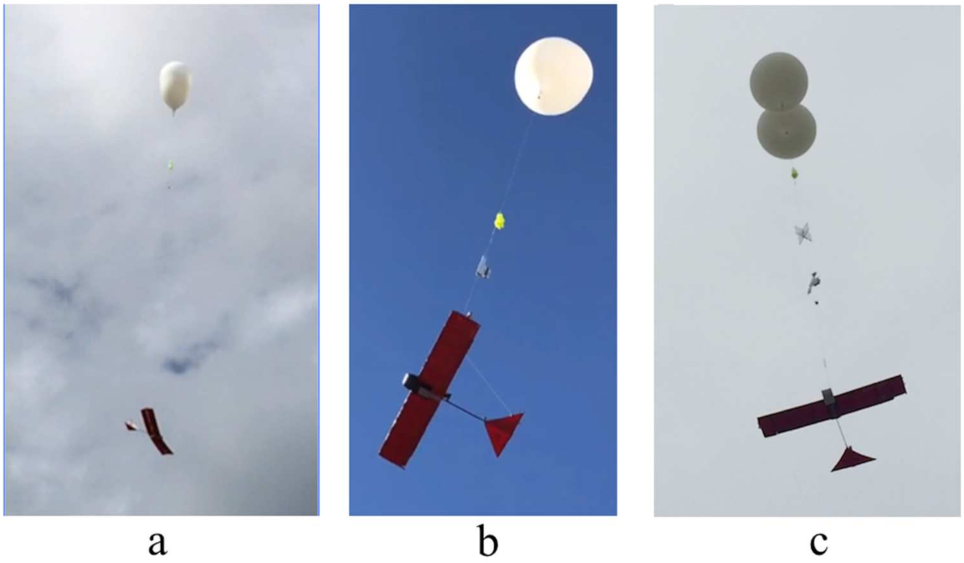

Figure 5.6: Three of the different in field launches using high altitude burst balloons. a) ELEPHANT 1, b) ELEPHANT 2A, and c) ELEPHANT 3B.

The testing procedure was as follows. The aircraft were attached to the high-altitude burst balloon at all time, and when the desired altitude was reached, the computer initiated the full system, including the AB-PPT. The wings were designed such that the aircraft would fly in circles during operation through the balloon tether line. The balloon would reach a maximum altitude of approximately 30 km. At this point the balloon would burst, and the aircraft would fall on the ground under parachute. In addition to the different diagnostics, which will be discussed in the next sections, a GPS and an APRS (Automatic Packet Reporting System) were placed on the aircraft in order to facilitate finding the payload once on the ground. To meet the flight requirements, three different versions were designed and built at the APL. The design was based on the three main variables previously discussed, the lift force (F_{lift}), drag force (F_{drag}), and the net force delivered by the AB-PPT (F_{thrust}).

5.2.1 *Experimental Lift with Electric Propulsion at High Altitude Niche, Test 1*

The first in field test was Experimental Lift with Electric Propulsion at High Altitude Niche, Test 1 (ELEPHANT 1), Figure 5.7. The 5 kg aircraft had a wingspan of 6.5 m, 0.8 m of cord and an angle of attack of 15 degrees. The aircraft was flown in a flaps-down configuration, and a lift-to-drag ratio (C_l/C_d) of 3.75 was estimated. The propulsion system used for the aircraft was the first iteration of the AB-PPT with the adjustable electrodes mechanism, with a maximum specific thrust value of 240 mN/kW.

Figure 5.7: ELEPHANT 1 being launched using a high altitude burst balloon.

ELEPHANT 1 was powered with a total of 400 cell-coin batteries of 3.2 Volts and 90 mA-hr each, connected in series, resulting in a total energy of 115 W-hr, Figure 5.8. The duration of the flight was designed to be 90 minutes, with the AB-PPT operating at 2 Hz. Using 1200 Volts and

40 μF capacitors, the resulting energy per discharge would be 29 Joules. In order to overcome the drag force, operating the AB-PPT at higher frequencies is desirable, however, the electronics and charging system design of the ELEPHANT 1 were limited to a maximum frequency of 2 Hz. The total impulse, delivered by the propulsion system to the aircraft after the 90 minutes of operation, would yield a final velocity of 10 m/s. The estimated lift force for the ELEPHANT 1 would be sufficient to lift 20% of its total weight (5 kg).

Figure 5.8: Power supply consisting of 400 cell-coin batteries of 3.2 Volts and 90 mA-hr each, connected in series, resulting in a total energy of 115 W-hr.

In addition to the GPS and APRS system, a Rogowski coil on the positive side of the capacitor bank connected to the anode, and four cameras were installed on the ELEPHANT 1. One of the cameras was placed on one of the wings, one on the tail, one on the fuselage, and one attached to the main cord, that was used to attach the aircraft to the balloon. All of the four cameras were pointing towards the fuselage of the aircraft.

The aircraft was found 112 km away from the launching site. However only the camera placed on the fuselage was recovered. Based on the data obtained from the APRS system and the video camera, we believe that the ELEPHANT 1 did not quite reach the operating altitude (20 km) for the thruster. Thus, no in-situ data on the thruster were obtained. However, the data showed that the very lightweight construction of the ELEPHANT 1 was robust enough to withstand passage upward through the jet stream. Figure 5.9 shows the altitude of the aircraft versus ground speed obtained from the APRS system.

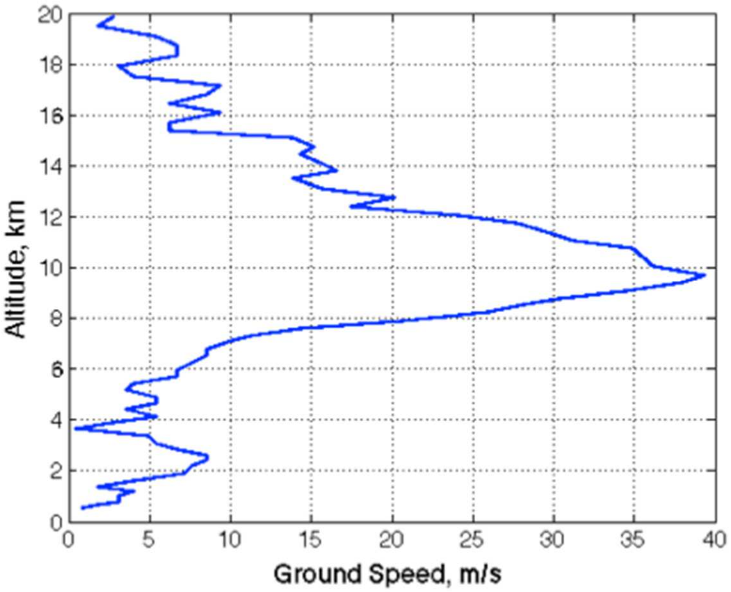

Figure 5.9: Altitude versus ground speed of the ELEPHANT 1. Data obtained from the APRS system. The jet stream was located approximately in the 8-16 km range, and for station keeping, an aircraft speed of < 10 m/s would be needed.

Each point was measured approximately every two minutes. Ground speeds at an altitude of 20 km suggest that for station keeping in the 20-30 km altitude range, a minimum aircraft speed of 5 m/s is needed. With the proposed system, speeds of > 5 m/s should be achievable.

Additionally, we observed an increase in the speed in the 8-12 km range of altitude, suggesting that during launching the jet stream was located in this range.

5.2.2 *Experimental Lift with Electric Propulsion at High Altitude Niche, Test 2*

For the second in field test, two aircraft were built - Experimental Lift with Electric Propulsion at High Altitude Niche, Test 2A, and Test 2B; ELEPHANT 2A (E2A) and ELEPHANT 2B (E2B) respectively. Both aircraft were 4 kg in weight, had a wingspan of 3 m, 0.8 m of cord and an angle of attack of 0 degrees. An airfoil E178 with an angle of attack of 0 was chosen, resulting in a lift-to-drag coefficient of 4. Similar to ELEPHANT 1, the propulsion system used for the aircraft was the first iteration of the AB-PPT with the adjustable electrodes mechanism, and the cylindrical igniter configuration. However, in order to simplify the system, the cathode diameter of the AB-PPT was fixed at 27, and 37 cm for E2A and E2B respectively. Similar to ELEPHANT 1, in addition to the GPS and APRS system, a Rogowski coil on the positive side of the capacitor bank connected to the anode, and four cameras were installed on E2A and E2B. One of the cameras was placed on one of the wings, one on the tail, one on the fuselage, and one attached to the main cord, that was used to attach the aircraft to the balloon. All of the four cameras were pointing towards the fuselage of the aircraft. Figure 5.10 shows a picture of E2A while being prepared before launching, and Figure 5.11 a picture of E2A after being launched.

Figure 5.10: ELEPHANT 2A on the ground while being prepared, before launching.

Figure 5.11: ELEPHANT 2A being launched using a high altitude burst balloon.

Similar to ELEPHANT 1, E2A and E2B were powered with a total of 400 cell-coin batteries of 3.2 Volts, but 165 mA-hr each, resulting in a total energy of 211 W-hr, Figure 5.8. This increased in energy allowed the system to increase the operation frequency of the AB-PPT, from 2 to 5 Hz. The duration of the flight was also designed to be 90 minutes. Using 1200 Volts and 40 μF capacitors, the resulting energy per discharge would be 29 Joules. For E2A and E2B, a more refined electronic system was implemented, consisting of four main sub-systems – pressure sensor, microcontroller-based computer, programmed in ASM, igniter system, and main discharge system. The electric diagram used for E2A, and E2B is shown in Figure 5.12.

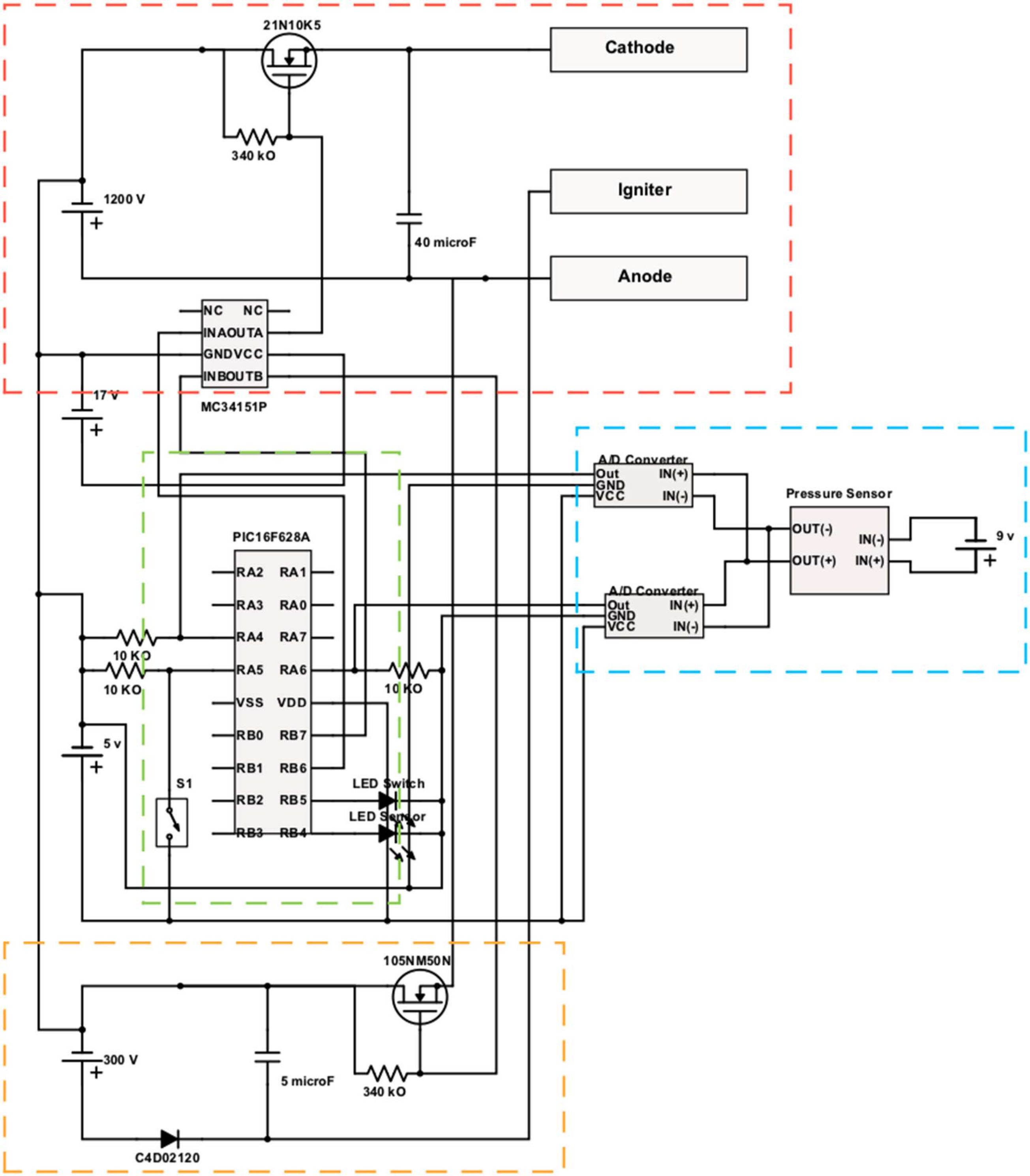

Figure 5.12: Electric diagram of the charge/discharge system used for the E2A and E2B, laboratory, and in field tests. The system consists of four subsystems: pressure sensor (blue box), igniter (yellow box), main discharge (red box), computer (green box).

The description and operation of each of the subsystems is as follows:

1. The pressure sensor subsystem consists of a Honeywell 015PAAA5 pressure sensor that outputs a 0-4.5 voltage range, 4.5 being the equivalent to 1 atm. When the aircraft is at the desired altitude (typically in the 0.5-0.7 Volts range), the pressure sensor sends a digital signal to the microcontroller (ports RA4, and RA6) through an analog-to-digital (A/D) converter. The pressure sensor is powered with a 9-Volt battery.
2. Microcontroller system. A microcontroller (PIC16F827), programmed in ASM, is used as the main computer (code provided in appendix A). When the pressure sensor sends the signal, the microcontroller operates the gate driver (MC34151) that activates the two MOSFETS that controls the igniter, and the main charging system. The microcontroller ports that control the igniter and main charging system are RB7, and RB6 respectively. The microcontroller is powered with 4.5 Volts, whereas the gate driver, with 17 Volts. The microcontroller can also be substituted by an Arduino or a Raspberry Pi board.
3. Igniter system. Similar to the laboratory testing, the igniter circuit consists of a secondary capacitor, a step-up toroidal transformer and a MOSFET. The two ends of the transformer are connected, one to the igniter and the other one to the cathode.
4. Main charging system. The main discharge capacitor bank is comprised of eight 20 μF, 1.3 kV polypropylene capacitors. Two of them were connected in series and the resulting four sets were connected in parallel. The resulting capacitance of the main discharge bank was 40 μF. The charging voltage was provided by the power supply consisting of 400 cell-coin

batteries. The voltage bank was then connected directly to the capacitor bank, regulated by the MOSFET.

In order to avoid overheating and arcing due to the lack of air at the operation altitudes, in particular the MOSFETS and IGBTs, the electronics were placed in a box containing mineral oil, and in order to protect the rest of the electronics from the low temperatures, the box containing mineral oil, batteries, transformer, and main capacitor bank were covered with foam.

E2A reached a maximum altitude of 25 km, and was designed to start operating at 19.8 km. It remained in the operation zone for approximately 15 minutes. Based on the data obtained we found that the AB-PPT attempted to fire 4769 times, however the system was not able to function. After analyzing the aircraft once on the ground, we found a poor electrical connection of the battery source to one of the key electronic components - the IGBT driver. It was concluded that the vibrations caused from transportation to the launching site, and the launch itself affected the in-house designed battery holder.

E2B reached a maximum altitude of 24.5 km, and was designed to start operating at 23 km. It remained in the operation zone for approximately 6 minutes. The system attempted to fire 1967 times, however only 57 were successful. The aircraft was still functional when it was found on the ground, thus we were able to test the entire system in the laboratory to find the cause of the misfires. It was found that the igniter configuration was not properly designed. In addition to the different disadvantages previously discussed in section 3.3, of having the igniter in a cylinder-shaped configuration around the anode, the igniter spark when activated, would occur in such a way that it would be blocked (hidden) between the igniter cylinder and the anode, as a result, the igniter spark would not help with the main breakdown discharge. This situation was solved by reducing the gap between the anode and the cylindrical igniter towards the tip and raising the isolation further up, in a cone-shaped-like configuration. Figure 5.13 shows the two cylindrical igniter configurations.

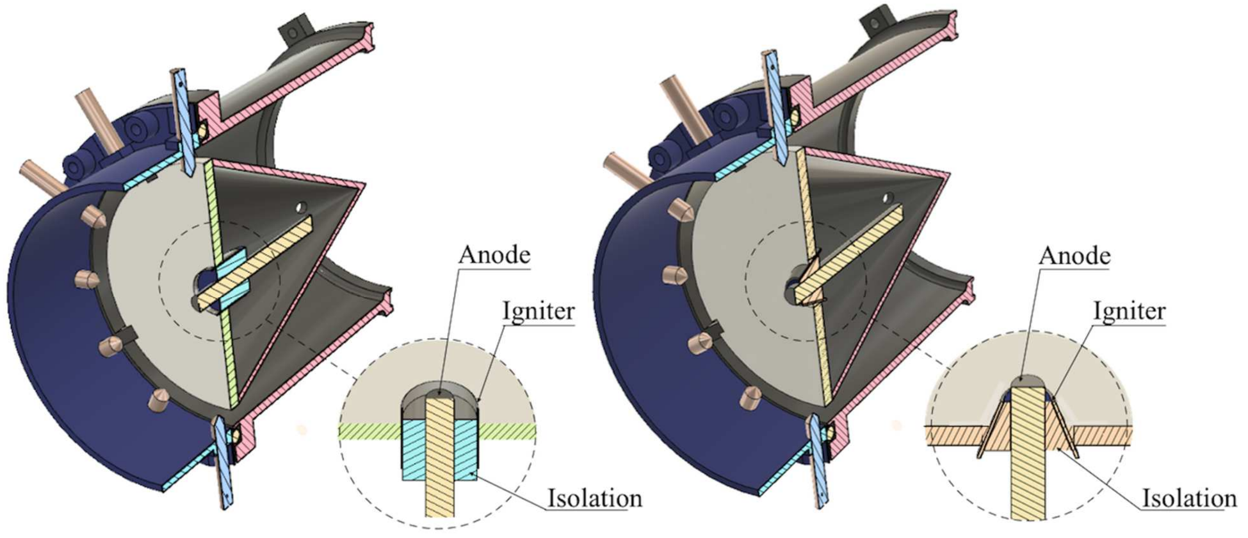

AB-PPT with Cylindrical Igniter

AB-PPT with Improved Cylindrical Igniter

Figure 5.13: Cylindrical igniter configurations used in the first iteration of the AB-PPT with the addition of the variable spacing cathode mechanism. a) Configuration used for the in-field testing of the E2A, and E2B, b) improved cylindrical igniter configuration. Details such as the nozzle, variable spacing cathode mechanism, and electrical connections have been omitted in this figure.

It is acknowledged by the author that this situation could have been avoided if more experimental testing prior the infield launches had been performed. Figure 5.14 shows a picture of E2A at its highest altitude, approximately 25 km, Figure 5.15 the trajectories of E2A, and E2B, obtained from the APRS system, and Figure 5.16 a picture of E2B after landing.

Figure 5.14: ELEPHANT 2A at its maximum altitude, approximately 25 km. Picture taken from the camera mounted on the tail of the aircraft.

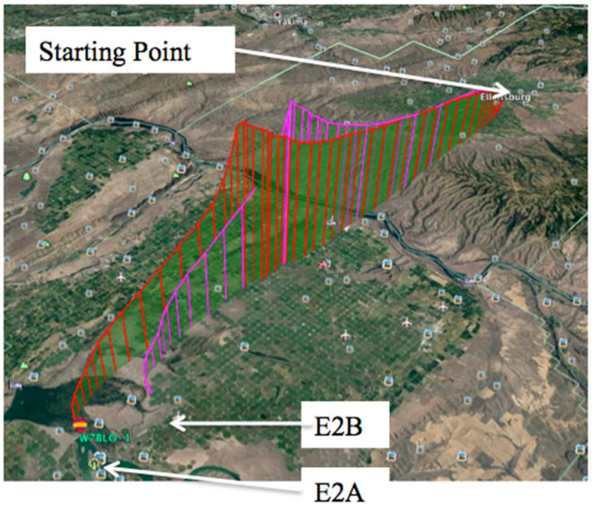

Figure 5.15: High-altitude burst balloon trajectories of the ELEPHANT 2A, and ELEPHANT 2B launches. The data is based on the APRS system. Peak altitudes are estimated as 25 km for E2A, and 24.5 for E2B.

Figure 5.16: ELEPHANT 2B after landing. The aircraft was found on a corn field, with no major damage to the structure.

5.2.3 *Experimental Lift with Electric Propulsion at High Altitude Niche, Test 3*

Because ELEPHANT 2A, and 2B did not suffer major structural damage after landing, for the third in field testing - Experimental Lift with Electric Propulsion at High Altitude Niche, Test 3A, and Test 3B; ELEPHANT 3A (E3A), and ELEPHANT 3B (E3B) respectively, the structure of the two previous aircraft, E2A, and E2B, was re-used. Therefore, the characteristics for the third launch were similar to the previous one. However, with the goal of increasing the performance of the system, different modifications, in particular to the AB-PPT and the electronics, were performed.

1. Due to better experimental performance obtained at the APL, the second iteration of the AB-PPT with the addition of the variable spacing cathode mechanism was used. Similar to E2A and E2B, in order to simplify the system, the cathode diameter of the AB-PPT was fixed at 27, and 37 cm for E3A and E3B respectively.
2. Since the geometry of the igniter was the main cause of the misfires of ELEPHANT 2B, the modified spark configuration was used, Figure 5.13.

3. Another possible reason for the misfires in ELEPHANT 2B, was the pulse frequency of operation. Initially, the cell-coin battery stack was able to supply enough energy to charge the main capacitors at the operational voltage (1200 V) in < 200 ms, which is ideal for a frequency operation of 5 Hz. However, after approximately 3 minutes of constant operation, the charging time was affected, increasing the charging time to approximately 300 ms. Therefore, for the third launch, two options were considered, 1) using more powerful batteries, and 2) reducing the pulse frequency of the AB-PPT. In order to maintain the weight of the system at 4 kg, for ELEPHANT 3A and 3B we decided to reduce the frequency, from 5 to 3 Hz.
4. The design of the battery holders and connections were improved. In addition to performing vibrational testing.
5. The electronics were more rigorously tested before the launch. For ELEPHANT 2, the electronics were tested in the bell-jar shaped vacuum chamber, Figure 3.1. However, the size of this chamber did not allow us to test the electronics while having them placed in the fuselage of the aircraft, thus after testing them we had to disconnect the entire system and connect it again once in the fuselage. This situation increases the risk of having poor and loose electrical connections, and having arcs that were not detected in the bell-jar shaped vacuum chamber. For ELEPHANT 3, the entire system (the electronics placed in the fuselage) was tested in our medium size vacuum chamber. Figure 5.17 shows the two electronic systems tested for ELEPHANT 2, and 3.

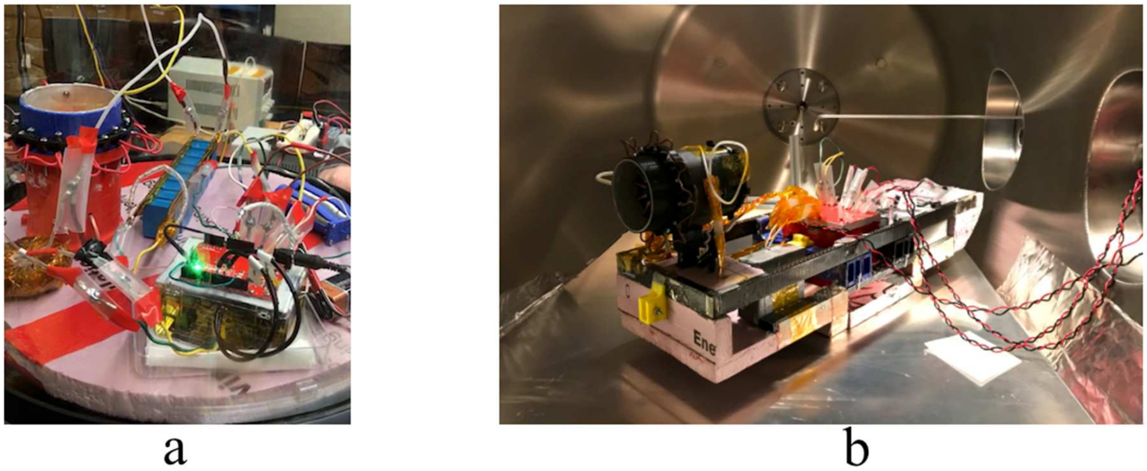

Figure 5.17: Electronic systems being tested prior the different in field testing. a) electronics tested for ELEPHANT 2, b) electronics tested for ELEPHANT 3.

Similar to the previous aircraft launches, in addition to the GPS and APRS system, a Rogowski coil on the positive side of the capacitor bank connected to the anode, and four cameras were installed on E3A and E3B. One of the cameras was placed on one of the wings, one on the tail, one on the fuselage, and one attached to the main cord, that was used to attach the aircraft to the balloon. All of the four cameras were pointing towards the fuselage of the aircraft.

The trajectory of ELEPHANT 3A, and 3B are shown in Figure 5.18. ELEPHANT 3A reached a maximum altitude of 29 km, and was designed to start operating at 20 km. It remained in the operation zone for approximately 30 minutes. From the total number of attempts to discharge, the AB-PPT fired 62% of those attempts. It is believed that at the beginning of the operation (20 km), the background air pressure was too high for breakdown to occur, thus most of the misfires occurred in the 22-26 km altitude range. This hypothesis can be validated by looking at the Rogowski coil data, which helps us determine the percentage of discharges as a function of altitude, Figure 5.19. It is noticed that the percentage increases with altitude, reaching an average of 90% at approximately 27 km.

For ELEPHANT 3B, we decided to use two balloons Figure 5.20, which were filled with lower amount of gas. The goal was to extend the flying time, in order to have more time to test the system. It reached a maximum altitude of 33 km, and was designed to start operating at 23 km. It remained in the operation zone for 80 minutes, however no discharges were detected. We believe that the aircraft took longer than expected to reach altitude, and the 9 Volt and IGBT batteries were drained before getting into the operation zone.

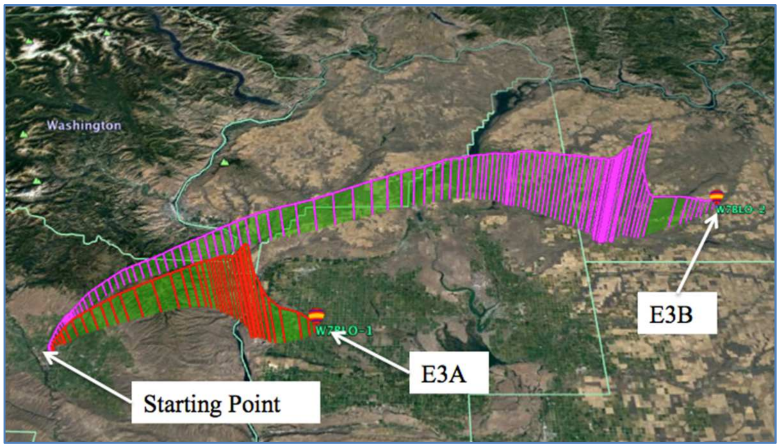

Figure 5.18: High altitude burst balloon trajectories of the ELEPHANT 3A, and ELEPHANT 3B launches. The data is based on the APRS system. Peak altitudes are estimated as 29 km for E3A, and 33 for E3B.

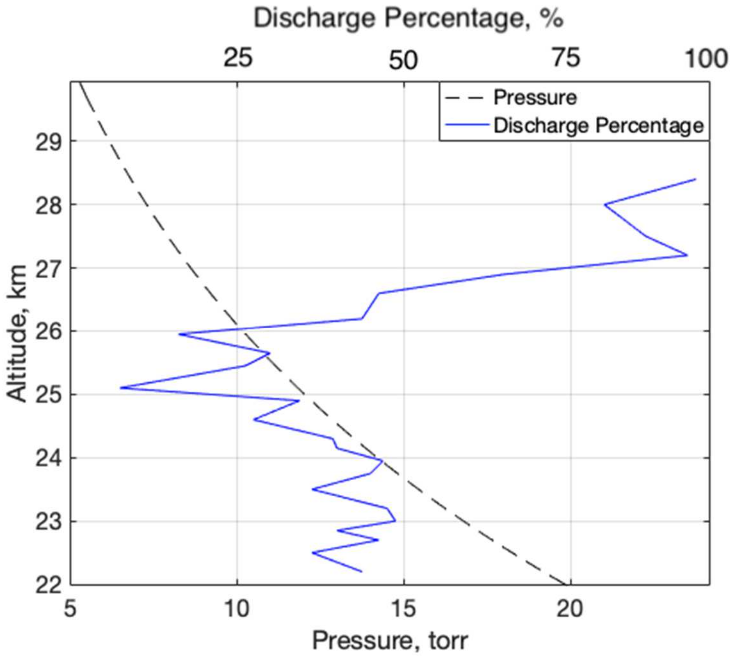

Figure 5.19: Discharge percentage as a function of atmospheric altitude of ELEPHANT 3A.

Figure 5.20: ELEPHANT 3B launch. In order to extend the flying time, the aircraft was launched using two balloons, filled with lower amount of gas.

The different in-field testing helped us understand the performance of the AB-PPT and the multiple components of the system in real atmospheric conditions. Through the laboratory experimental testing, and the different launches of the aircraft into the stratosphere, we were able to make continuous progress in the development of the AB-PPT, high pulsed-power electronics, aircraft structure, and the telemetry system. Resulting in our most successful in-field testing to date - ELEHPANT 3A, and thus demonstrating that the possibility of having an atmospheric satellite is a near-term reality. We were able to demonstrate that the aircraft can be placed into the stratosphere, by passing it through the jet stream using high-altitude burst balloons, without perturbing the system, and with no structural damage. Additionally, we demonstrated that the AB-PPT, when properly design and tested, can perform as per laboratory results and expectations.

Chapter 6. FURTHER APPLICATIONS

To date, the analysis of the AB-PPT has been focused on applications for terrestrial atmosphere, at a pressure range of approximately between 10 and 40 Torr. However, the device is not limited to such conditions. Thanks to the addition of the variable spacing electrode mechanism, and the ease at which the breakdown voltage can be regulated, the AB-PPT has the ability and flexibility of functioning in different conditions. In other words, the system can efficiently function at different background pressure ranges, and with different background gases. Thus, the AB-PPT could be also potentially used for propelling a spacecraft in planets/moons with an existent atmosphere, such as Mars and Titan. In this section we provide an analysis of the system using CO_2 as the background atmosphere, with the goal of simulating Martian conditions.

6.1 POSSIBLE APPLICATIONS FOR MARS EXPLORATION

In order to predict the performance of the AB-PPT in Mars, specific thrust measurements were performed using CO_2. The experiment was carried out in the bell-jar shaped vacuum chamber, and the thrust measurements were obtained using the pendulum-based thrust stand. The experiment set up and procedure are similar to the ones described in section 3.1. Additionally, the AB-PPT was tested at five different cathode diameters: 26.8, 34, 40.8, 45.5, and 52.4 mm, and the voltage per discharge was kept at 800 Volts.

Because more than 95% of the Martian atmosphere is comprised of CO_2, the experiment was performed using solely this gas. Additionally, because the bell-jar shaped vacuum chamber is relatively small (0.14 m^3), filling it up with CO_2 did not represent a major challenge. The air was first removed with vacuum pumps to a background pressure of 9 milliTorr, and then filled to a background pressure of 20 Torr with CO_2. The air percentage in the experiment was very low

(0.045%), and thus neglected in the analysis. Figure 6.1 shows the relation between the different cathode diameters of the AB-PPT and the background gas pressure at which breakdown first occurs, for both gases, air and CO_2.

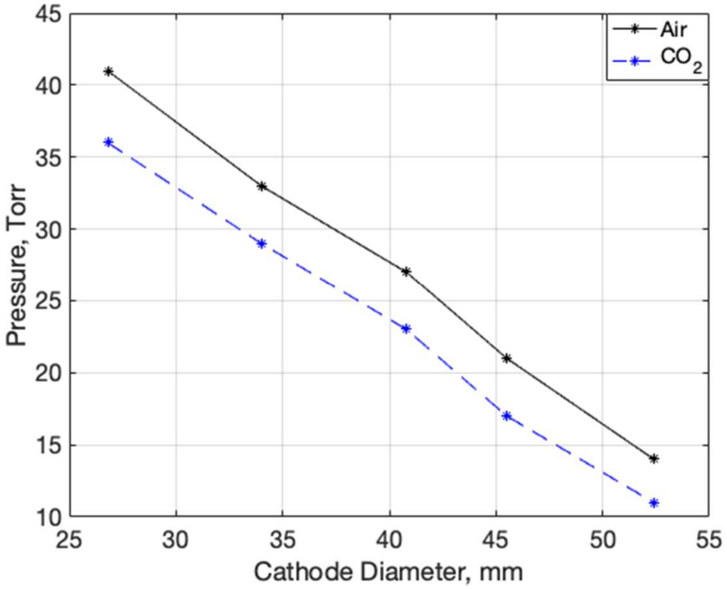

Figure 6.1: Cathode diameters of the AB-PPT versus background gas pressure at which breakdown first occurs, for both gases, air and CO_2. The experiment was performed using 800 Volts per discharge, at five different cathode diameters: 26.8, 34, 40.8, 45.5, and 52.4 mm.

It is noticed that the breakdown of air occurred at a higher background pressure, meaning that it takes more energy to ionize the CO_2. While ionization energy of air and CO_2 are very similar, CO_2 is a greenhouse gas, and has additional vibration modes [34], which absorb additional energy, and hence requiring more energy for breakdown. As a result, the point at which breakdown first occurs to be at a lower background gas pressure. Because the specific thrust of the AB-PPT is highly dependent on the background pressure of the neutrals, the specific thrust of the system is 25% lower. Figure 6.2 shows the specific thrust values of the AB-PPT for both gases, air and CO_2.

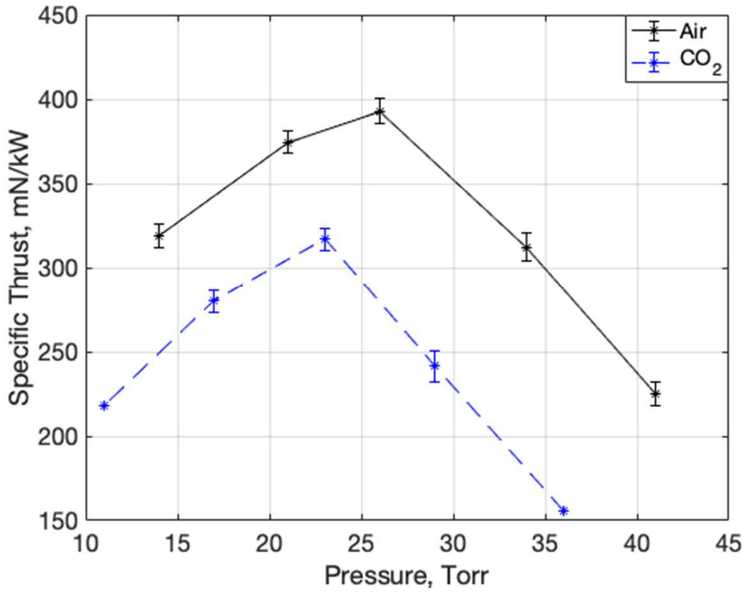

Figure 6.2: Specific thrust versus background gas pressure of the AB-PPT, for CO_2 and air. The test was performed using a voltage source of 800 Volts, and five different cathode diameters, 26.8, 34, 40.8, 45.5, and 52.4 mm.

Maximum specific thrust values of 317 mN/kW using CO_2 were obtained at a background gas pressure of 23 Torr. Such specific thrust values are an average of approximately 80 mN/kW lower than the values obtained when using air. However, because the gravity on Mars is 63% lower than the gravity on Earth, the thrust requirements to propel and sustain an aircraft in Martian atmosphere are also lower.

Figure 6.3 shows the sequence of a proposed mission, where a satellite orbiting Mars delivers a secondary satellite, powered with the AB-PPT, which would fly at much lower altitudes. Since the gravity on Mars is relatively low when compared to Earth's, the background pressure is more uniform, thus the range of operation of the proposed satellite would be wider.

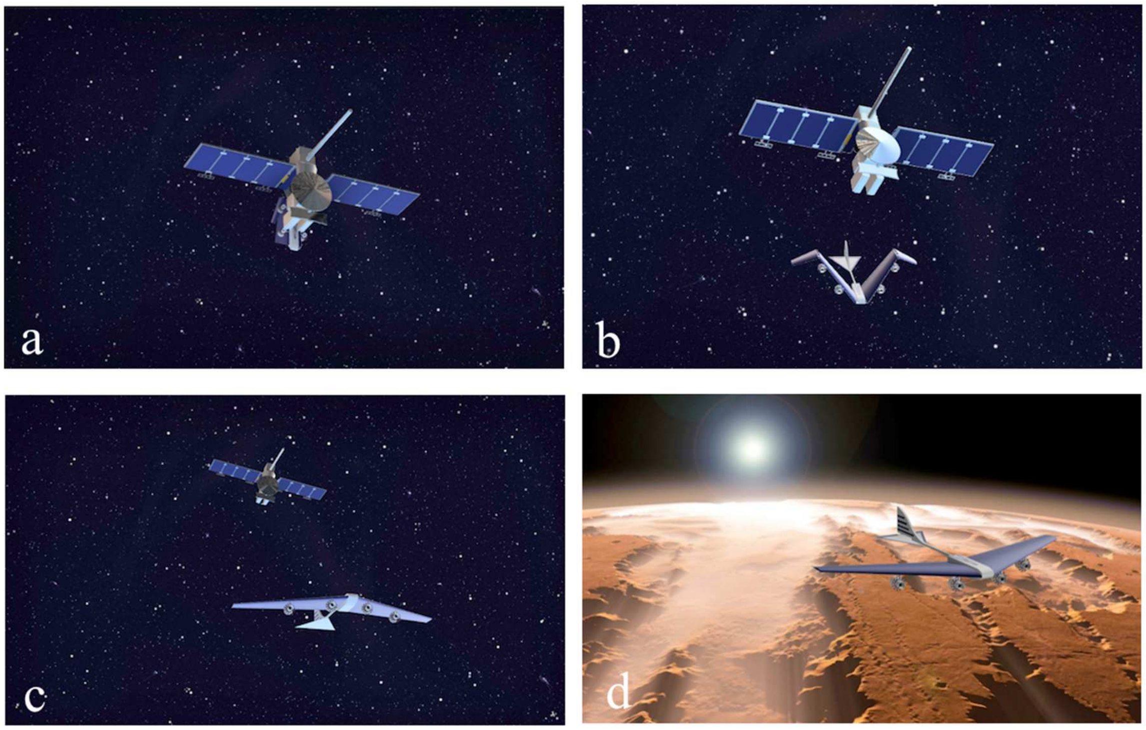

Figure 6.3: Sequence of a proposed mission to Mars to deliver an atmospheric satellite, powered with the AB-PPT.

Chapter 7. CONCLUSIONS

An Air-Breathing Pulsed Plasma Thruster AB-PPT has been presented and studied. Because the device was initially intended for atmospheric satellite application, specific thrust measurements using a pendulum-based thrust stand were performed and used as the key parameter of the system's performance. Additionally, an analytical expression as a function of measurable plasma parameters, for the specific thrust was derived. The expression was validated experimentally, using a quadruple Langmuir probe for electron density (n_e), electron temperature (T_e), and ion speed (u_i), and a B-dot probe for magnetic field measurements. Measurements suggest, that the acceleration mechanism of the AB-PPT is the contribution of, 1) ion-neutral collisions, with a contribution of 57%, 2) electromagnetic acceleration, with a contribution of 33%, and 3) electrostatic acceleration, with a contribution of 10%. Using the pendulum-based thrust stand, specific thrust values of 395 mN/kW were obtained, whereas specific thrust values of 352 mN/kW, using the Langmuir probe and B-dot probe data were obtained.

In order to test the system under real atmospheric conditions, different in-field testing was performed, where five in-house constructed aircraft were launched into the stratosphere using high-altitude burst balloons, demonstrating that the system can performed as per laboratory results and expectations. Additionally, we demonstrated that high-altitude burst balloons are a safe, efficient, and inexpensive method for launching an aircraft of this type into the stratosphere. Based on commercially available technology, a proposed fully functioning 20 kg aircraft, with a 35 meter wingspan was also described.

Other suggested applications were discussed, such as Martian exploration. An experimental test using CO2 as the background gas, indicated a reduction in specific thrust of 25% when compared to the specific thrust values obtained when using air as the background atmosphere.

However, because the gravitational force in Mars is much lower, the lift requirements of the aircraft are lower, and thus, the potential application of the AB-PPT for Martian exploration is feasible.

BIBLIOGRAPHY

[1] Thomas E. Noll, et al. "Investigation of the Helios Prototype Aircraft Mishap," Vol. I Mishap Report, NASA, January 2004.

[2] Airbus, "Airbus Zephyr Solar High Altitude Pseudo-Satellite flies for longer than any other aircraft during its successful maiden flight," August 2019.

[3] Warwick, Graham "Facebook Flies Stratospheric Internet-Delivery UAV," Aerospace Daily and Defense Report, Jul 26, 2016, Vol. 257(17), p.3

[4] Craig L. Nickol, Mark D. Guynn, Lisa L. Kohout, and Thomas A. Ozoroski, "High Altitude Long Endurance UAV Analysis of Alternatives and Technology Requirements Development," NASA TP-2007-214861.

[5] Shubhdeep Kaur, and Sukhchandan Randhawa, "Google LOON: Balloon-Powered Internet for Everyone," *AIP Conference Proceedings*, Vol 2034, No. 1, 2018.

[6] Magnuson Stew "Air Force explores balloon-assisted launches," Space News, Jan 13, 2003. Vol. 14(2), p. 20(1)

[7] Stéphane Mazouffre, "Electric propulsion for satellites and spacecraft: established technologies and novel approaches," Plasma Sources Sci. Technol. 25 (2016) 033002 (27 pp).

[8] Dan M. Goebel and Ira Katz "Fundamentals of Electric Propulsion: Ion and Hall Thrusters," Jet Propulsion Laboratory, California Institute of Technology, 2008, pp. 1-5

[9] Felix Berner and Morton Camac "Air Scooping Vehicle," Planetary and Space Science, Vol. 4, 1961.

[10] Nishiyama, K., "Air Breathing Ion Engine Concept," *Proceedings of the 54th International Astronautical Congress of the International Astronautical Federation*, Institute of Space and Astronautical Science, Japan, 2003, pp. 1-5.

[11] V. Hruby, B. Pote, T. Brogan, K. Hohman, J. Szabo, and P. Rostler, "Air breathing electrically powered Hall effect thruster," U.S. Patent 6834492, Dec. 28, 2004.

[12] Ian K. Johnson, Robert M. Winglee, and B. Race Roberson "Pulsed Plasma Thruster for Atmospheric Operation," Propulsion and Energy Forum, *50th AIAA/ASME/SAE/ASEE Joint Propulsion Conference*, 2014, pp. 1-10.

[13] Tony Schönherr, Kimiya Komurasaki, Francesco Romano, Bartomeu Massuti-Ballester, and Georg Herdrich, "Analysis of atmosphere-Breathing Electric Propulsion," *IEEE Transactions on Plasma Science*, Vol. 43, No. 1, 2015, pp. 287-294.

[14] James S. Sovey, Terry L. Hardy, and Matthew Englehart "A Bibliography of Electrothermal Thruster Technology," Lewis Research Center, Cleveland, Ohio, 1984.

[15] Burton, R. L., and Turchi, P. J. "Pulsed Plasma Thruster," *AIAA Journal of Propulsion and Power*, Vol. 14, No. 5. 1998, pp. 716-735.

[16] Matthias Lau, and Georg Herdrich, "Plasma diagnostic with inductive probes in the discharge channel of a pulsed plasma thruster," Vacuum 110 (2014) 165-171.

[17] Robert G. Jahn, "Physics of Electric Propulsion," 1968, pp. 263-265.

[18] Paige E. Northway, "Pulsed Plasma Thruster Gains in Specific Thrust for CubeSat Propulsion," Propulsion and Energy Forum, *53rd AIAA/SAE/ASEE Joint Propulsion Conference, Atlanta, GA, 2017.*

[19] E. Husain and R.S. Nema "Analysis of Paschen curves for air, N_2 and SF_6 using the Townsend breakdown equation," *IEEE Transactions on Electrical Insulation*, 1982. Vol. EI-17 No. 4.

[20] Manuel Azuara Rosales, Paige E. Northway, and Robert M. Winglee, "Air-Breathing Pulsed Plasma Thruster with a Variable Spacing Cathode for Atmospheric Satellite Applications," Propulsion and Energy Forum, *53rd AIAA/SAE/ASEE Joint Propulsion Conference*, Atlanta, GA, 2017.

[21] Manuel Azuara Rosales, Corwin Hansen, and Robert M. Winglee, "Theoretical and Experimental Analysis for an Air-Breathing Pulsed Plasma Thruster," AIAA Propulsion and Energy Forum, Indianapolis, IN, 2019.

[22] Rodney L. Burton, Susan G. Del Medico, and J. Chris Andrew, "Application of a Quadruple Probe Technique to MPD Thruster Plume Measurements," *AIAA Journal of Propulsion and Power*, Vol. 9, No. 5, 1993, pp. 771-777.

[23] C. Bruce and L. Talbot, "Cylindrical Electrostatic Probes at Angles of Incidence," *AIAA Journal*, Vol. 13, No. 9, 1975, pp. 1236-1238.

[24] Madhoo Kanal, "Theory of Current Collection of Moving Cylindrical Probes," *Journal of Applied Physics*, Vol. 35, No. 6, 1964.

[25] Sin-Li Chen, and T. Sekiguchi, "Instantaneous Direct-Display System of Plasma Parameters by Means of Triple Probe," *Journal of Applied Physics*, Vol. 36, No. 8, 1965, pp. 2363-2375.

[26] Billy H. Johnson and David L. Murphree, "Plasma Velocity Determination by Electrostatic Probes," *AIAA Journal*, Vol. 7, No. 10, 1969, pp. 2028-2030.

[27] G. Poissant, and M. Dudeck, “Velocity Profiles in a Rarefied Argon Plasma Stream by Crossed Electrostatic Probes,” *Journal of Applied Physics*, Vol. 58, No. 5, 1985, pp. 1772-1779.

[28] Richard C. Fernow, “Principles of Magnetostatics,” 2016.

[29] Stewart S. Bushman and Rodney L. Burton, “Heating and Plasma Propoerties in a Coaxial Gasdynamic Pulsed Plasma Thruster,” Journal of Propulsion and Power. Vol. 17, No. 5, September-October 2001.

[30] Scott Allen Bufton, “Exit Plane Plasma Measurements of a Low-Power Hydrazine Arcjet,” PhD Thesis, Department of Mechanical Engineering, University of Illinois at Urbana-Champaign, Urbana, IL, 1996. Urbana,

[31] Bushman, S. S., “Investigation of a Coaxial Pulsed Plasma Thruster,” M.S. Thesis, Dept. of Aeronautical and Astronautical Engineering, University of Illinois at Urbana-Champaign, Urbana, IL, 1999.

[32] University of Illinois at Urbana-Champaign, Airfoil Coordinates Database, http://airfoiltools.com/

[33] Glider Flying Handbook, U.S. Department of Transportation, FAA-H-8083-13A.

[34] Takehiko Shimanouchi, “Tables of Molecular Vibrational Frequencies Consolidated,” Vol 1. Department of Chemistry, University of Tokyo, 1972. NSRDS-NBS 39.

APPENDIX A: E3 AND E2 MICROCONTROLLER (PIC16F628A) ASM CODE.

```
list P=16F628A
include <P16F628A.inc>
__config H'3F18'

org    0x000

num1   EQU 20
num2   EQU 21
num3   EQU 22
num4   EQU 23
num5   EQU 24
num6   EQU 25
num7   EQU 26
num8   EQU 27
num9   EQU 28
num10  EQU 29
num11  EQU 30
num12  EQU 31
num13  EQU 32
num14  EQU 33

START

clrf   PORTA               ; Clear memory of PORTA
clrf   PORTB               ; Clear memory of PORTB


bsf    STATUS,RP0

movlw  b'00000000'         ; Bank B defined as outputs
movwf  TRISB

movlw  b'11111111'         ; Bank A defined as inputs
movwf  TRISA

bcf    STATUS,RP0

MAIN

Movlw  b'11010000'         ; Declaration of PIC initial state
movwf  PORTB


btfss  PORTA,5             ; Asks pressure sensor if it’s in operation range
goto   MAIN                ; Go to main if sensor is out of range
goto   ON_charge.          ; Go to ‘‘ON_charge’’ if sensor is in range

ON_charge

movlw  b'10010000'         ; Capacitor charges
movwf  TRISB
call   delay_1 (x 610)     ; Charging time of 610 (x) delay_1 (200 ms)

movlw  b'11010000'         ; Capacitor charging stopped
movwf  PORTB
call   delay_1 (x 8)       ; Waiting time of 8 (x) delay_1 (2.6 ms)
```

```
movlw  b'01010000'        ; Igniter activated
movwf  PORTB
call   delay_1 (x 3)      ; Activation time of 3 (x) delay_1 (1 ms)


movlw  b'11010000'        ; Return PIC to the initial state
movwf  PORTB
call   delay_1

goto   MAIN               ; Go to the start of the program

delay_1                   ; Time delay loop
movlw  D'166'
movwf  num5
movlw  D'2'
movwf  num4
nop (x 4)
LOOP_2
decfsz num5,1
goto   LOOP_2
decfsz num4,1
goto   LOOP_2
return

END
```

APPENDIX B: AB-PPT AS A HYBRID SYSTEM

In addition to the usage of the AB-PPT at atmospheric altitudes > 20 km. The AB-PPT can be used as a hybrid system in order to extend its range of operation. As discussed earlier, because the AB-PPT doesn’t deliver sufficient thrust at atmospheric altitudes < 25 km, as shown in Figure 4.14, the system needs to be launch into the stratosphere using high-altitude burst balloons. This method is in particular convenient due to its low cost, simplicity, and because there is no need to develop an additional system that can efficiently operate at atmospheric altitudes < 20 km. However, the controlled access to atmospheric altitudes > 20 km is possible if conventional blade-based propellers are added to the system, as shown in Figure B. 1.

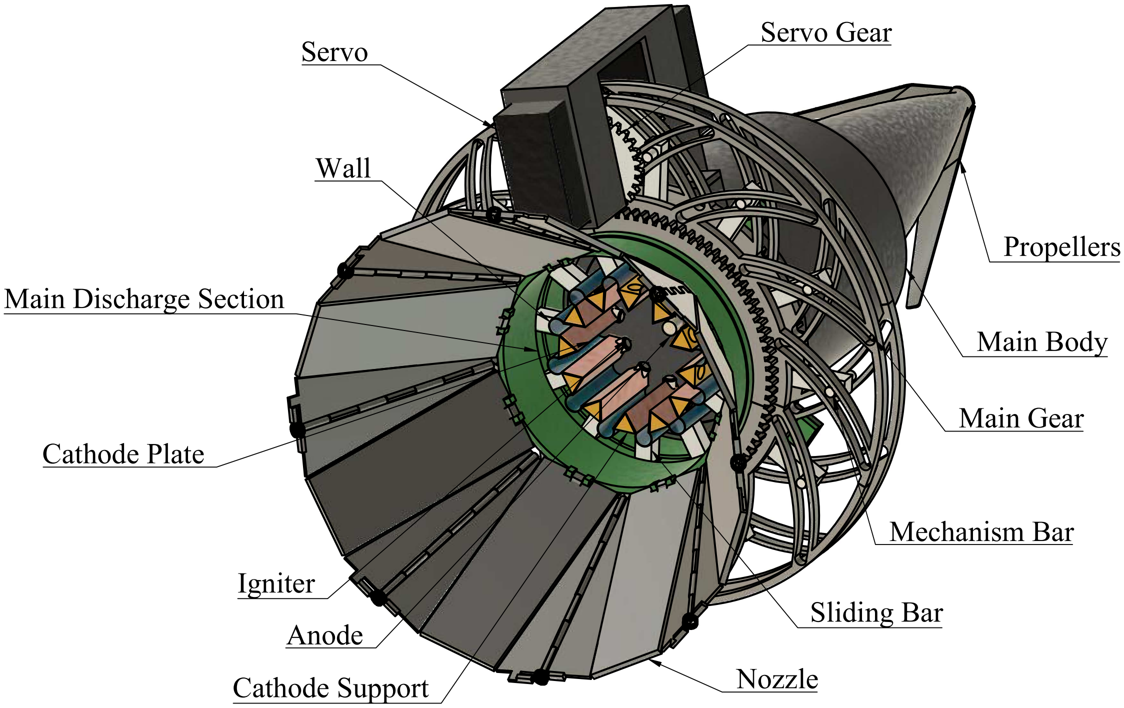

Figure B. 1: AB-PPT with the addition of conventional blade-based propellers, and adjustable size nozzle.

The proposed system has a total length of 320 mm, and has similar components to the AB-PPT presented in section 3.3. However, the hybrid system has the incorporation of blade-based propellers for operation at a higher-pressure regime, and the addition of a mechanism to adjust the aperture of the nozzle. The operation of the hybrid system is described as follows. When the aircraft is in a background pressure range of > 34 Torr, which corresponds to terrestrial atmospheric altitudes of 0 – 20 km, the propellers are activated, and in order to permit adequate air flow, the nozzle is closed, Figure B. 2. The aircraft in this case is powered only with blade-based propellers. When the background pressure lowers to < 34 Torr, which corresponds to terrestrial atmospheric altitudes of > 20 km, the blades are retracted, and because the addition of the nozzle helps increasing the amount of thrust, the nozzle also opens, Figure B. 1. In this scenario, the aircraft is powered using the pulsed plasma thruster system. Figure B. 3 shows a top view of both configurations.

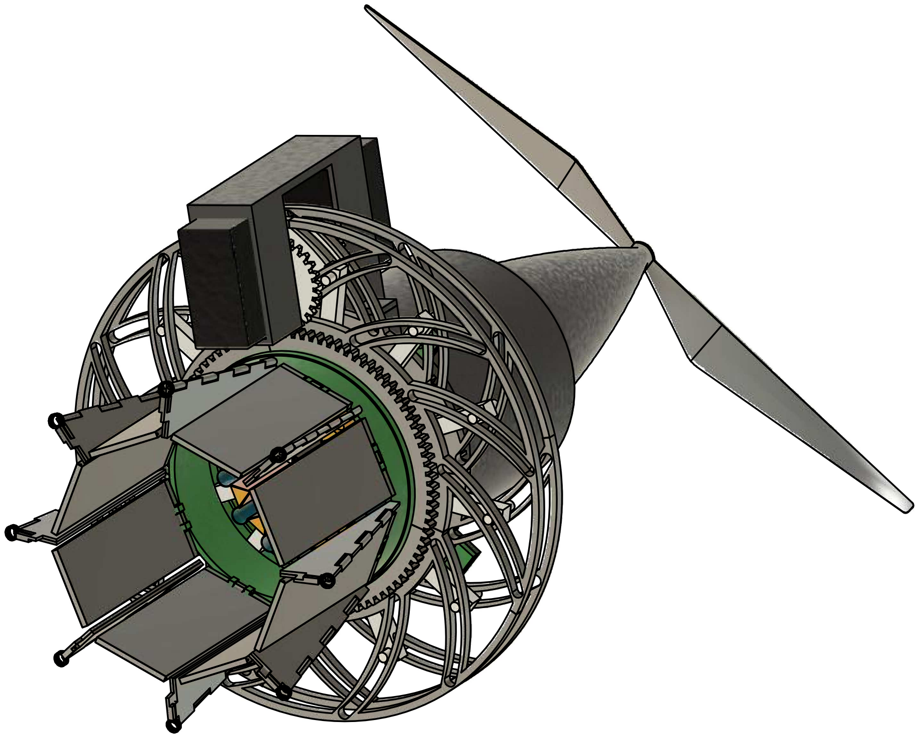

Figure B. 2: AB-PPT with the addition of conventional blade-based propellers, and adjustable size nozzle. Nozzle retracted and blades activated configuration, for operation at higher-pressure regime.

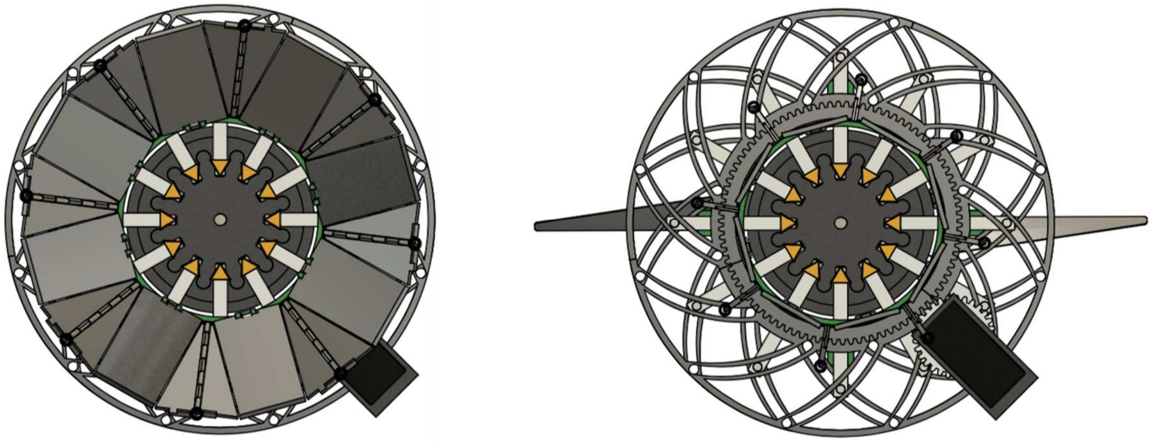

Figure B. 3: Top view of both of the configurations of the AB-PPT with the addition of conventional blade-based propellers, and adjustable size nozzle.

VITA

Manuel Azuara Rosales earned his bachelor’s degree in Mechanical Engineering from the Universidad del Valle de Mexico in 2009. He started his graduate education at the University of Washington in the Aeronautics and Astronautics department in 2013, obtaining his Master of Science degree in 2015, and PhD degree in 2020.